Julius-Maximilians-Universität Würzburg

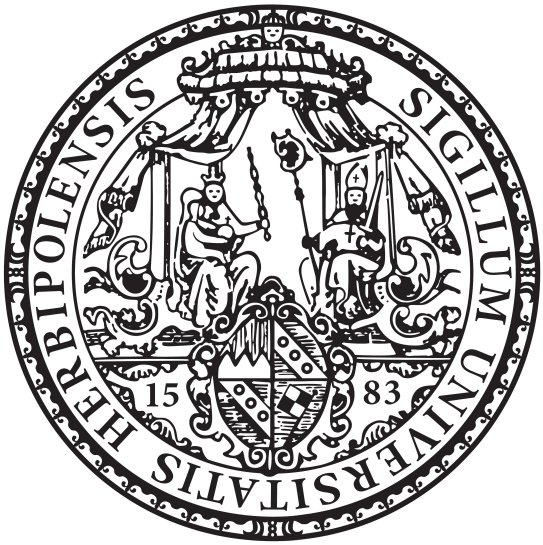

Accelerated non-Cartesian cardiovascular MR Imaging at 3 T and 7 T

Beschleunigte nicht-kartesische MRT Herzbildgebung bei 3 T und 7 T

Doctoral thesis for a doctoral degree at the Graduate School of Life Sciences, Section Biomedicine

submitted by

Philipp Eirich
from Haßfurt

Würzburg 2021

Submitted on: _____

Office stamp

Members of the Thesis Committee

Chairperson:	Prof. Dr. Peter Jakob
Primary Supervisor:	Prof. Dr. Herbert Köstler
Supervisor (Second):	Prof. Dr. Laura Schreiber
Supervisor (Third):	PD Dr. Bernhard Petritsch
Date of Public Defence:	_____
Date of Receipt of Certificates:	_____

Contents

1 Introduction

Magnetic Resonance Imaging (MRI) is a non-invasive imaging technique that has evolved to a major pillar in medical diagnosis in the past decades. Along with conventional radiography, computed tomography (CT) and medical ultrasound, MRI is one of the most commonly used imaging modalities in clinics and hospitals worldwide. In contrast to X-Ray-based imaging techniques, MRI does not expose the patient to ionizing radiation and it offers a high soft tissue contrast. Since its initial implementation in medical diagnosis in the mid-1980s, MRI has experienced an ongoing technical development[1, 2].
»Citius, Altius, Fortius« is the Latin motto of the Olympic Games, which can be translated to *»Faster, Higher, Stronger«* [3, 4]. This slogan is not only an accurate reflection of todays economy and society but can also be transferred to MR technology. One example is the field strength of the main magnetic field B_0, the core element of any MR scanner. Up to the turn of the millennium, the market was dominated by 1.5 Tesla (T) MR scanners. From 2000 on, 3 T MR scanners became available for clinical diagnosis [5]. Most of the clinical MR scans performed nowadays operate at these two field strengths. Nevertheless, there has always been a demand in increasing the B_0-field as it promises gains in signal-to-noise-ratio (SNR), contrast-to-noise-ratio (CNR) as well as imaging speed and efficiency [6]. Up to now, more than 70 human MR scanners operate at a field strength of 7 T, of which some has been licensed for clinical usage [7]. Moreover, first human MR images were published in 2019 at 10.5 T [8, 9]. The downside of this trend lies in considerable technical challenges. The inhomogeneity of the B_0-field and the radiofrequency (RF)-field (B_1), as well as the specific absorption rate (SAR) and the sensitivity to motion artifacts increase at higher field strengths [1, 7].

In general, some of the main drawbacks of MRI are the high costs involved, the acoustic noise produced by the scanner and long examination times [10]. That is to say, an MRI scan is accompanied with reduced patient comfort and even needs to be re-

peated when the patient moves in the meantime [10]. Therefore, research in the field of MRI often aims at accelerating the MRI process and thus reducing the scan time. Amongst many different milestones in the history of MRI, key contributors to fast imaging techniques were the invention of gradient echo pulse sequences [2, 11], the technology of phased array coil receive elements [2, 12] and their application to parallel imaging (PI) techniques [13, 14]. Most recently, the field of compressed sensing (CS) has proven to be a powerful tool for highly accelerated MRI by exploiting the sparsity that is present in some given domain of the MRI data [15]. Furthermore, the majority of clinical examinations still primary relies on conventional Cartesian data acquisition. Non-Cartesian k-space sampling patterns, e.g. radial or spiral trajectories, offer considerably more capabilities for rapid MRI. However, they also entail k-space sampling errors due to imperfections of the dynamic gradient system, which ultimately can lead to image artifacts.
When it comes to imaging moving tissue, i.e. in the cases of respiratory or cardiac motion, rapid MRI is of particular interest. Cardiovascular MRI (CMR), CT and ultrasound echocardiography are the three most common imaging modalities in the diagnosis of cardiovascular diseases [16]. CMR delivers highly accurate and reproducible information of cardiac morphology and function by covering the entire cardiac cycle at high spatiotemporal resolution [17, 18]. Nevertheless, a typical clinical CMR scan is performed in several breath holds, which is not trivial for dyspneic patients. Also, inaccurate breathing states complicate the exact planning of the measurement, which eventually results in displacements in the images. In addition, conventional gated cardiac exams require a trigger signal and can be corrupted in patients suffering from cardiac arrhythmia. In these cases accelerated imaging approaches that aim to resolve the beating heart in real time are of particular interest.

Therefore, the purpose of this thesis was to develop strategies for accelerated CMR readout techniques by optimizing efficient non-Cartesian k-space trajectories. One main aspect was the correction of k-space trajectory errors in non-Cartesian imaging, which can be seen as the missing step to facilitate real-time CMR with high spatiotemporal resolution. On the one hand, this was achieved by efforts in pulse sequence development and on the other hand by image reconstruction techniques that employ PI and CS. The aim was to enable high-quality gated as well as real-time CMR at different main magnetic field strengths (3 T and 7 T). In addition, the developed rapid imaging approaches were compared to current clinical gold standard protocols by analyzing morphological and functional information of the myocardium tissue.

2 Theory

2.1 The basic principles of Magnetic Resonance Imaging (MRI)

This section briefly outlines the basic principles of the relevant physical concepts of MRI. The respective purpose of the different magnetic fields of an MR scanner is summarized in the first Subsection 2.1.1, followed by the concept of the gradient echo pulse sequence and the spatial frequency domain in Subsections 2.1.2 and 2.1.3, respectively.

2.1.1 The different magnetic fields of an MR scanner

MRI exploits the fact that over 75 % of the human body consists of water or lipids [2]. That is to say that hydrogen is the most abundant element in our body referred to the number of atoms. Hydrogen has a single proton, which exhibits a magnetic moment due to its nuclear spin angular momentum (referred to as spin in the following). Without an external magnetic field B, the orientation of each hydrogen spin in the human body is random, which means that in total they compensate each other and sum up to a macroscopic net magnetization $M = 0$. When a magnetic field B is present, the spins tend to align parallel or anti-parallel to the direction of B. A slight majority of spins favor the lower-energetic state parallel to B, resulting in $M \neq 0$. However, the spins are not aligned exactly with the direction of B. Instead, they experience a torque, which results in a precession around B with a given resonance frequency w_{L}, called the *Larmor* frequency [2].

w_L exhibits a linear dependency of B, following

$$w_\mathrm{L} = \gamma \cdot B, \tag{2.1}$$

with the nucleus-specific gyromagnetic ratio γ. In the case of hydrogen, the gyromagnetic ratio reads $\gamma/2\pi = 42.58\,\mathrm{MHz/T}$ [19]. Thus, the main magnetic field B_0 of an MR scanner (longitudinal axis) defines the resonance frequency of the individual spins. In the case of $B_0 = 3\,\mathrm{T}$ the *Larmor* frequency is $w_\mathrm{L} = 127.7\,\mathrm{MHz}$ and for $B_0 = 7\,\mathrm{T}$ w_L equals 298.1 MHz.
The net magnetization M of the human body in a MR scanner is in the order of $10^{-6}\,\mathrm{T}$ and thus not measurable if aligned parallel to the strong B_0-field. In order to receive a MR signal, M needs to be rotated to the plane perpendicular to B_0 (transversal plane). This is realized by exciting the hydrogen nuclei with a short radiofrequency (RF) pulse (B_1-field, perpendicular to B_0), whose frequency matches the *Larmor* frequency of hydrogen. The transversal component of the precessing net magnetisation M can be detected by a voltage induced in a receive element (known as free induction decay, FID) [2]. After the RF pulse, the spins return to their equilibrium state, losing the absorbed energy by interacting with the surrounding tissue. The duration that characterizes this interaction is called spin-lattice relaxation time T_1 and represents the time necessary for the return of M along the longitudinal axis. Secondly, interactions between the individual spins cause small fluctuations of the local magnetic field. This results in a loss of the phase coherence and thus a decay of the measurable transversal component of M. This relaxation process is characterized by the spin-spin relaxation time T_2. Moreover, inhomogeneities of the main magnetic field or susceptibility effects enhance the phase dispersion in the transversal plane. This accelerates the measurable decay and is characterized by the relaxation time T_2^* (with $T_2^* < T_2$). T_1 and T_2 are dependent on the atomic and molecular environment of the hydrogen atoms and therefore, together with the hydrogen density ρ, enable a distinction of human tissues [2, 19]. In general, increasing the B_0-field strength results in higher T_1 relaxation times, whereas T_2 relaxation times remain rather unchanged or exhibit a slight decrease. However, as B_0-field inhomogeneity increases at higher field strengths, T_2^* relaxation times decrease [2, 20].
Up to this point, the different parts of the human body emit a MR signal, but it is not possible to localize the source of the signal yet. For that, the concept of spatially varying magnetic fields is used: magnetic field gradients $G = \Delta B_2/\Delta r$. This means that at two different locations r_1 and r_2 the magnitudes of the applied magnetic fields $B_2(r_1)$ and $B_2(r_2)$ differ from each other. Following equation 2.1, this leads to a difference in

the resonance frequencies $w_{\mathrm{L}}(r_1) \neq w_{\mathrm{L}}(r_2)$ and offers a possibility to distinguish the origin of the acquired RF signal. When applying magnetic field gradients in all three spatial directions x, y and z, it is feasible to locate the origin of any MR signal emitted by a three-dimensional (3D) object. Note that all switched gradient fields superimpose on the main magnetic B_0-field: $B_{\mathrm{total}}(r) = B_0 + G(r) \cdot r$, with $r = (x, y, z)$.
In total, the main components of a MR scanner are its main magnetic B_0-field, the RF B_1-field for excitation, the gradient coil system for spatial encoding of the signal and a receive element for acquiring the MR data. However, MRI does not generate its images through an acquisition of the rapidly decaying FID. Instead, echoes are created, which is why the basic concept of the gradient echo pulse sequence is explained in the following, further clarifying the purpose of magnetic field gradients.

2.1.2 The gradient echo pulse sequence

Dependent on the application and aim of the study, different MR pulse sequences can be utilized to perform the MRI examination with (e.g. spin echo or gradient echo pulse sequences). In this thesis, two-dimensional (2D) MRI with spoiled gradient echo (GRE) pulse sequences was performed. Figure 2.1 shows a diagram of an exemplary Cartesian spoiled GRE sequence [21]. It demonstrates the various elements of the sequence by means of amplitude as a function of time within one repetition of the measurement. In order to excite a 2D slice and not the whole 3D volume, a slice selection gradient is switched along the axis that is perpendicular to the planned slice orientation. Simultaneously, a RF pulse is transmitted, matching the *Larmor* frequency of the spins located in the chosen 2D slice. This way, only the spins of the 2D slice are flipped to the transversal plane and emit a MR signal. The duration and amplitude of the RF pulse defines the flip angle (*FA*) and tunes the magnitude of the transversal component of the flipped magnetization. The slice selection gradient inherently causes a dephasing of the magnetic moments within the slice. This phase dispersion is refocused by a gradient with opposite polarity, played out subsequent to the slice selection gradient (slice selection rephaser) [21]. To encode the MR signal along the two remaining dimensions, phase encoding (PE) and frequency encoding (FE) gradients are used. The PE gradient is played out before data acquisition and ensures that the spins along the PE direction acquire a unique phase. The FE gradient is responsible for generating an echo of the MR signal. The FE dephasing gradient causes a phase dispersion along the FE direction. When the gradient moment of the

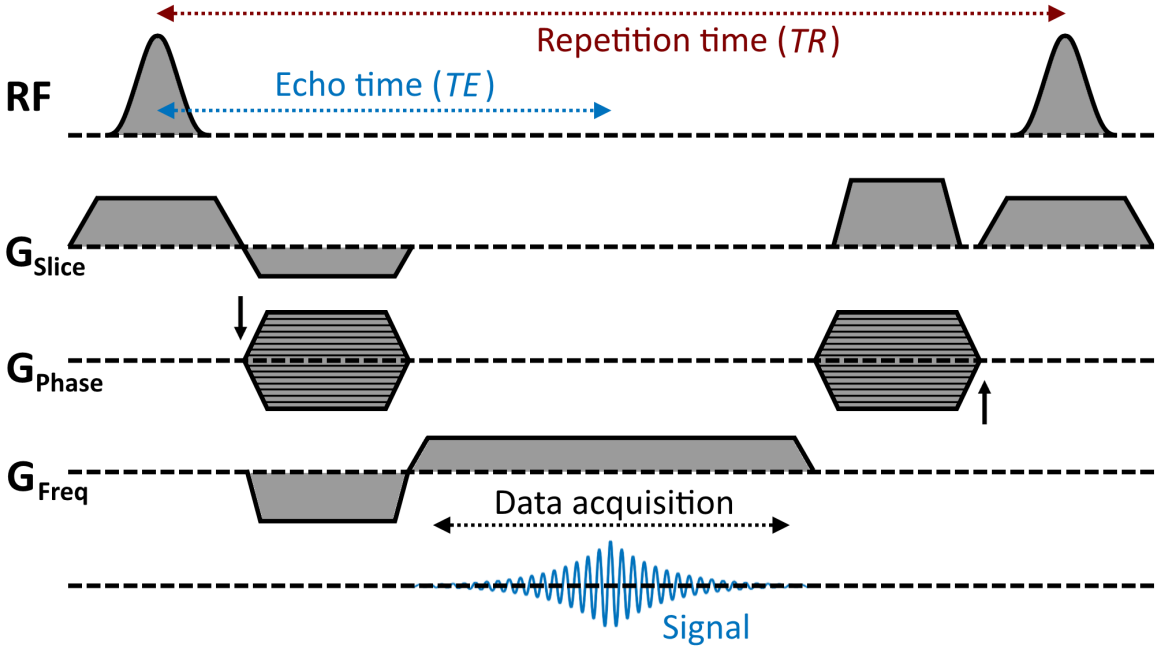

Figure 2.1: Pulse sequence diagram of an exemplary 2D Cartesian spoiled gradient echo sequence [21]. Slice excitation is performed by a RF pulse and a slice selection gradient. Phase encoding and frequency encoding gradients encode the signal along the remaining two dimensions. Data is acquired during the frequency encoding gradient, in which the signal echo is generated. A spoiling gradient and a rewinding gradient is played out on the slice selection axis and the phase encoding axis, respectively. Echo time (TE) is the time between the RF pulse and the signal echo, and repetition time (TR) the time between two consecutive RF pulses.

FE gradient (opposite polarity) compensates that of the FE dephasing gradient, the MR signal is again in phase and a signal echo is created. During the time of the FE gradient the MR data is acquired, which is why the FE gradient is also often named readout gradient. In order to dephase remaining transversal magnetization, gradient spoiling and RF spoiling can be applied. In Figure 2.1, a spoiling gradient is switched on the slice selection dimension at the end of the sequence block. RF spoiling means that each RF pulse is applied with a random or pseudo-random phase angle. In addition, RF spoiling usually requires a gradient rewinder that is switched on the PE axis to compensate the area of the PE gradient of the current repetition (denoted by the black arrows pointing in opposite directions) [2, 21]. After this sequence block is over, the next RF pulse is transmitted and the cycle of the switched gradients is repeated. To complete encoding along the PE dimension, the amplitude of the PE gradient is changed in every repetition. This is represented by the horizontal lines within the PE gradient. The time between the RF pulse and the signal echo is named

echo time (*TE*) and the time between two consecutive RF excitations repetition time (*TR*). *FA*, *TE* and *TR* can be adjusted by the examiner, which allows for various tissue contrast settings [2].
Another widely used GRE sequence in CMR is the balanced steady state free precession sequence (bSSFP) [22]. In contrast to spoiled GRE pulse sequences, in which the residual transversal magnetization is dephased, bSSFP sequences aim to preserve the transversal magnetization in a steady state by balancing all gradient moments. bSSFP imaging is often used in CMR, as it offers a high *SNR* and a very good contrast between blood and myocardium. However, the additional time needed for gradient balancing is disadvantageous for real-time applications. Furthermore, bSSFP sequences are prone to magnetic field inhomogeneities, which can result in dark banding artifacts. Hence, spoiled GRE sequences are more stable especially at high B_0-field strengths, which is why they were used for CMR at 3 T and 7 T in this study.

2.1.3 The spatial frequency domain (k-space)

Unlike other imaging modalities, MRI does not deliver the information directly in image space. Instead, MR data is acquired in the spatial frequency domain, which is referred to as k-space. The goal of the previously introduced pulse sequence is to sample the 2D k-space, which later is transformed to image space. The sampled k-space location $k_r(t)$ at a certain time point t can be calculated by integrating the gradient field $G_r(t)$ over time as follows [19]:

$$k_r(t) = \frac{\gamma}{2\pi} \cdot \int_0^t G_r(\tau)\, d\tau, \tag{2.2}$$

with $r \in \{x, y, z\}$ referring to the spatial dimension. If the amplitude of the switched FE gradient is constant over time and the same for all repetitions (as in Figure 2.1), the k-space is sampled in a *Cartesian* manner. This is the most common case in clinical MRI, as Cartesian data acquisition allows direct application of the *Fourier* Transform (FT) in order to obtain the image [23]:

$$\begin{aligned} \textit{Fourier}\text{ Transform (FT):} \qquad & S(f) = \int_{-\infty}^{\infty} s(r) \cdot \exp(-i2\pi f r)\, dr, \\ \text{Inverse }\textit{Fourier}\text{ Transform (iFT):} \qquad & s(r) = \int_{-\infty}^{\infty} S(f) \cdot \exp(i2\pi f r)\, df. \end{aligned} \tag{2.3}$$

The FT extracts the frequency components $S(f)$ that are present in a spatial signal $s(r)$. Analogously, the inverse FT (iFT) transforms the MR signal $S(f)$ acquired in the spatial frequency domain to image space $s(r)$ and thus yields the resulting image of the measured object. The FT is not limited to a certain domain but can be transferred to e.g. a time signal and its representation in the temporal frequency domain. Fast *Fourier* Transform (FFT) algorithms reduce the number of operations needed for an N-point signal from $O(N^2)$ for the discrete FT to $O(N \cdot \log N)$ [24].
An example of an acquired 2D k-space is depicted in the upper parts of Figure 2.2. The signal intensity in the k-space center is high and decreases towards the outer parts of k-space. iFFT of the shown k-spaces resulted in different representations of the measured object in the image domain. Figure 2.2 (A) shows the image quality when the entire acquired k-space is used for reconstruction. In Figure 2.2 (B) only the k-space center and in Figure 2.2 (C) only the k-space periphery was used for reconstruction. Intuitively, coarse structures are represented by low spatial frequencies, whereas the information of fine details at high resolution lies at high spatial frequencies. As in MRI

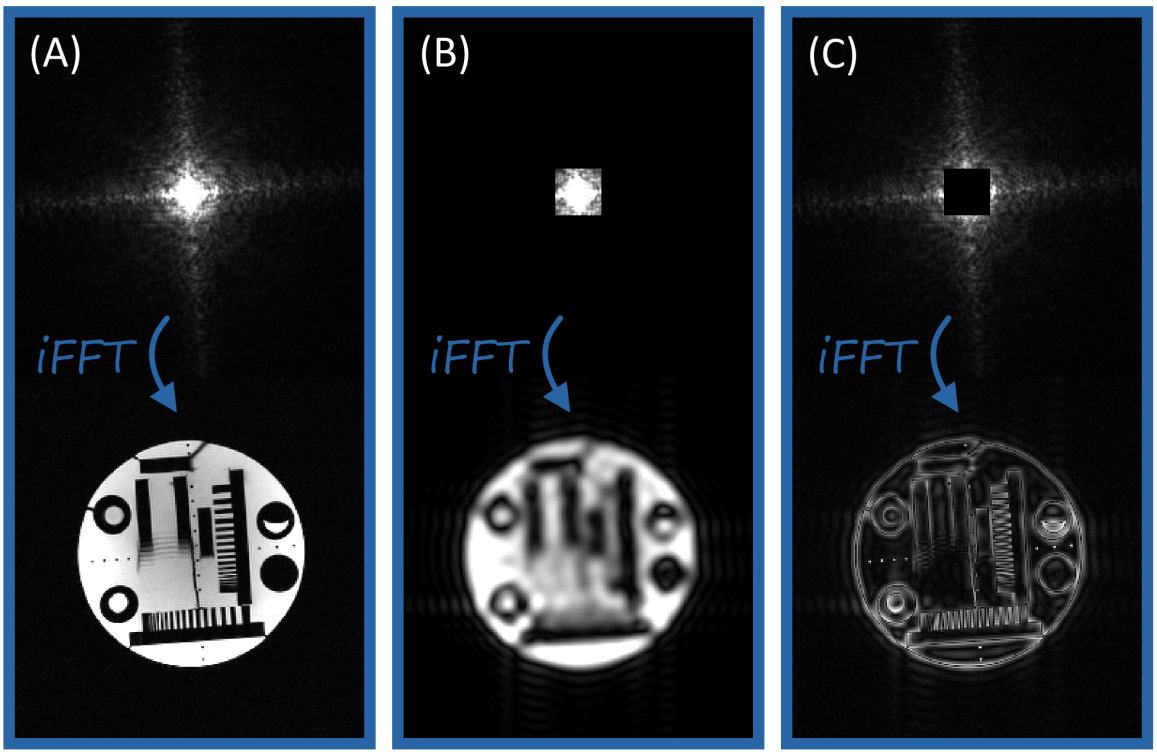

Figure 2.2: Spectral contributions of different k-space regions: The first row shows certain k-space entries that were transformed to image space (second row) via the iFFT. (A) represents the transformation of the whole k-space, (B) only of the k-space center and (C) of the k-space periphery.

there is neither unlimited amount of time nor data storage, the k-space can not be acquired in an infinite extent with an infinite amount of data points. Instead, the k-space needs to be sampled with finite data points up to a finite position in the k-space periphery. This naturally constrains the possible display of the examined object and corresponds to two important measurement parameters: the field of view (FOV) and the spatial resolution (Δr). The FOV is limited by the distance between two adjacent sampled k-space points $\Delta k = 1/FOV$ and the resolution by the maximum sampled k-space location $k_{\max} \approx 1/(2 \cdot \Delta r)$. If Δk is set such that the sampled FOV is smaller than the measured object, aliasing impairs the image quality. This is designated by the *Nyquist* theorem, stating that at a given sampling rate f_s only frequency contributions of an acquired signal up to $f_s/2$ can be digitized. If an undersized k-space extent is sampled (determined by $k_{\max}$), truncation artifacts that are also known as *Gibb's* ringing are present [2, 19]. This appeared in outlines in the truncated reconstructions of Figure 2.2 (B) and (C).

2.2 Parallel Imaging

After the basic principles of MRI, parallel imaging (PI) will be introduced. The application of PI techniques is a key element in accelerating the MRI acquisition process. They are based on the possibility to use multiple receive elements instead of only a single coil. There exist numerous PI methods, but all of them have in common that less k-space data is sampled as usually required by the *Nyquist* criterion (undersampling). Furthermore, the undersampling (or acceleration) factor R is limited by the number of coil elements. During image reconstruction, information about the individual coil sensitivities is exploited to obtain an unaliased image [25, 26]. The most prominent PI methods are called Sensitivity Encoding for Fast MRI (SENSE) [13] and Generalized Autocalibrating Partially Parallel Acquisitions (GRAPPA) [14]. Both play an essential role in todays clinical routine and thus are briefly summarized in this section.
Undersampling the k-space leads to aliasing in image space. This means that after the iFFT a reduced FOV is reconstructed with foldover artifacts present in PE direction. Dependent on R and the undersampling pattern, multiple pixels overlap and cannot be distinguished from one another. In SENSE, the coil sensitivity maps are utilized to unfold the reconstructed image in image space. This information is often received by performing an additional scan prior to the measurement.

In a simple example of two receive elements and $R = 2$ the unfolding process can be understood by the following equations [25]:

$$\begin{aligned} F_1 &= P_A \cdot C_{A1} + P_B \cdot C_{B1} \\ F_2 &= P_A \cdot C_{A2} + P_B \cdot C_{B2} \end{aligned} \tag{2.4}$$

F_1 and F_2 are the intensities of one folded pixel of the aliased reconstruction acquired by coil 1 and coil 2, respectively. P_A and P_B are the values for the pixels of the unfolded image at position A and B. C_{A1}, C_{B1}, C_{A2} and C_{B2} are the coil sensitivities of coil 1 and 2 at the postitions A and B. In this way the system of equations can be solved as there are two equations and only two remaining unknowns (P_A and P_B).
In contrast to SENSE, GRAPPA fills the missing data points already in k-space. Also, an exact knowledge of the coil sensitivity maps is not necessary. Instead, GRAPPA exploits the principle that the weighting of acquired single-coil data by their respective coil sensitivity profile represents a spreading of information to neighboring points in k-space. This means that the sampled k-space locations additionally carry information about the neighboring k-space locations. As a consequence, appropriate combination of sampled k-space data can be used to fill the k-space voids that where left out in the undersampled acquisition. However, these GRAPPA weighting factors first need to be determined. This calculation can be based on a low-resolution reference dataset that can be received through a separate scan or inclusive to the accelerated scan (auto-calibration signal ACS). A GRAPPA kernel is defined by selecting an appropriate k-space range and subsequently the GRAPPA weights of each coil element can be calculated by sliding the GRAPPA kernel through the corresponding ACS data. This GRAPPA weight set can then be transferred to the undersampled acquisition in order to fill the missing voids in the k-space data. Unaliased single-coil images can now be reconstructed from the complete k-spaces via the iFFT and ultimately combined to a final image [25, 27].

2.3 Non-Cartesian data acquisition

As described in Section 2.1.3, a conventional MR scan is performed with Cartesian data acquisition (see Figure 2.3 A). However, sampling the k-space line by line is rather inefficient as it takes a long time to cover the 2D k-space, including the k-space edges. In addition, the sampling density is uniform, whereas most of the information is located in the k-space center. Therefore, research aims at different approaches of k-space trajectories to increase the overall efficiency. In general, there exist many alternatives of covering a 2D k-space in a non-Cartesian manner. Some of the most common are summarized schematically in Figure 2.3: radial (B), spiral (C) as well as

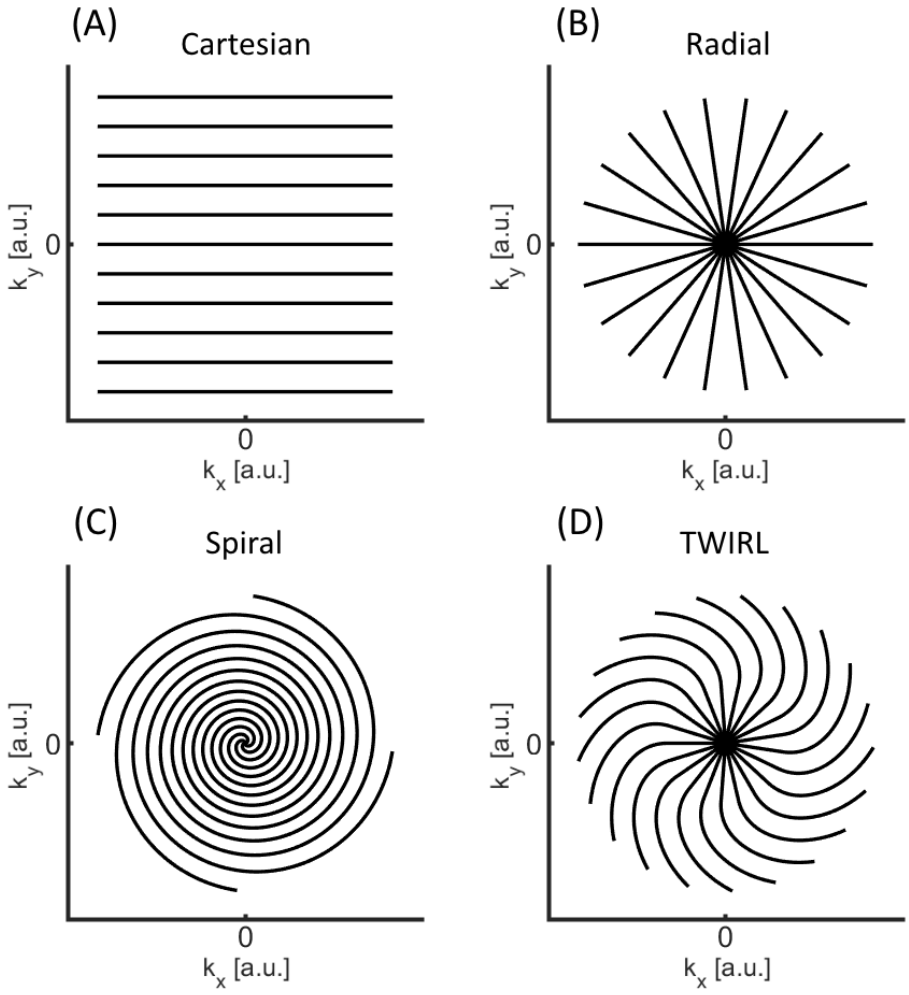

Figure 2.3: Summary of common 2D k-space sampling schemes: Cartesian (A), radial (B), spiral (C) and an exemplary hybrid trajectory dubbed TWIRL (twisting radial lines) (D) [28].

a combination of both, e.g. twisting radial lines (TWIRL) (D) [28]. A major disadvantage of radial sampling are large voids in the k-space periphery, which may violate the *Nyquist* criterion and therefore limit not only the spatial resolution but also undersampling strategies. Thus, the main focus of this project lied on optimizing spiral sampling schemes and to test the efficiency of hybrid trajectories as e.g. the TWIRL sampling pattern. The theory of both trajectory categories is explained in the following Subsections 2.3.1 and 2.3.2.

2.3.1 Spiral k-space trajectories

Spiral k-space trajectories offer numerous advantages as compared to Cartesian imaging [29]. Firstly, data acquisition starts in the k-space center, which not only increases the *SNR* but also facilitates ultra-short echo time (UTE) applications [30]. Interleaved sampling schemes offer self-navigating possibilities, e.g. to correct for motion-induced phase variations in diffusion tensor imaging [31] or to track cardiac or respiratory motion in cine imaging [32]. In addition, spirals provide some inherent refocusing of flow- and motion-induced phase errors [33–35]. Furthermore, the k-space is sampled more efficiently as spirals allow to cover a larger pathway through k-space in each readout, i.e. the readout gradients are able to exploit todays powerful gradient systems. Moreover, a spiral trajectory can be designed very flexibly. It can be implemented as a single-shot sequence [36–38], meaning that the entire 2D k-space is sampled after only one RF excitation. Therefore, it is considered as one of the fastest MRI techniques. On the other hand, interleaved multi-shot sequences [32, 39] enable to tune the number of spiral interleaves per 2D k-space as well as their duration. In addition, the trajectory can be equipped with a constant density [40] (*Archimedean*) or with a variable density [41, 42]. Generally, a spiral trajectory can be formulated as [29, 43]:

$$k(t) = \lambda \cdot \tau(t)^{\alpha} \cdot \exp\left[i\omega\tau(t)\right]. \tag{2.5}$$

$k(t)$ is the complex k-space location, $\tau(t) = [0, 1]$ is a function of time t and α defines the density ($\alpha = 1$ for *Archimedean* and $\alpha \neq 1$ for variable density). λ is defined as $\lambda = N/(2 \cdot \mathrm{FOV})$ with the matrix size N and ω is defined as $\omega = 2\pi n$ with the number of spiral interleaves n.

2.3.2 Twisting radial lines (TWIRL) k-space trajectories

The fact that data acquisition in center-out spiral trajectories constantly starts in the k-space origin has multiple advantages, e.g. a shortened minimum TE or reduced sensitivity to motion. On the other hand, high oversampling of the central region of k-space is inefficient as it results in longer acquisition times [44, 45]. Therefore, it seems more efficient to move in a straight line away from $k = 0$, which is why hybrid trajectories that arise out of the combination of radial and spiral sampling were additionally studied. Exemplary implementations are the twisting radial lines trajectory (TWIRL) [28], winding hybrid interleaved radial lines trajectory (WHIRL) [44] or trajectories created by a multi-objective genetic algorithm [46]. In this work, the TWIRL algorithm was tested and applied to CMR. The TWIRL k-space trajectory consists of four different stages, constrained by the maximum gradient amplitude $G_{\max}$ and slew-rate $S_{\max}$, as well as a minimum data sampling density and a maximum k-space extent $k_{\max}$ (determined by FOV and spatial resolution). Furthermore, two constants r_m and p were introduced, which refer to the radius of $k_{\max}$ and the fraction of radial interleaves needed to fully sample the 2D k-space with the TWIRL interleaves, respectively. The latter ultimately controls the starting point of twisting. Note that r_m has the unit [Ts/m], it does not equal the radius of $k_{\max}$.

1. Stage: the first part of the TWIRL readout, starting at $k = 0$, is a gradient ramp with duration t_1, limited by $G_{\max}$ and $S_{\max}$.

2. Stage: secondly, a region with constant gradient amplitude continues moving through k-space in a straight line with duration t_2 satisfying

$$t_2 = \frac{\sqrt{(S_{\max} \cdot p \cdot r_m)^2 - G_{\max}^4}}{(G_{\max} \cdot S_{\max})} - \frac{G_{\max}}{(2 \cdot S_{\max})}, \qquad (2.6)$$
$$\text{with} \qquad p \cdot r_m \geq (\sqrt{5} \cdot G_{\max}^2)/(2 \cdot S_{\max})$$

   to prevent complex values for t_2.

3. Stage: a slew-rate-limited transition region connects the linear with the twisting part of the trajectory by creating a circular arc that passes through an angle ϑ with the two generating gradients $G_{\mathrm{x}}(t_3)$ and $G_{\mathrm{y}}(t_3)$:

$$\vartheta = \arcsin\left[G_{\max}^2/(p \cdot r_m \cdot S_{\max})\right] \qquad (2.7)$$

$$G_{\mathrm{x}}(t_3) = G_{\max} \cdot \cos \frac{(S_{\max} \cdot t_3)}{G_{\max}} \qquad \text{and} \qquad G_{\mathrm{y}}(t_3) = G_{\max} \cdot \sin \frac{(S_{\max} \cdot t_3)}{G_{\max}}$$
$$\text{with} \qquad 0 \leq t_3 \leq (G_{\max} \cdot \vartheta)/S_{\max}. \tag{2.8}$$

4. Stage: the last stage ensures twisting of the trajectory with uniform radial sampling density, given by $dr(t)/dt \propto 1/r(t)$ with the spirals radial position $r(t)$. Solving this differential equation by using polar coordinates leads to the following generating gradients:

$$G_{\mathrm{x}}(t_4) = G_{\max} \cdot \cos\left(\sqrt{\frac{2 \cdot G_{\max} \cdot t_4}{p \cdot r_m}} + \vartheta_0\right)$$
$$\text{and} \qquad G_{\mathrm{y}}(t_4) = G_{\max} \cdot \sin\left(\sqrt{\frac{2 \cdot G_{\max} \cdot t_4}{p \cdot r_m}} + \vartheta_0\right), \tag{2.9}$$
$$\text{with} \qquad \frac{G_{\max}^3}{2 \cdot p \cdot r_m \cdot S_{\max}^2} \leq t_4 \leq \frac{(1-p^2) \cdot r_m}{2 \cdot p \cdot G_{\max}}.$$

The start and end conditions of t_4 guarantee that the time derivative of $G_{\mathrm{x}}(t_4)$ and $G_{\mathrm{y}}(t_4)$ does not exceed $S_{\max}$ for any ϑ_0.

An illustration of the four stages together with trajectory modifications that were made for the measurements will be presented in methods Section 3.2.2. Despite all the advantages that are offered by spiral or TWIRL sampling patterns, they still lack popularity in clinical routine as they are more complex than Cartesian imaging. Due to the fact that the k-space is no longer sampled uniformly on a Cartesian grid, simple reconstruction via the FFT is not possible. Moreover, non-Cartesian MRI is prone to distortion and blurring artifacts that can arise due to gradient imperfections or off-resonance effects caused by magnetic field inhomogeneities, concomitant fields or chemical shift [29, 47, 48]. Also, the PI techniques presented in Section 2.2 must be extended and adapted to non-Cartesian trajectories [49–51]. The following subsections thus clarify how reconstruction of non-Cartesian data can be performed and which approach was used to correct for typical non-Cartesian imaging artifacts.

2.4 Image reconstruction in non-Cartesian MRI

There exist different strategies to reconstruct data that were sampled with non-Cartesian k-space trajectories. Many methods still use the FFT for image reconstruction by resampling the acquired data to a Cartesian grid beforehand, called *nonuniform* FFT (or short NUFFT) [24, 52, 53]. Resampling can be performed either by grid-driven or data-driven interpolation. The most common reconstruction technique is a data-driven interpolation called *gridding*, which is illustrated in Figure 2.4 [52, 54]. The sampled data points (blue dots) form a given non-Cartesian k-space trajectory (dashed blue curve) and need to be resampled onto the points of the Cartesian grid. This is done by a well-chosen convolution kernel (orange) which point-wise distributes weights to adjacent Cartesian grid points dependent on their distance (black arrows). A well established framework presented by *Jeffrey A. Fessler* uses min-max interpolation with a Gaussian or Kaiser-Bessel function [24, 53]. A crucial step before data interpolation is to correct the sampling nonuniformity that is present in spiral imaging [55, 56]. In many applications the sampling density decreases from the k-space origin towards the periphery. This needs to be compensated as an unintentional, unbalanced weighting of the spatial frequency content can result in corrupted images. An efficient

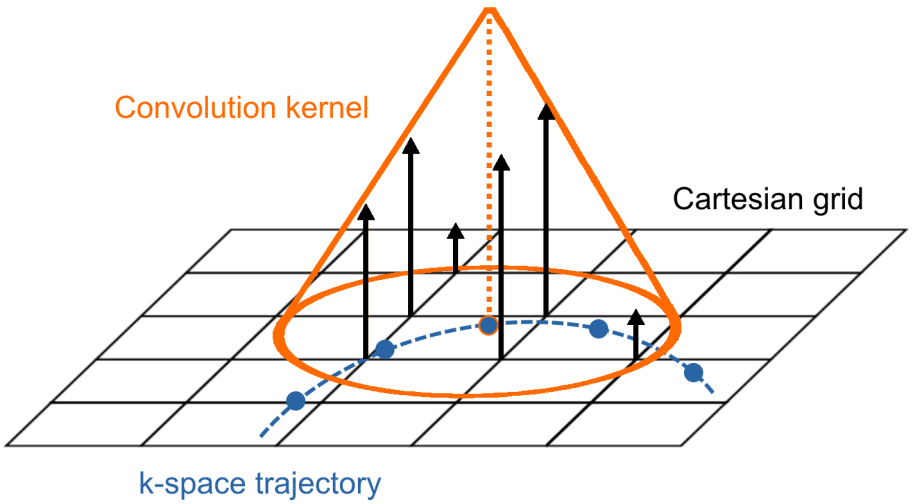

Figure 2.4: Schematic illustration of the gridding procedure, following Ref. [52]. The amplitude of the non-Cartesian k-space position (blue) is distributed to the surrounding positions of the Cartesian grid (black) with weights (black arrows) given by a certain convolution kernel (orange), e.g. a Kaiser-Bessel interpolator.

method is the determination of a *Voronoi* diagram, which means that the density is estimated by the area of cells surrounding each data point [55]. A different approach to reconstruct non-Cartesian data uses the concept of GRAPPA (see Section 2.2) as a basis to shift the sampled k-space positions to a Cartesian grid, dubbed GRAPPA operator gridding (GROG) [50]. Here, spiral k-space positions act as the source points and Cartesian grid positions as the missing k-space voids that need to be filled. In contrast to convolution gridding introduced above, no separate density compensation must be calculated as resampled points that fall on the same Cartesian position simply can be averaged. However, note that GROG can only be used if the data was acquired with a multi-coil receive element and that a Cartesian calibration dataset either needs to be acquired separately or calculated from the image data itself. Further details about the applied image reconstruction will be presented in methods Section 3.6.

2.5 Compressed Sensing

Besides PI, the field of compressed sensing (CS) represents a recent milestone in accelerating the MRI process. CS is based on the mathematical concept of finding sparse solutions for underdeterminded systems of linear equations [57, 58]. A vector is considered to be sparse if most of its entries equal zero and only some entries are unequal to zero and thus hold the entire information [59]. In general, sparsity in some domain forms the basis of data compressibility as e.g. exploited by the prominent image compression method JPEG. CS was transferred to MRI by Lustig et al. [15] as sparsity is also present in a given transform domain of an MR image, e.g. spatial finite-differences, the discrete cosine transform, wavelet transform, the temporal frequency domain or the image space itself. The question motivating the usage of CS in MRI is: if k-space data is compressible posterior, shouldn't it be possible to measure only a subset instead of the entire k-space? The key prerequisites to do so are [15, 59]:

1. the data must be compressible, i.e. there must be a sparse representation in some transform domain,

2. in which pseudo-random undersampling of the k-space results in incoherent aliasing,

3. and reconstruction is done by a non-linear recovery procedure that enforces sparsity and data consistency.

In the case of a pseudo-random undersampling pattern, energy will additionally spread from non-zero signal values towards points with former zero signal intensity, similar to noise. The non-linear recovery scheme can be formulated by the following minimization problem [15]:

$$\min \|\Psi x\|_1 \ , \ \text{such that} \ \ \|\mathcal{F}_u x - d\|_2 < \tau. \tag{2.10}$$

The linear operator Ψ transforms the reconstructed image x from image domain to the sparse domain. $\mathcal{F}_u$ stands for the undersampled FFT and d for the measured k-space data. Data consistency is ensured by the error tolerance τ. Note that minimizing the ℓ_1-norm ($\|r\|_1 = \sum_i |r_i|$) produces sparser results than minimizing the ℓ_2-norm ($\|r\|_2 = (\sum_i r_i^2)^{1/2}$). However, for data consistency the ℓ_2-norm is preferred as large errors are penalized stronger than small errors [59].

In this work, MRI of the heart is the main application. Dynamic processes are well suited for CS as the temporal dimension offers an excellent basis for sparsifying transforms. Otazo et al. [60] proposed a low-rank plus sparse (L+S) model for the reconstruction of undersampled dynamic MRI, which decomposes the data matrix d in a low-rank matrix L (background component) and a sparse matrix S (dynamic component):

$$\min_{L,S} \frac{1}{2} \|E(L+S) - d\|_2^2 + \lambda_L \|L\|_* + \lambda_S \|TS\|_1 \,, \tag{2.11}$$

with the two regularization parameters λ_L and λ_S. A matrix exhibits a low rank, if it can be expressed by only a few non-zero singular values. E is the multi-coil encoding operator, which - additionally to the undersampled FFT $\mathcal{F}_u$ from equation 2.10 - includes coil sensitivity information. $\|L\|_*$ is the nuclear norm of the matrix L corresponding to the sum of singular values. In the case of cardiac cine imaging, the matrix S already can have a sparse representation. However, it can be further sparsified by an additional transform T, which e.g. performs a FFT along the temporal dimension. In general, the minimization problem can be solved by different approaches. An iterative soft thresholding algorithm was used in this thesis as proposed by Otazo et al. [60].

In soft thresholding, components n (complex valued) with an absolute value higher than the threshold λ (real valued) are reduced by λ, whereas all other entries are set to zero. This soft thresholding operator can be formulated as [60, 61]:

$$\mathrm{T}_\lambda(n) = \max(|n| - \lambda, 0)\frac{n}{|n|}. \tag{2.12}$$

Note that the complex phase remains unchanged. An alternative approach to soft thresholding could be e.g. a non-linear conjugate gradients descent algorithm as applied by Lustig et al. [15].

2.6 The Gradient System Transfer Function (GSTF)

The maximum gradient slew-rate S_{max} and gradient amplitude G_{max} are two physical quantities that characterize the limitations of spatially and temporally varying magnetic field strengths. The gradient systems used in this study ($S_{max} = 200\,\mathrm{T/m/s}$ and $G_{max} = 80\,\mathrm{mT/m}$) enable rapidly oscillating magnetic field gradients in the range of milliseconds and thus facilitate the implementation of non-linear pathways throughout the k-space. However, non-linear k-space trajectories still play a minor role in clinical routine. As a consequence, the scanner hardware is not entirely optimized for their application. When e.g. a spiral readout gradient is played out by the scanner, the oscillating waveform is not transferred properly. Instead, imperfections of the dynamic gradient system result in small but significant deviations of the gradient output. This means that the sampled k-space does not match the calculated trajectory, which often causes artifacts in spiral imaging [62–64]. These artifacts do not appear in conventional Cartesian imaging, because the gradient errors mostly result in a shift of the Cartesian k-space. This corresponds to an additional phase in image space, which does not affect the magnitude representation [62]. The main source of gradient errors are magnetic fields arising due to eddy currents, which are induced in conducting structures of the magnet. In addition, amplifier inaccuracies, timing errors or the coupling of acoustic and main magnetic field fluctuations lead to imperfect transfer behavior when performing a MR scan [62, 65–68]. Under the assumption of a linear and time-invariant MR gradient system, the transfer characteristics can be comprehensively described by the Gradient System Transfer Function (GSTF) [69]. The GSTF is a complex func-

tion that reveals the transfer behavior of magnitude and phase of a given gradient input dependent on its frequency. This function is unique for each gradient system and exhibits only little change over time [62, 70]. The equivalent of the GSTF in the temporal domain is called Gradient Impulse Response Function (GIRF).
There exist different approaches to determine a GSTF, such as measurements performed with a field camera [69, 71] or with a phantom [62, 70, 72–75]. The detailed description of the approach used in this work is presented in methods Section 3.1. After the GSTF was determined, convolution of a non-Cartesian gradient waveform with the appropriate GSTF yielded a corrected gradient waveform, which can be utilized for trajectory correction in post-processing. Convolution of a non-Cartesian gradient waveform with the inverse GSTF led to the initially intended gradient output (pre-emphasis).

2.7 Cardiovascular MRI (CMR)

The heart is responsible for sufficient oxygen supply by regularly pumping blood to the different parts of the human body. An impairment of the cardiovascular system can have severe health consequences, i.e. cardiovascular diseases are the main causes of death worldwide. Coronary artery disease, cardiac arrhythmia, hypertension, cardiomyopathy or congenital heart disease are examples of diseases that limit cardiac function or alter heart structures [76]. It is of great importance to optimize clinical cardiac imaging tools, because they play an essential role in the diagnosis of cardiovascular diseases. Ultrasound echocardiography and cardiovascular MRI (CMR) are the two most common noninvasive imaging modalities for the evaluation of cardiac function and morphology. Echocardiography is the method of choice for an immediate determination of cardiac chamber size and function, promoted by its availability and portability [77, 78]. However, CMR enables a more comprehensive and profound analysis including detailed information about the different tissues, chamber volumes and morphology. Accurate and reproducible quantification of the different parameters strengthen diagnosis and treatment of cardiovascular diseases, i.e. CMR represents the gold standard for the quantification of left- and right-ventricular volumes and ejection fraction [79–81].
Imaging moving tissue, e.g. due to respiratory or cardiac motion, constitutes a particular challenge in MRI. A typical cardiac MR examination is based on a Cartesian GRE sequence, acquired during multiple breath holds of the patient using an electro-

cardiogram (ECG)-signal for gating. This procedure is illustrated in Figure 2.5 (B) using an ideal cardiac sinus rhythm. In healthy participants, the human heart contracts approximately 70 times per minute. Conventional MR sequences are unable to display the beating heart in real time as they need too much time for data acquisition. In gated imaging the data is acquired along several consecutive heart beats in order to determine one averaged cardiac cycle. In Figure 2.5 (B) this segmentation process is explained for the simplified example of four frames that are used to depict the cardiac cycle (represented by the four colours: blue, orange, green and red). In reality, a frame rate of > 20 frames per second, which corresponds to a temporal resolution of $< 50\,\text{ms}$, is recommended to evaluate cardiac function [82, 83]. Here, the data is acquired over a duration of four heartbeats. At unique positions within the cardiac cycle, different portions of the k-space are sampled. After the measurement, one cardiac frame is generated by summing up the four sub-k-spaces. In Figure 2.5 (B) this is exemplarily shown for the blue segments. During the measurement, the recorded

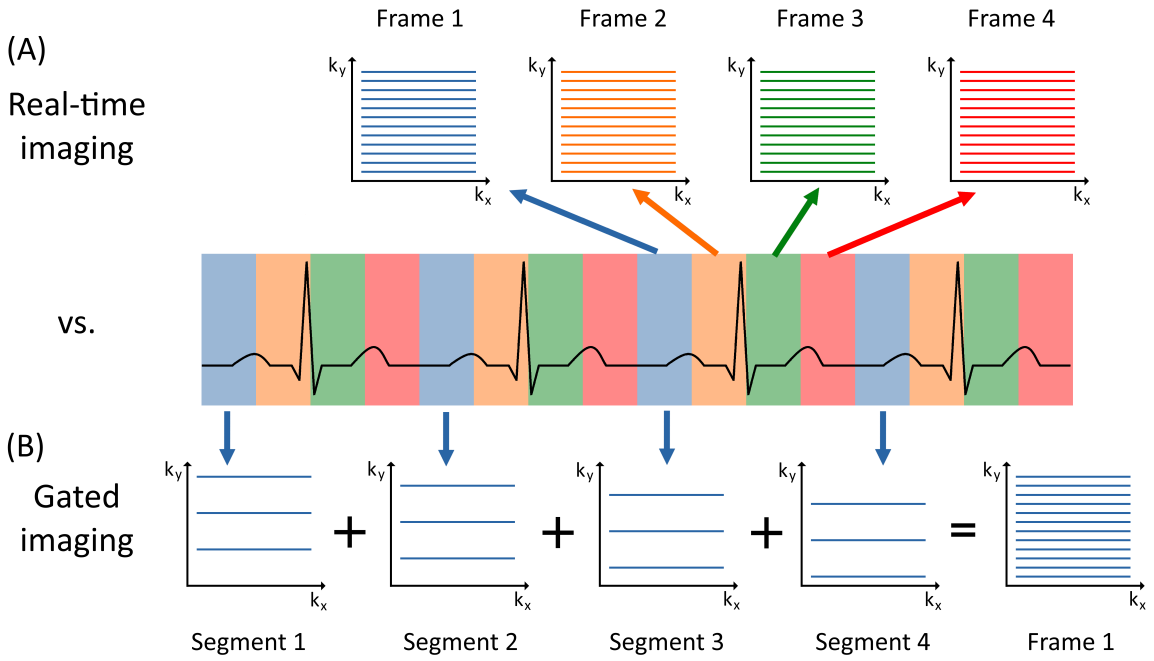

Figure 2.5: The principles of cardiac real-time imaging and gated imaging are depicted in (A) and (B), respectively. To simplify, an ideal sinus rhythm is divided into four segments, represented by the colors blue, orange, green and red. In (A), the data acquired in each segment needs to be sufficient to reconstruct one frame. In (B), the acquired data of four consecutive heart beats is summed up to receive one averaged cardiac cycle (exemplarily demonstrated for the blue segments).

ECG serves as a trigger signal to match the sampled data with the position of the sinus rhythm. In addition, data always must be acquired in the same breathing state (breath hold usually in expiration). Alternatives to using an ECG as trigger signal are self-gating approaches [84, 85]. They use information of the k-space center (direct current (DC) signal) measured by coils adjacent to the heart to assign the acquired data to the cardiac motion. This can be achieved by integrating a separate ADC without any encoding gradients or by taking advantage of center-out sampling schemes, in which the k-space center is repeatedly measured at the beginning of each readout.
In contrast to gated imaging, real-time imaging aims to map each wave of the sinus rhythm individually. This is illustrated in Figure 2.5 (A). Here, the k-space data must be acquired sufficiently fast such that a unique image can be reconstructed for each real-time frame. For consistency, this is again depicted for the case of Cartesian sampling. To give an example, Beer et al. [86] applied spatiotemporal sensitivity encoding to demonstrate that real-time CMR in free breathing and without ECG-triggering can be realized with Cartesian trajectories. However, the results were limited by a comparatively low spatial resolution. To further increase the quality of real-time CMR, k-space sampling schemes can be modified. Non-Cartesian trajectories represent a promising basis to facilitate results with high spatiotemporal resolution, not only for real-time imaging [87–92], but also for gated imaging [32, 41, 84, 85, 93–95].

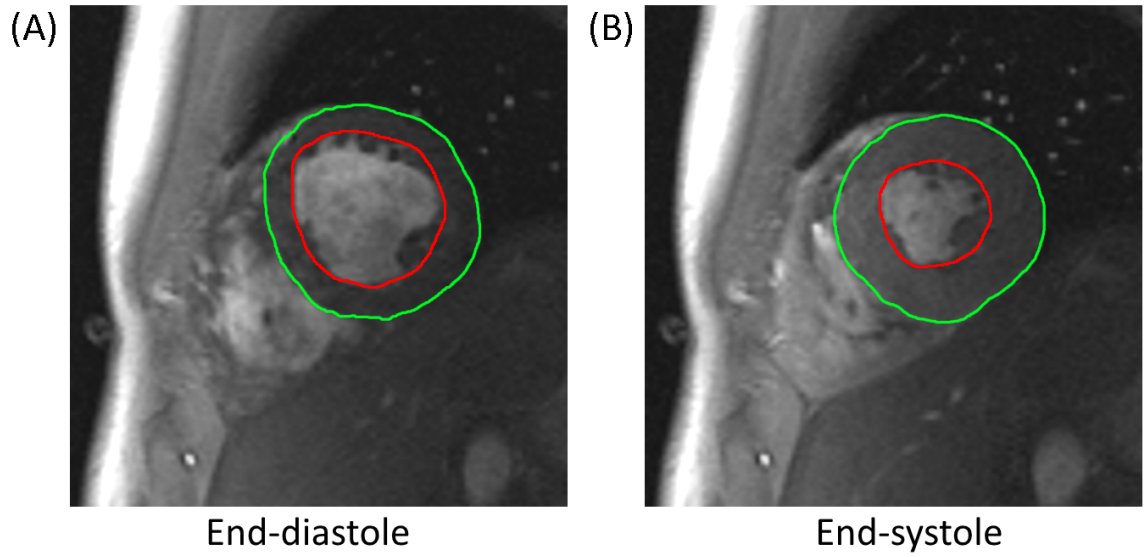

Figure 2.6: Midventricular short-axis slice in end-diastole (A) and end-systole (B). Determination of epicardial (green) and endocardial (red) borders in order to calculate mass, volumes and ejection fraction of the left ventricle.

To assess quantitative information of cardiac function in CMR, a stack of multiple slices in short-axis (SAX) orientation can be acquired. Mass and volumes of the left ventricle can be calculated by determining the epicardial and endocardial borders in end-diastole and end-systole for all slices. This is demonstrated in Figure 2.6 (A) and (B) for an exemplary midventricular SAX slice of a healthy volunteer. Epicardium and endocardium are marked in green and red, respectively. End-diastolic volume (EDV) and end-systolic volume (ESV) are defined by the area within the endocardial border, multiplied by the slice thickness, respectively. Subsequently, important parameters such as stroke volume (SV) and ejection fraction (EF) follow from [96]:

$$\begin{aligned} SV\,[\mathrm{ml}] &= EDV - ESV \\ EF\,[\%] &= \frac{SV}{EDV} \cdot 100. \end{aligned} \tag{2.13}$$

Myocardial mass can be calculated by additionally evaluating the area within the epicardial border.

3 Methods

3.1 GSTF measurements

All measurements of this work were performed at two different MR scanners, a 3 T and a 7 T system (MAGNETOM Prisma$^{\text{fit}}$ and Terra, Siemens Healthcare, Erlangen, Germany). Both scanner models are equipped with a gradient system allowing for a maximum slew-rate of $S_{max} = 200\,\text{T/m/s}$ and a maximum gradient amplitude of $G_{max} = 80\,\text{mT/m}$. Nevertheless, the scanner-specific GSTF needed to be determined for both systems separately, but following the same procedure. A phantom-based approach was used in this project as presented e.g. in Refs. [62, 70, 73]:
A homogeneous, spherical phantom was placed in the isocenter of the MR scanner. A series of N input gradients $g^i_{\text{in}}(t)$ ($i \in \{1, 2, ..., N\}$) that cover a large frequency spectrum are played out in two slices with distance SD equidistantly from the isocenter. Their phase evolutions $\phi^i_1(t)$ and $\phi^i_2(t)$ are measured together with reference scans $\phi^i_{1,\text{ref}}(t)$ and $\phi^i_{2,\text{ref}}(t)$ that correspond to zero gradient amplitude. The true gradient output $g^i_{\text{out}}(t)$ can be calculated by subtraction of the respective phases with subsequent time derivation:

$$g^i_{\text{out}}(t) = \frac{1}{SD \cdot \gamma} \cdot \frac{d}{dt} \left\{ \left[\phi^i_1(t) - \phi^i_{1,\text{ref}}(t) \right] - \left[\phi^i_2(t) - \phi^i_{2,\text{ref}}(t) \right] \right\}, \tag{3.1}$$

with the gyromagnetic ratio γ for hydrogen. With the FFT of the gradient input $G^i_{\text{in}}(f) = \mathcal{F}\left[g^i_{\text{in}}(t)\right]$ and output $G^i_{\text{out}}(f) = \mathcal{F}\left[g^i_{\text{out}}(t)\right]$, the frequency dependent $\text{GSTF}(f)$ follows from:

$$\text{GSTF}_{k,l}(f) = \frac{\sum_i G^{i,k}_{\text{in}}(f)^* \cdot G^{i,l}_{\text{out}}(f)}{\sum_i |G^{i,k}_{\text{in}}(f)|^2}. \tag{3.2}$$

k and l are the input and output channels, respectively ($k, l \in \{x, y, z\}$). In this work, only the GSTF self-terms (i.e. $k = l$) were determined and utilized for correcting the non-Cartesian gradient waveforms. This means that the data was measured on the same physical axis as the triangular input gradients were played out. $N = 12$ triangular input gradients were set up with a constant slew-rate of $S = 180\,\mathrm{T/m/s}$ but with varying amplitude specified by the gradient duration, which covered a range of $100-320\,\mu\mathrm{s}$. Further parameters of the GSTF measurements at both scanner models are summarized in Table 3.1: dwell time (DT), repetition time (TR), slice thickness (ST), slice distance (SD), flip angle (FA), signal averages (SA) and measurement time (MT). The longer TR and smaller ST at 7 T were chosen as T_1 relaxation times and magnetic field inhomogeneity increase at higher field strengths, respectively [97]. Due to the higher SNR at 7 T, fewer SA were chosen, which additionally kept the MT constant as compared to the 3 T measurements.

	GSTF measurement parameters						
	DT [µs]	TR [s]	ST [mm]	SD [mm]	FA [°]	SA	MT [h]
3 T Prisma	8.7	1.0	3.0	33	90	100	4.0
7 T Terra	8.7	2.0	2.0	33	90	50	4.0

Table 3.1: Parameters of the Gradient System Transfer Function (GSTF) measurements, performed at the Prisma and the Terra scanner, respectively: dwell time (DT), repetition time (TR), slice thickness (ST), slice distance (SD), flip angle (FA), signal averages (SA) and measurement time (MT).

3.2 Design of non-Cartesian k-space trajectories

3.2.1 Spiral k-space trajectories

Spiral imaging gradients were designed with a publicly available MATLAB (The-MathWorks, Natick, MA) toolbox, which was released by *Brian Hargreaves* [98]. The following input parameters can be adjusted to flexibly create any desired spiral k-space trajectory: maximum slew-rate ($S_{\max}$ in [G/cm/s]), maximum gradient amplitude ($G_{\max}$ in [G/cm]), sampling increment (T in [s]), number of spiral interleaves

necessary for *Nyquist* sampling N, FOV coefficients ($F_{\text{coeff}} = \{F_1,\ F_2\}$ in [cm]) and spatial resolution (res in [mm]). For F_{coeff}, two values can be set that correspond to the FOV at the k-space center F_1, which is reduced by F_2 at the k-space maximum with linearly decreasing density. In the case of $F_2 = 0$, an *Archimedean* spiral with constant density is created.

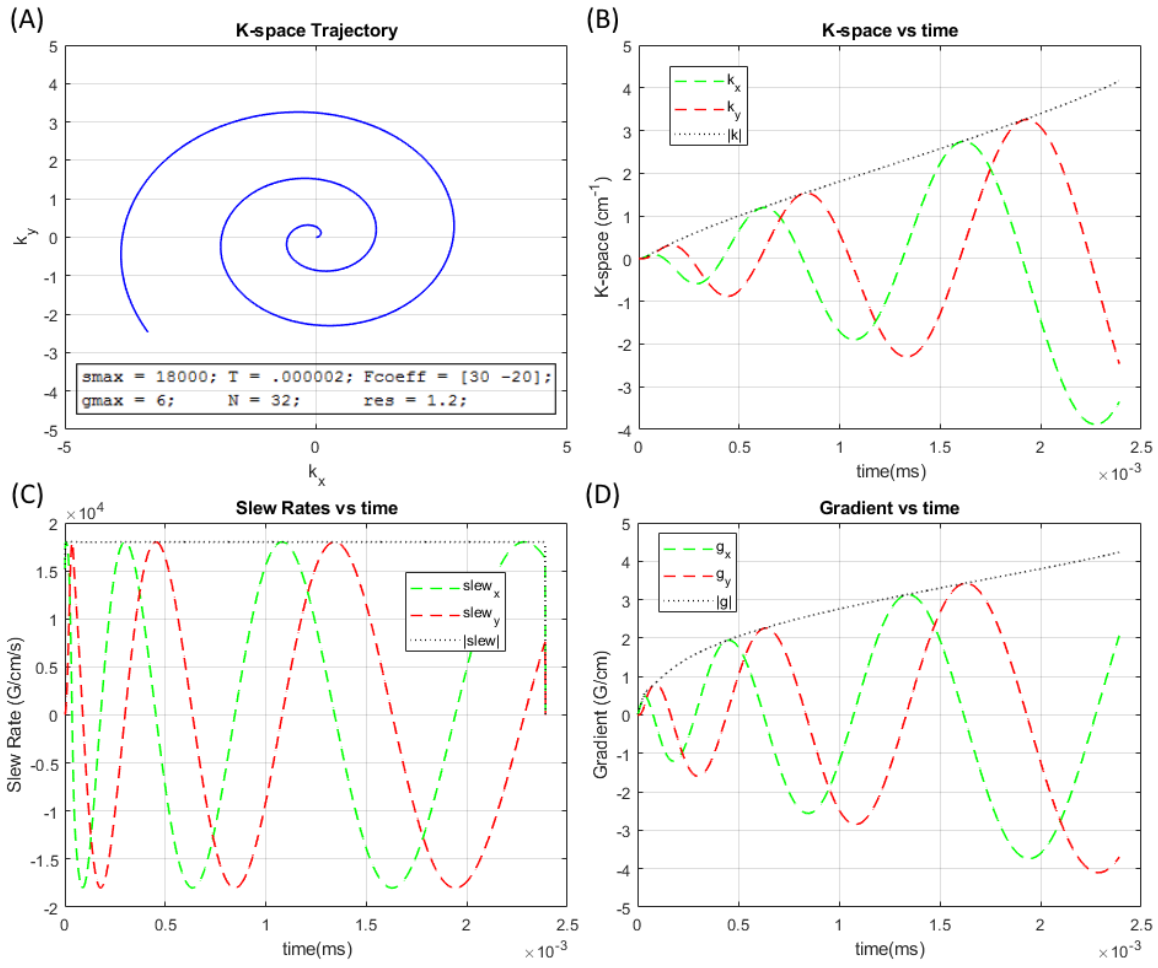

Figure 3.1: Spiral k-space trajectory design using the MATLAB toolbox of *Brian Hargreaves* [98]. Trajectory as well as time courses of k-space, slew-rates and gradients are depicted in (A), (B), (C) and (D), respectively. In (B), (C) and (D), the contributions of the two readout dimensions (here x and y) together with the absolute value are shown in green, red and black, respectively. The inlay of (A) summarizes the exemplary chosen toolbox input parameters of maximum slew-rate (S_{max} in [G/cm/s]), maximum gradient amplitude (G_{max} in [G/cm]), sampling increment (T in [s]), number of spiral interleaves (N), FOV coefficients (F_{coeff} in [cm]) and spatial resolution (res in [mm]).

In Figure 3.1 the framework is introduced for an exemplary set of input parameters, which are summarized in the inlay of (A). They read: $S_{\max} = 18\,000\,\mathrm{G/cm/s} \equiv 180\,\mathrm{T/m/s}$, $G_{\max} = 6\,\mathrm{G/cm} \equiv 60\,\mathrm{mT/m}$, $T = 2 \cdot 10^{-6}\,\mathrm{s}$, $N = 32$, $F_{\mathrm{coeff}} = \{30,\ \text{-}20\}\,\mathrm{cm}$ and $res = 1.2\,\mathrm{mm}$. The first spiral interleave of the resulting k-space trajectory is shown in Figure 3.1 (A) and the corresponding time courses of k-space, slew-rates and gradients in Figure 3.1 (B), (C) and (D), respectively. The different contributions of the two readout dimensions as well as their absolute value are presented in green, red and black, respectively.
Due to different properties of the 3 T Prisma and the 7 T Terra scanner, such as main magnetic field inhomogeneity, different spiral readout gradients are favorable for the respective system. Therefore, two spiral k-space trajectories with variable density were designed for phantom and in vivo studies, one for the Prisma and one for the Terra scanner. The respective input parameters of the MATLAB toolbox introduced above are summarized in Table 3.2. In order to mitigate off-resonance related artifacts, shorter readout durations are reasonable at 7 T, which e.g. can be realized by increasing the number of spiral interleaves N.

	Spiral trajectory design parameters					
	$S_{\max}$ [T/m/s]	$G_{\max}$ [mT/m]	T [µs]	N	F_{coeff} [cm]	res [mm]
3 T	149.5	36.0	1.0	37	{48.2, -32.1}	1.34
7 T	176.2	43.0	1.0	95	{40.9, -27.2}	1.14

Table 3.2: Input parameters of the MATLAB toolbox [98] to design spiral k-space trajectories for the 3 T Prisma and the 7 T Terra system, respectively: maximum slew-rate ($S_{\max}$), maximum gradient amplitude ($G_{\max}$), sampling increment (T), number of spiral interleaves (N), FOV coefficients ($F_{\mathrm{coeff}} = \{F_1,\ F_2\}$) and spatial resolution (res).

The resulting undersampled k-space trajectories applied for real-time imaging at the 3 T Prisma and the 7 T Terra system are summarized in Figure 3.2 (A) and (B), respectively. Each real-time frame was acquired with N_{RT} equidistantly distributed spiral interleaves, which ensured minimizing the largest gaps in the undersampled k-spaces. Figure 3.2 (A1) and (B1) show the frame-wise k-space trajectories for the cases of $N_{\mathrm{RT}} = 10$, and Figure 3.2 (A2) and (B2) show the readout gradient waveforms $g_{\mathrm{x}}(t)$ and $g_{\mathrm{y}}(t)$ of the first spiral interleave in green and red, respectively. The golden angle $GA = (2 \cdot \pi)/(\sqrt{5} + 1) \approx 111.25°$ was used to efficiently fill the k-space gaps between consecutive frames. This is realized by rotation of the 2D k-space by $\varphi = (2 \cdot GA)/N_{\mathrm{RT}}$

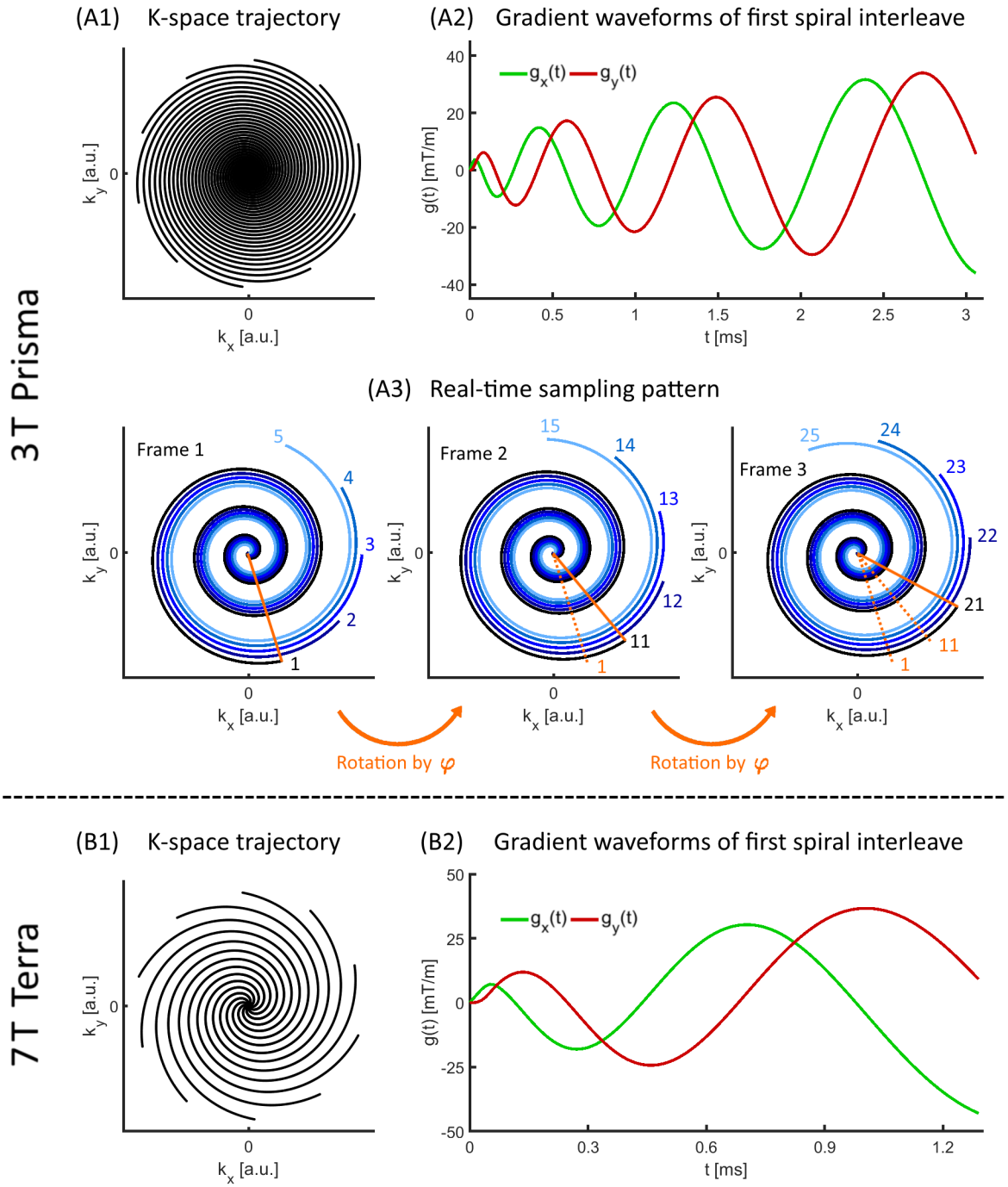

Figure 3.2: Spiral k-space trajectories used at the 3 T Prisma (A) and the 7 T Terra scanner (B). (A1, B1) show the k-space coverage of one real-time frame for the case of $N_{\mathrm{RT}} = 10$ equidistant spiral interleaves, and (A2, B2) show the gradient waveforms of the first interleave, respectively. (A3) outlines the total real-time sampling pattern applied at 3 T (with $N_{\mathrm{RT}} = 10$). The trajectory is rotated by $\varphi \approx 22.25°$ between the frames (orange). For clarity, only the first five interleaves are shown in each of the three consecutive frames (blue gradations).

from frame to frame. This procedure is illustrated in Figure 3.2 (A3) for the case of $N_{\mathrm{RT}} = 10$ ($\varphi \approx 22.25°$). For clarity, however, only the first five spiral interleaves of each k-space are shown ($1 \rightarrow 5$, $11 \rightarrow 15$ and $21 \rightarrow 25$). Note that this real-time sampling pattern fixes the temporal resolution of the acquired dynamic process to $\Delta t = N_{\mathrm{RT}} \cdot TR$. Spiral real-time imaging at 7 T was performed using $N_{\mathrm{RT}} = 10$ and $N_{\mathrm{RT}} = 20$, following the same approach as presented in Figure 3.2 (A3).

3.2.2 TWIRL k-space trajectories

The theory of the TWIRL k-space trajectory was explained in Section 2.3.2. An example, dubbed $\mathrm{TWIRL}_{\mathrm{orig}}$, is given in Figure 3.3 (A) and (B) to illustrate the four different stages. It corresponds to the parameters summarized in the first row of Table 3.3: maximum slew-rate (S_{max}), maximum gradient amplitude (G_{max}) and spatial resolution (*res*). r_m, p and ϑ_0 are the three parameters that additionally constrain the shape of the trajectory as defined by Equations 2.6-2.9 in Section 2.3.2.

	TWIRL trajectory design parameters					
	S_{max} [T/m/s]	G_{max} [mT/m]	*res* [mm]	r_m [µTs/m]	p	ϑ_0 [rad]
$\mathrm{TWIRL}_{\mathrm{orig}}$	60.0	12.0	1.39	8.4	0.40	0.085
$\mathrm{TWIRL}_{\mathrm{dip}}$	60.0	12.0	1.39	8.4	0.30	0.345

Table 3.3: Input parameters of an exemplarily designed original $\mathrm{TWIRL}_{\mathrm{orig}}$ and the modified $\mathrm{TWIRL}_{\mathrm{dip}}$ k-space trajectory, respectively: maximum slew-rate (S_{max}), maximum gradient amplitude (G_{max}) and spatial resolution (*res*); r_m, p and ϑ_0 additionally constrain the shape of the trajectory (see Equations 2.6-2.9 of Section 2.3.2).

Figure 3.3 (A) and (B) show the first three interleaves of a golden angle sampling pattern as well as the gradient waveforms of the first interleave with the four stages drawn in colors of green, orange, blue and red, respectively. Similarly, the trajectory chosen for CMR, dubbed $\mathrm{TWIRL}_{\mathrm{dip}}$, is presented in Figure 3.3 (C) and (D), which refers to the parameters given in the second row of Table 3.3. There, two parts of the trajectory were modified as compared to $\mathrm{TWIRL}_{\mathrm{orig}}$. Firstly, the time of the slice select rephaser was used to move faster through the k-space center. This was realized by an initial triangular gradient waveform of $g_{\mathrm{x}}(t)$ as shown in Figure 3.3 (D) (stage 0 with t_0, drawn in black). After t_0, data acquisition started with the regular stage 1,

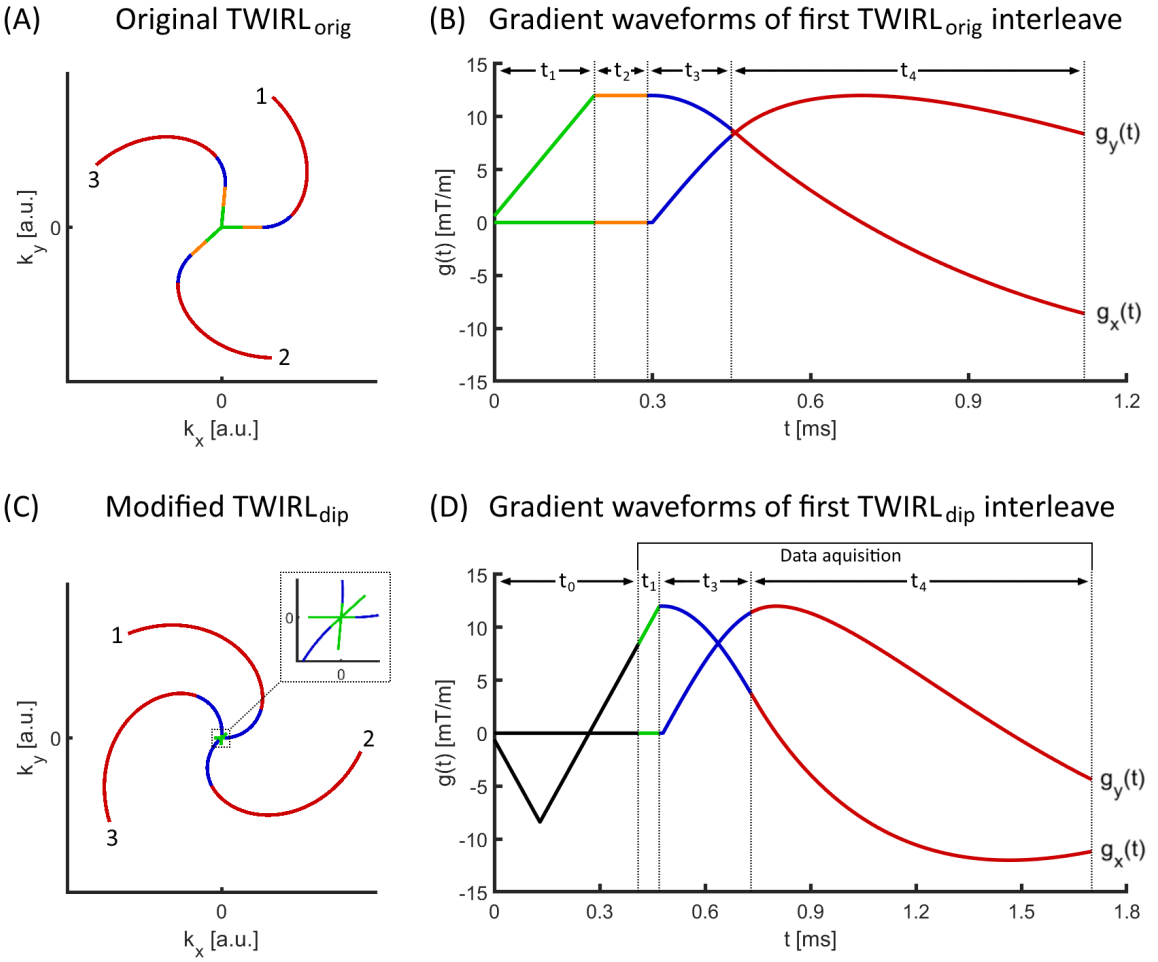

Figure 3.3: The first three interleaves in golden angle sampling of an original $\text{TWIRL}_{\text{orig}}$ as well as the modified $\text{TWIRL}_{\text{dip}}$ k-space trajectory are shown in (A) and (C), together with the corresponding gradient waveforms of the first interleave in (B) and (D), respectively. The four different stages of the TWIRL trajectory are drawn in green, orange, blue and red, respectively. In the modified $\text{TWIRL}_{\text{dip}}$ gradients, stage 2 (orange) was removed and a stage 0 (black) was implemented.

which is highlighted in Figure 3.3 (C) by the zoomed-in region of the k-space center as an inlay. This means that t_0 was chosen such that each interleave samples the k-space center in both directions. Secondly, stage 2 was omitted for the purpose of lengthening the k-space pathway up to k_{max}, which ultimately decreases the k-space voids between the interleaves (see p-values in Table 3.3, which refer to the fraction of TWIRL interleaves necessary for *Nyquist* sampling compared to radial sampling). This $\text{TWIRL}_{\text{dip}}$ trajectory was applied to gated CMR at the 7 T Terra system. Therefore, the readout gradients were designed with a relatively short duration in order to mitigate off-resonance related artifacts, similar to the spiral trajectory design for

7 T (compare to Figure 3.2 B2). For gated imaging a golden angle sampling pattern with an angle increment of $\theta = 2 \cdot GA \approx 222.5°$ was utilized (with the golden angle $GA = (2 \cdot \pi)/(\sqrt{5}+1) \approx 111.25°$).

3.3 Trajectory correction using the GSTF

After the introduction of the GSTF measurements and the design of the desired non-Cartesian readout gradient waveforms, the applied trajectory correction technique will be explained. The GSTF characterizes the frequency dependent transfer behavior of the MR scanner's gradient system. This information can be utilized in two different approaches, which both result in matching the sampled k-space locations with the trajectory used for image reconstruction. The first option is to exploit the GSTF in the reconstruction step, in which the k-space trajectory is calculated. In this case, the GSTF correction is done after the data was acquired, which is why it is referred to as *post-correction* in the following. In the second approach, called *pre-emphasis*, the inverse of the GSTF is used to compensate gradient errors prior to playing out the gradient waveforms. In the first part of this project, the goal was to implement a GSTF pre-emphasis for a two-dimensional (2D) spoiled GRE sequence, which automatically corrects arbitrary non-Cartesian input gradients for double-oblique MRI.
For this, the three inverted GSTF self-terms ($\mathrm{GSTF}_{k,k}$, with $k \in \{x, y, z\}$) and the two previously created non-Cartesian readout gradients $g_1(t)$ and $g_2(t)$ were written into the pulse sequence code. The orientation of an arbitrary slice was encoded within a rotation matrix R_1, which projected $g_1(t)$ and $g_2(t)$ on the physical x-, y- and z-axis. A second rotation matrix R_2 carried the spatial information of the current readout step, which served the purpose of filling the 2D k-space. Ultimately, the respective spatial contributions $g_k(t)$ resulted from:

$$\begin{pmatrix} g_x(t) \\ g_y(t) \\ g_z(t) \end{pmatrix} = R_1 \cdot R_2 \cdot \begin{pmatrix} g_1(t) \\ g_2(t) \\ 0 \end{pmatrix} \tag{3.3}$$

Subsequently, the contributions $g_k(t)$ were *Fourier*-transformed to the temporal frequency domain and multiplied with the inverse GSTF of the corresponding dimension.

Inverse *Fourier* transform back to time domain yielded the pre-emphasized gradient waveforms $g_k^{\mathrm{pre}}(t)$. This way, the originally intended waveforms were played out by the dynamic gradient system and image reconstruction could be performed with the nominal k-space trajectory. In post-correction, the contributions $g_k(t)$ were played out without further processing, and the correct k-space trajectory resulted from convolution with the original GSTFs during image reconstruction ($g_k^{\mathrm{post}}(t)$). Both approaches are summarized in Equation 3.4.

$$\begin{aligned} &\text{Pre-emphasis:} && g_k^{\mathrm{pre}}(t) \;= \mathcal{F}^{-1}\{\mathcal{F}\left[g_k(t)\right] \cdot \mathrm{GSTF}_{k,k}^{-1}(f)\} \\ &\text{Post-correction:} && g_k^{\mathrm{post}}(t) = \mathcal{F}^{-1}\{\mathcal{F}\left[g_k(t)\right] \cdot \mathrm{GSTF}_{k,k}(f)\}. \end{aligned} \tag{3.4}$$

Note that inversion of the GSTF magnitude was only performed for the frequency range of interest, i.e. $<$ 12.2 kHz. This cutoff frequency was chosen in accordance with the frequency spectrum of the non-Cartesian readout gradients. Curve fitting of the original GSTF magnitude served as decaying function for frequencies larger than 12.2 kHz. Without this cutoff, inversion would lead to large gain factors at high frequencies. In addition to trajectory correction using the GSTF, the artifact power in the resulting images was evaluated using global delays only and the performances of both were compared to each other.

3.4 Phantom measurements

In addition to the GSTF measurements presented in Section 3.1, further measurements were performed using either a homogeneous, spherical phantom or a phantom with structures of different sizes. The purpose of all phantom measurements summarized in this section was the initial validation of the applied trajectory correction methods before they were transferred to in vivo imaging. A 16-channel head coil array was used for phantom measurements performed at the 3 T Prisma system and a single-channel tune-up coil for those at the 7 T Terra system.

One way to demonstrate the success of the proposed trajectory correction method using the GSTF is to measure the actual output of a pre-emphasized gradient waveform and compare it to the originally intended, theoretical waveform. For this measurement, a 1D phase encoder followed by the particular gradient waveform of interest was played out on one gradient axis in one slice in a spherical phantom. FFT along

the phase encoding dimension yielded the spatially encoded signal evolution of each readout, i.e. the phase encoder replaced the need of measuring multiple slices. Subsequently, the signal's phase of each readout was unwrapped. The phase values as a function of phase encoding steps exhibited a linear dependency for each readout point. Linear fits were created and their slopes yielded the respective k-space values. Differentiation and normalization by including the dwell time and the voxel size resulted in the correct gradient output. In order to increase *SNR*, the measurement was repeated 50 times.

Secondly, phantom measurements were done to investigate the performance of the automatic GSTF pre-emphasis. For this, data in transversal, coronal as well as in double-oblique slice orientations were acquired with both, the nominal and the pre-emphasized gradient waveforms. The corresponding imaging parameters of the measurements performed with the spiral k-space trajectories presented in Section 3.2.1 are summarized in Table 3.4: echo time (TE), repetition time (TR), dwell time (DT), number of spiral interleaves (N_{int}), number of sampling points per spiral interleave (N_{SP}), readout duration (RoD), flip angle (FA) and slice thickness (ST). An exemplary spoiled GRE pulse sequence diagram using the spiral readout gradients presented in Figure 3.2 (A2) is depicted in Figure 3.4. Here, the example of a transversal slice orientation is shown, which means that the slice selective gradient and the spoiler are played out on the z-axis and the two spiral readout gradients on the x- and y-axis, respectively.

	Spiral phantom and in vivo imaging parameters							
	TE [ms]	TR [ms]	DT [µs]	N_{int}	N_{SP}	RoD [ms]	FA [°]	ST [mm]
3 T	0.84	4.96	2.20	704	1408	3.10	15	8.0
7 T	0.84	3.20	2.50	256	512	1.30	25	6.0

Table 3.4: Imaging parameters of the phantom measurements performed with the spiral k-space trajectories presented in Section 3.2.1: echo time (TE), repetition time (TR), dwell time (DT), number of spiral interleaves (N_{int}), number of sampling points per spiral interleave (N_{SP}), readout duration (RoD), flip angle (FA) and slice thickness (ST).

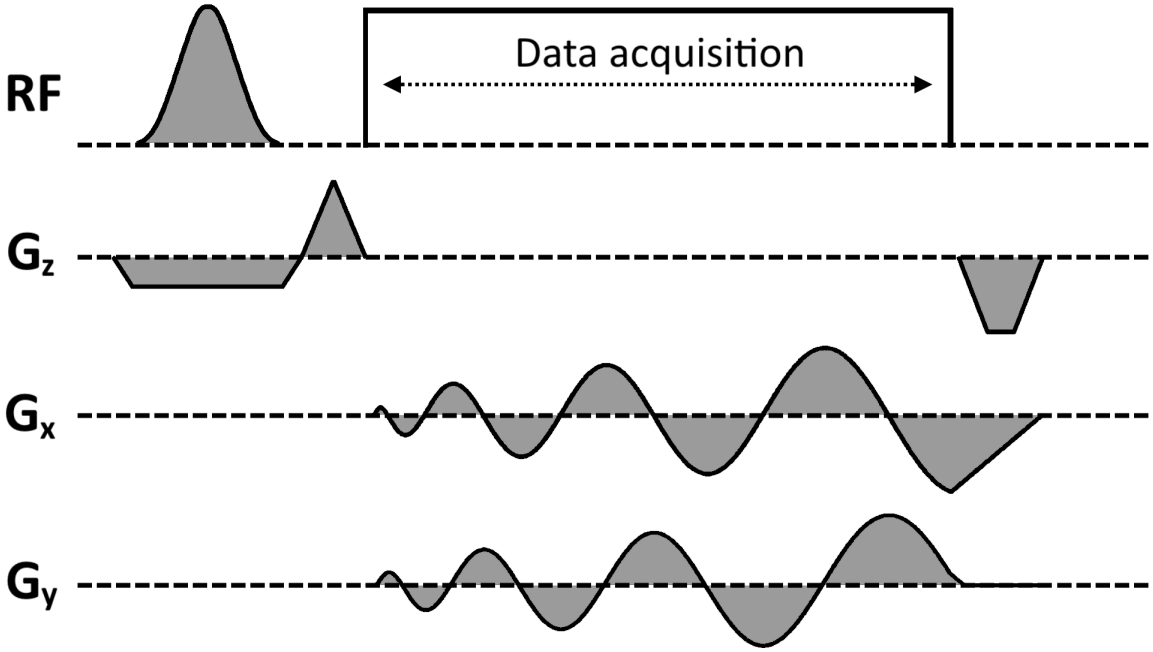

Figure 3.4: Exemplary pulse sequence diagram applying the spiral readout gradients presented in Figure 3.2 (A2) for a transversal slice orientation as used in both, phantom and in vivo experiments.

3.5 In vivo measurements

3.5.1 3 T Prisma scanner

All in vivo measurements performed at the 3 T Prisma scanner were approved by the local ethics committee and written informed consent was obtained from each participant. Cardiac imaging was done with an 18-channel body coil array together with a 16-channel spine coil array. A vendor-provided cardiac shim was applied for B_0-shimming of the examined volumes. The conducted study compared spiral real-time CMR with the gold standard of conventional Cartesian CMR using an ECG-gated GRE sequence. Throughout the thesis, the developed spiral imaging framework will be referred to as CRISPI (Cardiac Real-time Imaging using a SPIral k-space trajectory). The spiral measurements were performed with the sampling pattern described in Figure 3.2 (A3) and the imaging parameters coincide with those of the phantom measurements presented in the first row of Table 3.4. In general, the same spiral GRE sequence was used for phantom and in vivo imaging, following the exemplary pulse

sequence diagram shown in Figure 3.4. $N_{\mathrm{RT}} = 10$ equidistant interleaves formed one real-time frame resulting in a temporal resolution of $\Delta t = 49.6\,\mathrm{ms}$. This k-space coverage led to a minimum sampling density at $k_{\max}$ that corresponded to a minimum field of view of $FOV_{\min} = 44\,\mathrm{mm}$. In total, the following protocol was applied to 7 healthy participants and 2 patients suffering from cardiac disease:

1) Spiral acquisitions of a midventricular short-axis (SAX) slice with and without pre-emphasis. Both measurements were performed in breath hold with a duration of 3.5 seconds, respectively, with the aim of evaluating the in vivo performance of the GSTF trajectory correction.

2) Spiral acquisitions of the whole heart in SAX orientation covering a stack of $10 - 14$ slices from base to apex, depending on the size of the heart. Here, the spiral pre-emphasis was applied in all cases, and the whole stack was acquired in breath hold (3.5 seconds each slice) as well as in free breathing (total imaging time: $35 - 49$ seconds). Therefore, irregularities that refer only to breathing motion could be traced.

3) Cartesian acquisitions of the same SAX stack using an ECG-gated spoiled GRE sequence in breath hold as a reference technique. The corresponding imaging parameters that were adjusted individually dependent on the subject size are summarized in Table 3.5: echo time (TE), repetition time (TR), field of view

In vivo imaging parameters of the Cartesian reference			
$TE\,[\mathrm{ms}]$	$2.29 - 2.41$	IM	208×163
$TR\,[\mathrm{ms}]$	$4.57 - 4.80$	$RoD\,[\mathrm{ms}]$	1.41
$FOV\,[\mathrm{mm}^2]$	$(280 - 360) \times (229 - 294)$	$FA\,[^\circ]$	15
$res\,[\mathrm{mm}^2]$	$(1.35 - 1.73) \times (1.41 - 1.80)$	ST [mm]	8.0
$\Delta\,t\,[\mathrm{ms}]$	$27.42 - 50.82$	T-GRAPPA	2
$DT\,[\mu\mathrm{s}]$	3.4		

Table 3.5: In vivo imaging parameters of the ECG-gated Cartesian GRE sequence used as a reference technique in the CRISPI study: echo time (TE), repetition time (TR), field of view (FOV), spatial resolution (res), temporal resolution ($\Delta\,t$), dwell time (DT), image matrix (IM), readout duration (RoD), flip angle (FA), slice thickness (ST) and the T-GRAPPA acceleration factor.

(FOV), spatial resolution (res), temporal resolution (Δt), dwell time (DT), image matrix (IM), readout duration (RoD), flip angle (FA), slice thickness (ST) and the T-GRAPPA acceleration factor.

3.5.2 7 T Terra scanner

Human in vivo measurements performed at the 7 T Terra scanner were approved by the local ethics committee and written informed consent was obtained from the healthy participant. The acquisitions were done using a 16-channel body coil array (MRI.TOOLS GmbH, Berlin, Germany). A vendor-provided brain shim was applied for B_0-shimming of the examined volumes.
One healthy participant was measured with the $\text{TWIRL}_{\text{dip}}$ k-space trajectory as presented in Figure 3.3 (C) and self-gated CMR was performed using the golden angle sampling pattern. One midventricular SAX slice was acquired during a breath hold of 9.2 seconds. Similar to the 3 T experiments, the measurement was done with and without GSTF pre-emphasis. The following imaging parameters were used: $TE = 0.9\,\text{ms}$, $TR = 3.0\,\text{ms}$, $DT = 2.5\,\mu\text{s}$, number of TWIRL interleaves $N_{\text{int}} = 3072$, number of sampling points per TWIRL interleave $N_{\text{SP}} = 512$, $RoD = 1.28\,\text{ms}$, $FA = 22\,^\circ$ and $ST = 6.0\,\text{mm}$.

In addition, in vivo experiments were done in a pig, which were covered by an animal experiment application (reference number: 55.2.2-2532.2-1134-16). The pig was anesthetized with isoflurane and fentanyl analgesia, and artificial ventilation was controlled by a trained veterinarian using an MR-compatible ventilator (Draeger, Germany). Additionally, the veterinarian supervised heart rate, ventilation parameters, oxygen saturation as well as rectal temperature. Here, the acquisitions were done with a 16-channel coil array built in-house by *Ibrahim Elabyad* [99–101]. Again, a vendor-provided brain shim was adjusted to the whole cardiac volume.
Cardiac real-time imaging in free breathing was performed in a midventricular SAX slice using the spiral gradients presented in Figure 3.2 (B2). The number of spiral interleaves in each real-time frame was set to $N_{\text{RT}} = 10$ and $N_{\text{RT}} = 20$. This yielded temporal resolutions of $\Delta t = 32\,\text{ms}$ and $\Delta t = 64\,\text{ms}$, and the minimum sampling densities at k_{max} corresponded to minimum field of views of $FOV_{\text{min}} = 14\,\text{mm}$ and $FOV_{\text{min}} = 29\,\text{mm}$, respectively. Spiral in vivo imaging parameters matched those of the phantom measurements as summarized in the second row of Table 3.4. However,

the number of spiral interleaves was multiplied by a factor of 4 to $N_{\text{int}} = 1024$ in order to increase the measurement time. Again, the measurements were performed with and without GSTF pre-emphasis.

3.6 Image reconstruction of non-Cartesian data

In this work, all non-Cartesian measurements were reconstructed offline using MATLAB. In a first step, the k-space data were transferred to a Cartesian grid (see Section 2.4). For measurements performed with a single channel coil, convolution gridding was used. In contrast, data acquired with a multi-coil receive element were gridded using the GROG formalism. The non-Cartesian k-space source points were determined using the nominal readout gradients as implemented in the pulse sequence code. Here, no additional low-resolution Cartesian ACS calibration scan was performed. Instead, a fully sampled Cartesian k-space was obtained by applying convolution gridding to a temporally averaged dataset. With this, the GRAPPA operators were calibrated. Subsequently, these operators were used to shift the non-Cartesian sampling points towards their nearest Cartesian grid position. Depending on static phantom or dynamic in vivo data, the non-Cartesian source points belong to a fully sampled or an undersampled k-space.
The low rank plus sparse CS model of Otazo et al. [60] (see Equation 2.11 in Section 2.5) was employed to fill missing voids in undersampled k-spaces. In all cases, FFT to the temporal frequency domain was applied as the additional sparsifying transform T. The number of iterations N_{it} as well as the two regularization parameters λ_L and λ_S were chosen empirically and read: $N_{\text{it}} = 70$, $\lambda_L = 0.01$ with λ_S set to 5 % of the maximum value in the sparse domain. These parameters were kept constant for all reconstructions of undersampled cardiac data at 3 T and 7 T. A maximum acceleration factor R_{max} of the applied undersampled acquisitions can be calculated by the ratio of the maximum void in the undersampled k-space to the distance between two neighboring k-space positions of the underlying Cartesian grid chosen for the reconstruction framework. For the spiral real-time acquisitions with $N_{\text{RT}} = 10$ at 3 T, R_{max} yielded a value of $R_{\text{max}} = 15.6$. In the cases of spiral real-time imaging at 7 T using $N_{\text{RT}} = 10$ and $N_{\text{RT}} = 20$, R_{max} was calculated to $R_{\text{max}} = 30.4$ and $R_{\text{max}} = 15.2$, respectively.

3.7 Quantification of cardiac functional parameters

The study introduced in Subsection 3.5.1 compared spiral real-time CMR (CRISPI) in breath hold and free breathing with the gold standard of conventional Cartesian cine imaging using ECG-gating in breath hold at 3 T. To comprehensively characterize the different techniques, quantitative cardiac functional parameters must be evaluated. Therefore, end-diastolic volume (EDV), end-systolic volume (ESV), stroke volume (SV) and ejection fraction (EF) of the left ventricle were determined for the three SAX stacks for all participants and patients. The data was evaluated by a trained operator (4 years of experience in CMR) following the approach presented in Section 2.7 (see e.g. Equation 2.13). The assessment of the endocardial border was done using a dedicated cardiovascular imaging software (Circle Cardiovascular Imaging Inc., Calgary, Canada). To test for significant differences between the quantitative parameters of the different methods, a Wilcoxon signed-rank test was additionally conducted.

4 Results

4.1 Phantom and in vivo results at 3 T

Many results presented in this section were published as a journal article in *Magnetic Resonance in Medicine* by the author of this dissertation and colleagues (see Ref. [102]). Following the signed "Attribution-NonCommercial 4.0 International" license agreement *CC BY-NC 4.0*, the author is allowed to include the published figures from that article into this dissertation. In these cases, the article will be cited at the end of each corresponding figure caption, respectively, together with an indication if changes were made.

4.1.1 The GSTF

The magnitude and phase of the determined GSTF of the 3 T Prisma scanner are depicted in Figure 4.1 (A) and (B), and the self-terms of the x-, y- and z-axis are drawn in colors of red, blue and green, respectively. The course of the magnitude represents typical low-pass behavior as the transmission decreases with increasing frequency. In general, the transfer characteristics of the x- and y-axis appear to be quite similar. In contrast, the GSTF self-term of the z-axis deviates from those of the two other axes. Furthermore, it is remarkable that the GSTF magnitude of the z-axis is greater than that of the x- and y-axis for all frequencies, respectively. It even exceeds the transmission value of 1 in the low frequency range. At certain input frequencies, the hardware components of the MR scanner resonate, which presents itself as small fluctuations in the shape of the GSTF self-terms. Exemplarily, resonance frequencies at around 1.7 kHz and 4.0 kHz are emphasized in the inlay of Figure 4.1 (A). The shape of the GSTF phase is approximately linear in the case of the x- and y-axis, however,

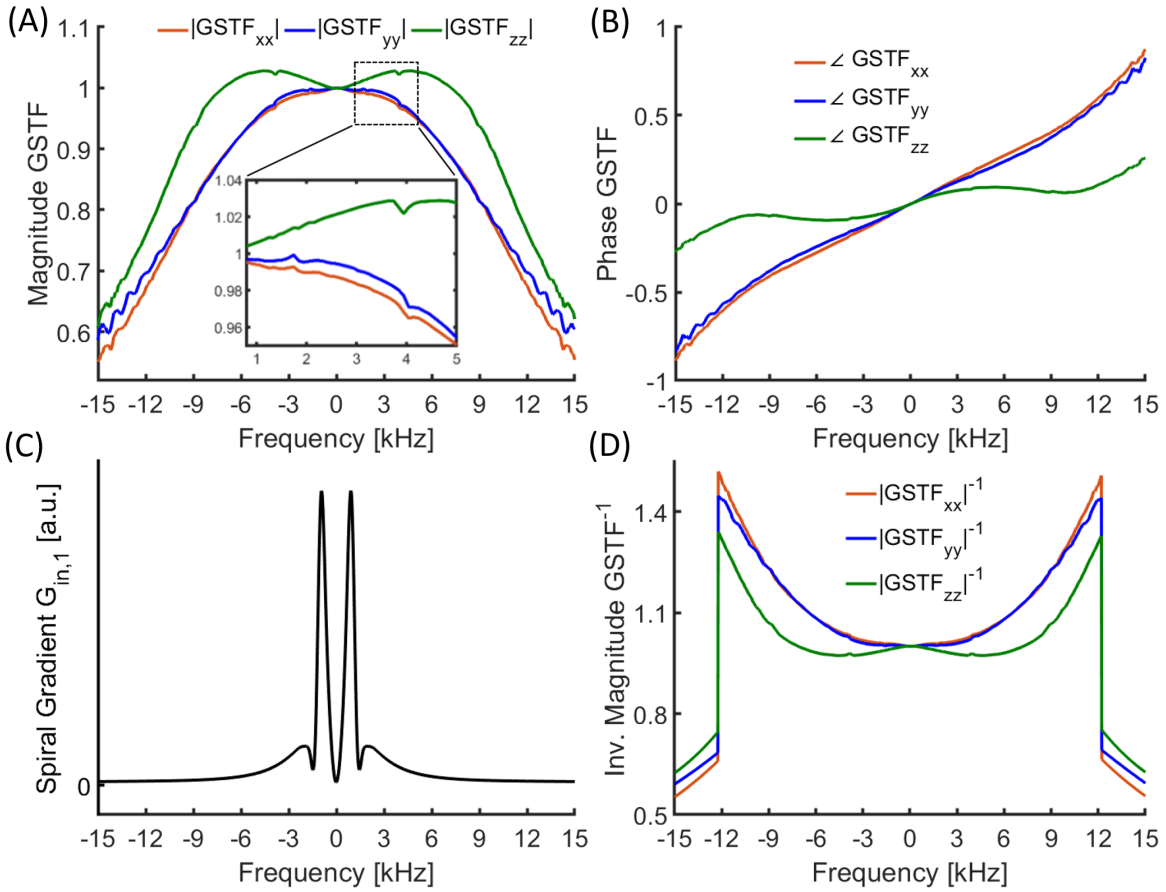

Figure 4.1: Magnitude (A) and phase (B) of the measured Gradient System Transfer Function (GSTF) at 3 T. The self-terms of the three physical dimensions x, y and z are depicted in red, blue and green, respectively, together with scanner-specific resonances (inlay of A). (C) and (D) show the magnitude of one of the spiral readout gradients in the frequency domain and the inverted GSTF magnitude applied to the automatic pre-emphasis, respectively. (from Eirich et al. [102], modified)

it is rather undulating in the case of the z-axis. The frequency spectrum of one of the applied spiral readout gradients (for comparison see Figure 3.2 A2) is shown in Figure 4.1 (C). In this example, the main contributions of the spiral waveform lie in the frequency range of less than 5 kHz. Knowing the shape of the spiral frequency spectrum is a key prerequisite for a successful pre-emphasis as a cutoff frequency should be implemented when inverting the GSTF magnitude. Here, the cutoff frequency was set to 12.2 kHz, which ensures to invert also the small contributions in the frequency range higher than 5 kHz. The resulting inverse GSTF magnitude, following the description of Section 3.3, is presented in Figure 4.1 (D).

4.1.2 Phantom results

The comparison of measured gradient output waveforms with the input waveforms is depicted for both spiral readout gradients in Figure 4.2 (A1) and (B1), respectively. To highlight the differences of the gradient waveforms, a zoomed-in image of the area with maximum amplitude is presented in both cases (see Figure 4.2 A2 and B2). The pre-emphasized, nominal as well as the measured waveforms with and without pre-emphasis are shown in colors of blue, black, green and orange, respectively. The intended gradient waveforms were transferred by the scanner (green curves match dashed black curves) when playing out the waveforms that were generated by the automatic GSTF pre-emphasis (blue curves). However, if the scanner applied the waveforms without trajectory correction (dashed black curves), the true output deviated from the actually intended waveforms (orange curves).

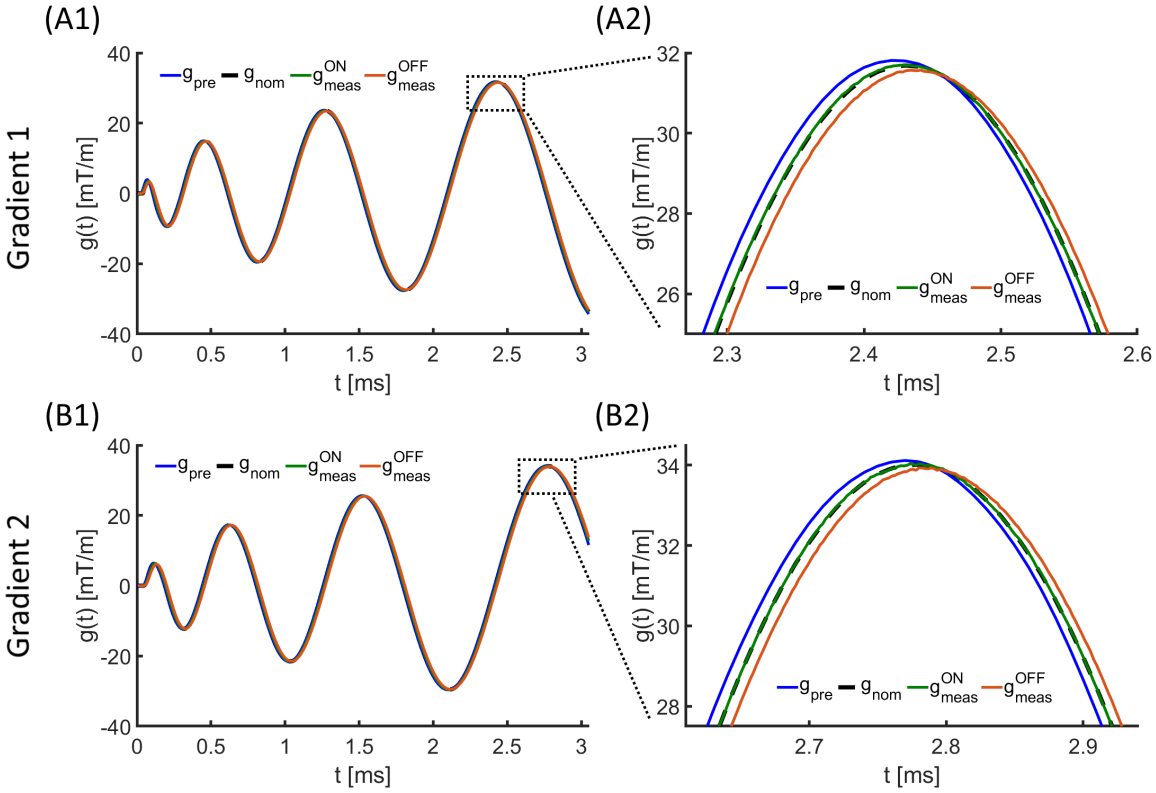

Figure 4.2: (A1) and (B1) compare the pre-emphasized, nominal and measured gradient waveforms (with and without pre-emphasis) for both spiral readout gradients in blue, black, green and orange, respectively. (A2) and (B2) show zoomed-in views of the regions with maximum amplitude. (from Eirich et al. [102], modified)

Figure 4.3 demonstrates the performance of the GSTF pre-emphasis on a structural phantom for transversal (A) as well as a double-oblique slice orientation (B). In favor of a better comparison, a similar slice of the phantom was chosen for both orientations. Hence the phantom was rotated in the setup of the double-oblique experiment, and the perpendicular slice orientation yielded the images shown in Figure 4.3 (B). Furthermore, the nominal k-space trajectory was used for image reconstruction in all cases. The resulting image quality when playing out the uncorrected gradient waveforms is shown in Figure 4.3 (A1) and (B1), respectively. Typical artifacts that correspond to k-space sampling errors, such as ghosting artifacts or signal pile-ups and voids, are present in both images. They could be mitigated by applying the pre-emphasized gradient waveforms as can be seen in Figure 4.3 (A2) and (B2), respectively. Line profiles that correspond to the orange line were added in Figure 4.3 to support the analysis. As a result, corrupted signal intensities inside phantom structures together with signal dropouts at phantom edges are present in Figure 4.3 (A1) and (B1), which could be reduced in Figure 4.3 (A2) and (B2).

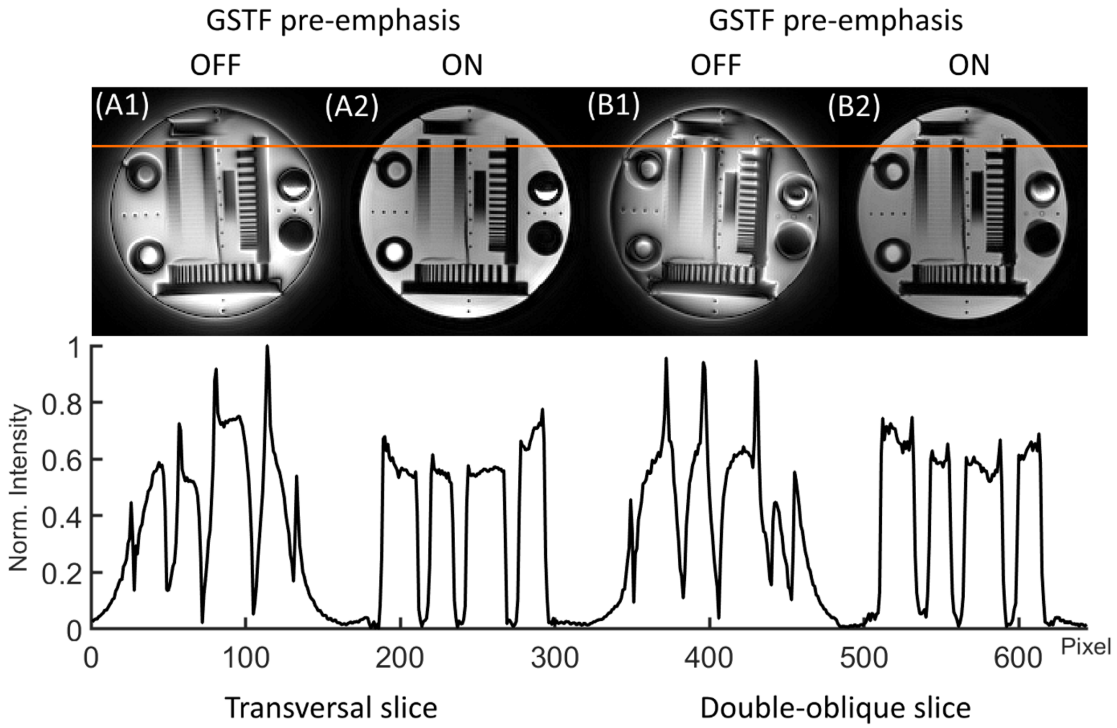

Figure 4.3: Transversal (A) and double-oblique (B) slice orientation of a structural phantom, measured without (A1, B1) and with (A2, B2) GSTF pre-emphasis, respectively. The line profiles correspond to the orange line in the phantom images. (from Eirich et al. [102])

In addition, the structural phantom was used to compare the artifact power of k-space trajectory correction using the comprehensive GSTF pre-emphasis with using global delays only. This comparison is summarized in Figure 4.4, for the case of the double-oblique slice measurement. The acquisitions without and with pre-emphasis, reconstructed with the nominal k-space trajectory, are shown in Figure 4.4 (A) and (D), respectively. To include efficient time delays into image reconstruction, the nominal trajectory was shifted in time by values that minimize the delay effect at a certain gradient axis, i.e. time delays of 7.70 µs and 11.3 µs for the x- and z-axis, respectively. In both cases, the delays were chosen to be identical for all three dimensions. The corresponding phantom images are presented in Figure 4.4 (B) and (C), respectively. They show that time delays also improve the overall image quality. However, the high image quality obtained by the GSTF pre-emphasis could not be achieved, because image artifacts were still present (emphasized by orange arrows).

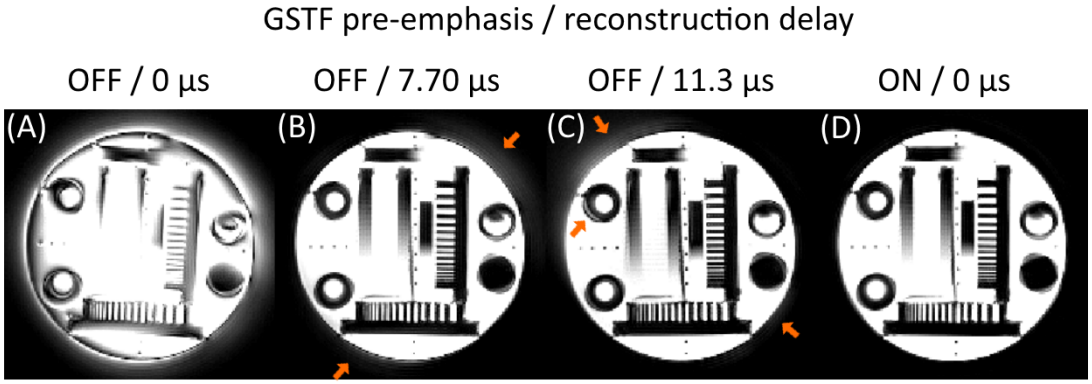

Figure 4.4: Comparison of the different trajectory correction techniques applied to a structural phantom in double-oblique slice orientation. (A) and (D) show the measurements without and with GSTF pre-emphasis, reconstructed with the nominal trajectory. The images in (B) and (C) correspond to the measurement without pre-emphasis, but were reconstructed using optimized time delays of 7.70 µs and 11.3 µs, respectively. The orange arrows emphasize remaining artifacts when using the delay compensation. (from Eirich et al. [102])

4.1.3 CMR in healthy participants

In this subsection, the spiral in vivo results are summarized that were gathered by performing the CMR measurements in healthy volunteers using the CRISPI sequence. Firstly, the impact of the GSTF pre-emphasis on in vivo imaging is demonstrated (Figure 4.5 A). As an example, a midventricular SAX slice of one healthy volunteer without and with pre-emphasis is shown in Figure 4.5 (A1) and (A2), respectively. To draw the attention to trajectory errors, a fully sampled and temporally averaged dataset was used (704 spiral interleaves), which was acquired in breath hold. Image reconstruction was performed using the nominal k-space trajectory. When comparing to the phantom results of Figure 4.3, similar shading artifacts appear in the CMR reconstructions when using no trajectory correction (Figure 4.5 A1). Again, the applied pre-emphasis mitigates those artifacts and greatly improves the image quality (Figure 4.5 A2). In addition, the same dataset was chosen to evaluate the influence of the compressed sensing (CS) reconstruction pipeline. For this, an exemplary end-diastolic real-time frame reconstructed without and with CS is depicted in Figure 4.5 (B1) and (B2), respectively. Due to the undersampled 2D k-spaces that were chosen for the real-time frames, incoherent aliasing compromises the image quality (Figure 4.5 B1).

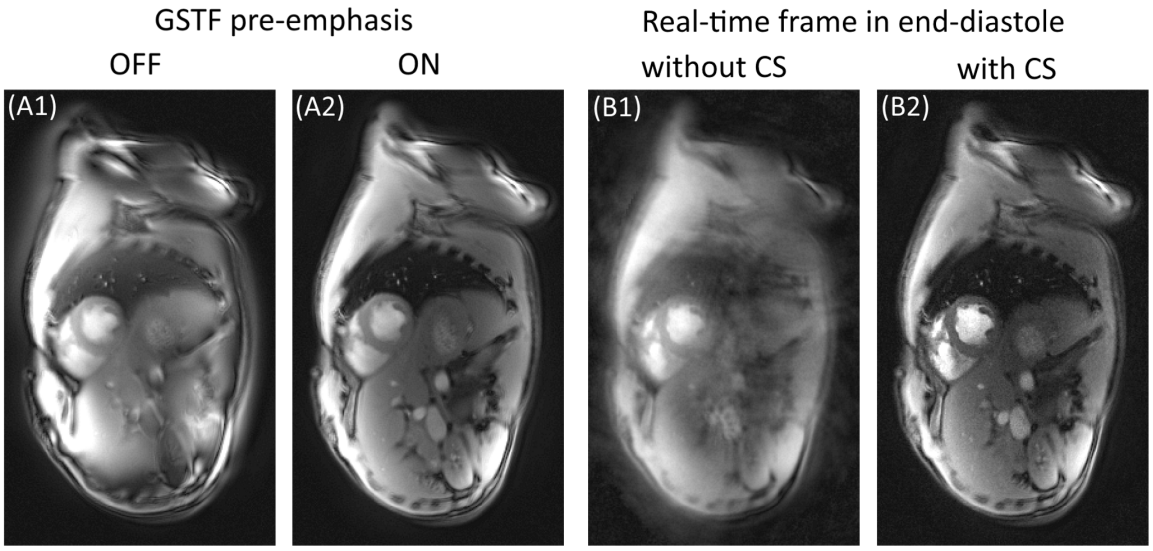

Figure 4.5: Midventricular SAX slice of a healthy volunteer, measured in breath hold without (A1) and with (A2) GSTF pre-emphasis, and reconstructed with 704 temporally averaged spiral interleaves. (B1) and (B2) show a real-time frame in end-diastole, which was reconstructed without (B1) and with (B2) compressed sensing (CS), respectively. (from Eirich et al. [102])

However, applying the low-rank plus sparse CS model successfully filled the missing k-space voids, which ultimately removes the aliasing (Figure 4.5 B2).
To verify that the automatic pre-emphasis works for arbitrary slice orientations, end-diastolic real-time frames acquired in 4-Chamber and SAX view are shown in Figure 4.6 (A) and (B), respectively. Again, measurements without and with GSTF pre-emphasis were performed and reconstructed with the nominal k-space trajectory. This yielded the images shown in Figure 4.6 (A1, B1) and (A2, B2), respectively. Addi-

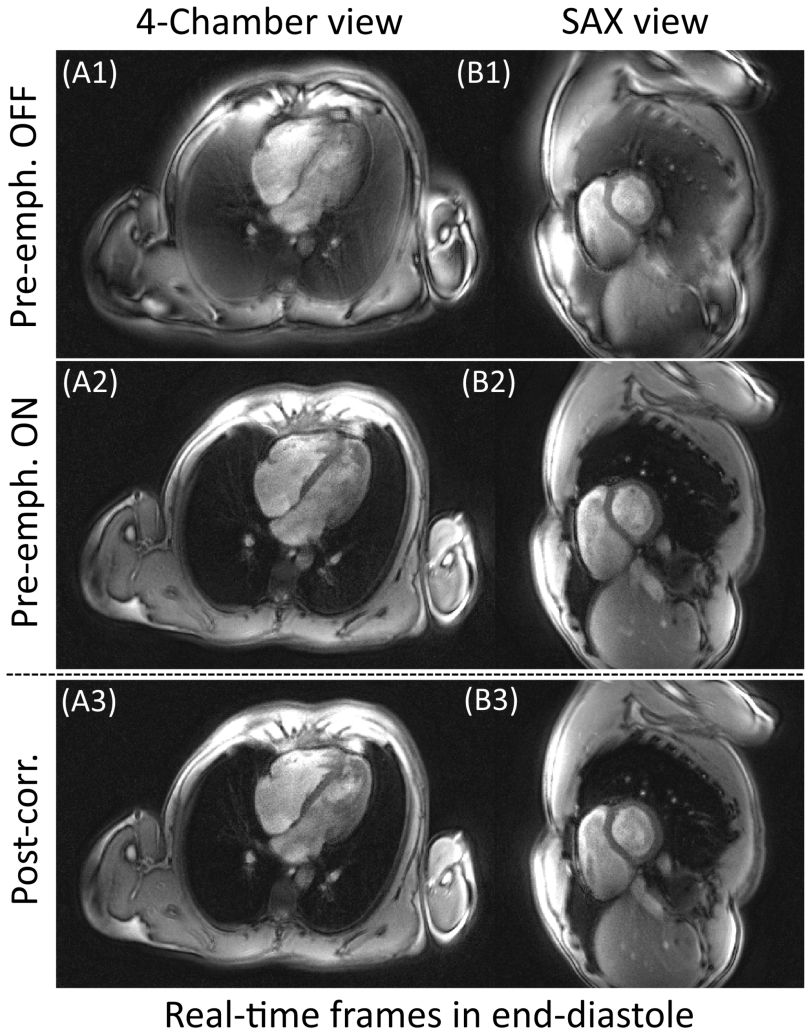

Figure 4.6: End-diastolic real-time frames in 4-Chamber (A) and SAX view (B) of a healthy volunteer, acquired in free breathing. (A1, B1) and (A2, B2) correspond to the measurements without and with GSTF pre-emphasis, both reconstructed with the nominal trajectory. (A3) and (B3) are the reconstructed images that refer to using the GSTF in post-processing. (from Eirich et al. [102])

tionally, applying the GSTF in post-processing during image reconstruction resulted in the images presented in Figure 4.6 (A3) and (B3). Image artifacts due to k-space misregistrations are visible using no trajectory correction, which could be improved by using both the pre-emphasis as well as the post-correction. Both trajectory correction methods resulted in high-quality 4-Chamber images as well as SAX images. However, note that the images of Figure 4.6 (A2, B2) and (A3, B3) not necessarily show the identical slice, because they belong to two different measurements performed in free breathing. To present the time dynamics of the CRISPI results, 20 real-time frames that correspond to one R-R interval are depicted in Figure 4.7. They refer to a measurement in midventicular SAX orientation of a healthy volunteer, which was performed in free breathing. The image order from top left towards bottom right shows the frames between end-diastole 1 and end-diastole 2. The end-systolic cardiac phase is emphasized by a dashed blue box in frame 10. The green and orange line marks the diaphragm-lung interface from end-diastole 1 and end-diastole 2, respectively, which indicates the present breathing motion.

Figure 4.7: Real-time CRISPI image series of a midventricular SAX slice, acquired in a healthy volunteer in free breathing. One R-R interval is represented by 20 time frames, from end-diastole 1 (top left) to end-diastole 2 (bottom right). The end-systolic frame is highlighted with a dashed blue box and the green and orange lines mark the diaphragm-lung interface due to breathing motion. (from Eirich et al. [102])

Figure 4.8 finally compares the developed spiral real-time CRISPI sequence with the reference technique of conventional ECG-gated cine imaging using Cartesian readouts. The gated reference is summarized in the left column, and the CRISPI results in breath hold (BH) as well as in free breathing (FB) in the middle and right column, respectively. End-systole and end-diastole of three exemplary SAX slices are presented for all three cases. Similar image quality could be observed using the different sequences. The CRISPI images reveal some blurring artifacts caused by off-resonance effects, especially in parts that contain fat tissue. However, they do not impair the image quality in the region of the heart, to which the shim was adjusted. In addition, x-t diagrams were included in Figure 4.8 to support the analysis. They correspond to the orange line drawn in the respective diastole frame of the second slice. A time interval is shown, in which twice the R-R interval of the gated reference matches the time of 45 real-time frames of the CRISPI sequence. Figure 4.7 and particularly the x-t diagrams

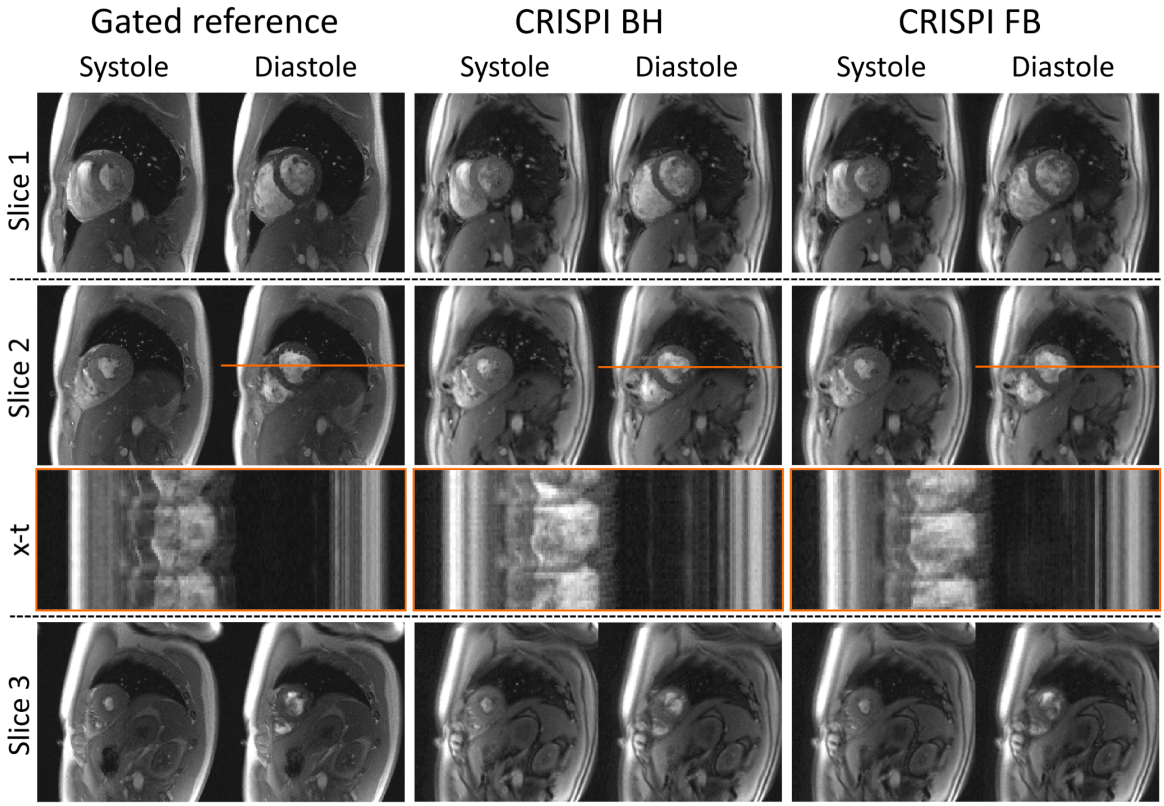

Figure 4.8: Three exemplary SAX slices of a healthy volunteer, acquired with the gated reference (left column) and the CRISPI sequence in breath hold (BH, middle column) and free breathing (FB, right column). End-systolic and end-diastolic frames are shown, respectively, with a x-t diagram refering to the orange line of slice 2. (from Eirich et al. [102])

shown in Figure 4.8 reveal that the temporal resolution of < 50 ms of the prepared CRSPI sequence is sufficient to successfully preserve the cardiac dynamics. At most, the blood-myocardium contrast is a little higher in the case of the gated reference.

4.1.4 CMR in patients

In this subsection, the resulting images of two patients examined by the different techniques are presented. Following the structure of Figure 4.8, the gated reference and the CRISPI images in breath hold (BH) as well as free breathing (FB) are summarized in the left, middle and right column of Figure 4.9. Both patients (Figure 4.9 A and B) suffered from heart failure with reduced ejection fraction, but one of them also exhib-

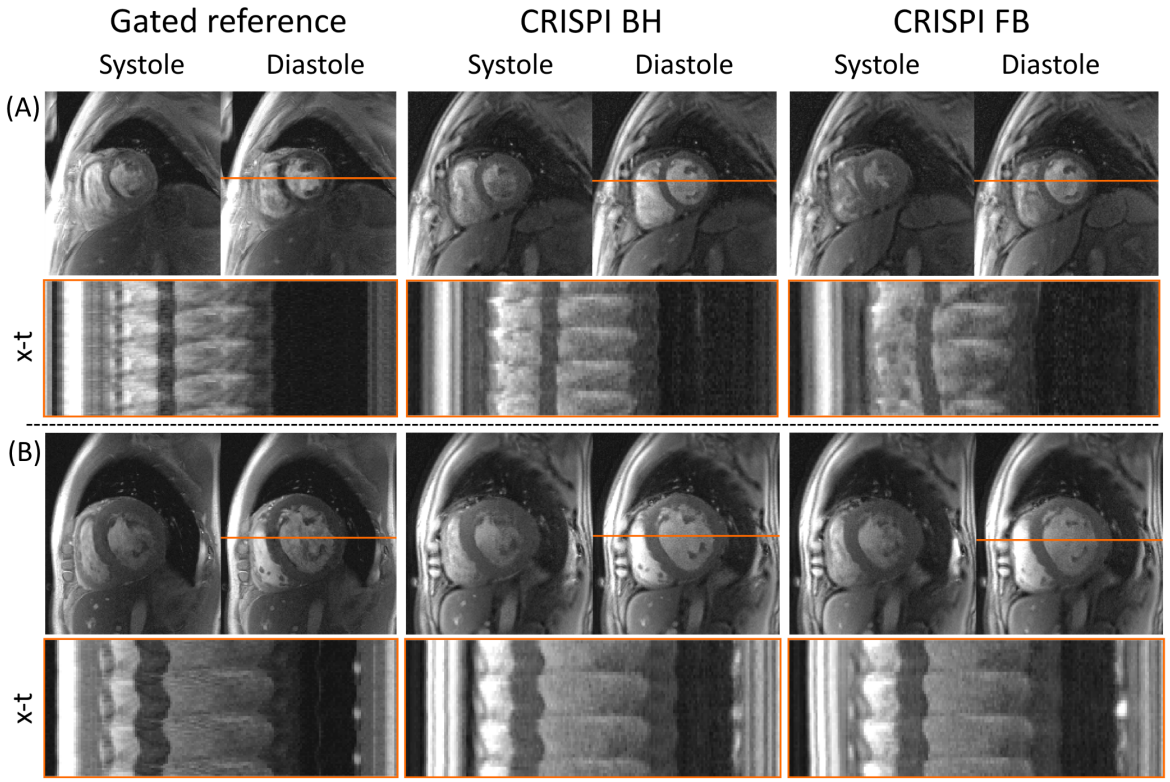

Figure 4.9: Comparison of the gated reference (left column) with the CRISPI images in breath hold (BH, middle column) and free breathing (FB, right column), acquired in two patients with cardiac disease (A and B), respectively. End-systolic and end-diastolic images are shown in all cases, together with x-t diagrams that refer to the orange line in the respective diastolic frame. (from Eirich et al. [102])

ited ventricular arrhythmia with complex premature contractions (A). X-t diagrams were included for both patients at the orange line drawn into the diastolic frame, respectively. The depicted time interval in Figure 4.9 (A) equals 2.2 seconds, whereas in the case of Figure 4.9 (B) three times the R-R interval of the gated reference matches 43 real-time frames of the CRISPI sequence.
The ECG-gated reference technique depends on a regular heartbeat for proper assignment of the acquired data to the correct cardiac phase. Irregularities in the heartbeat can impair this method and eventually lead to a falsified data sorting. This happened in the case of the arrhythmic patient shown in Figure 4.9 (A) and resulted in a spatiotemporally blurred image series. This can be seen in the x-t diagram of the gated reference in Figure 4.9 (A). Thus, the determination of end-systole and end-diastole was hampered, which finally can complicate clinical diagnostics. In contrast, the real-time CRISPI imaging technique was able to resolve the arrhythmic cardiac dynamics. The differences between the two CRISPI x-t diagrams in Figure 4.9 (A) are related to large breathing motion. It should be also mentioned that this patient experienced problems holding the breath, which can additionally complicate gated imaging. In the case of the patient presented in Figure 4.9 (B) (no arrhythmia), the different techniques in turn produced comparable results. Besides, the images already indicate a comparatively large left ventricle, which will be quantified in the next subsection.

4.1.5 Quantitative analysis of cardiac functional parameters

To comprehensively compare the gated reference with the CRISPI technique, the evaluation of quantitative cardiac functional parameters is necessary. For this reason, end-diastolic volume (EDV), end-systolic volume (ESV), stroke volume (SV) and ejection fraction (EF) were determined for the different methods, and are summarized in Figure 4.10 (A), (B), (C) and (D), respectively. The results of the gated reference and that of the CRISPI sequence in breath hold (BH) as well as free breathing (FB) are presented for all healthy participants (V1-V7) and patients (P1 and P2) in colors of blue, red and yellow, respectively. Moreover, all reference parameters were subtracted from the respective CRISPI parameters in breath hold and free breathing, and the mean differences with standard deviation (SD) were calculated (see Table 4.1). Figure 4.10 and Table 4.1 reveal that the values for all parameters are in good agreement with each other.

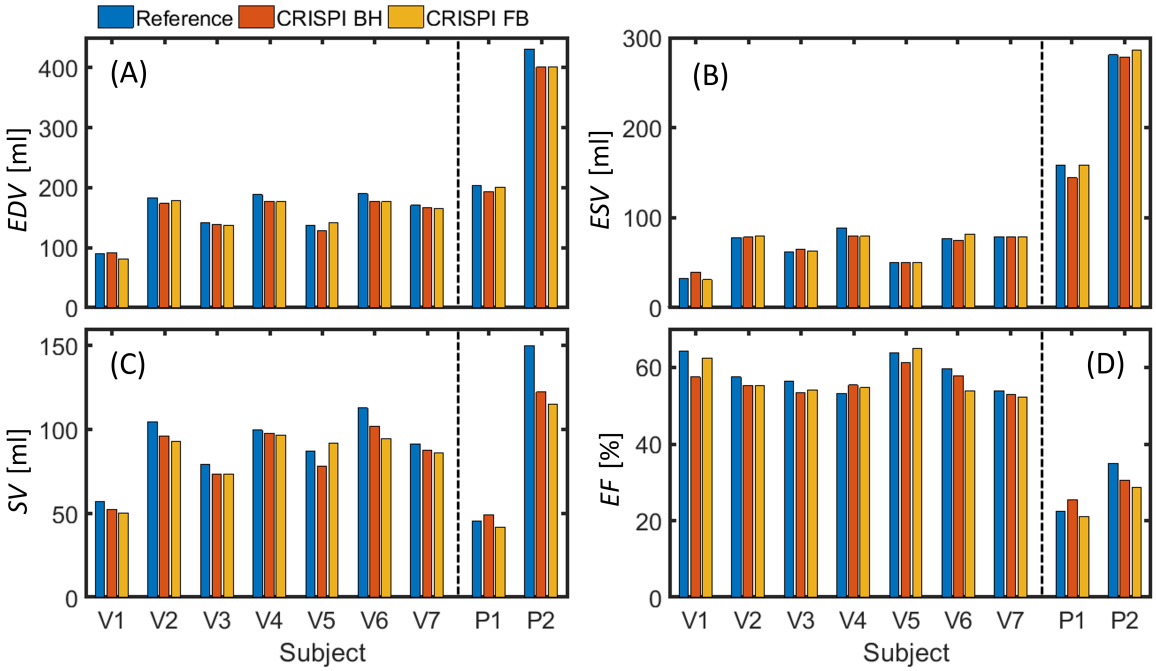

Figure 4.10: Cardiac functional parameters of end-diastolic volume (EDV), end-systolic volume (ESV), stroke volume (SV) and ejection fraction (EF) of the healthy volunteers (V1-V7) and the patients (P1 and P2). The values for the gated reference and the CRISPI acquisitions in breath hold (BH) and free breathing (FB) are shown in blue, red and yellow, respectively. (from Eirich et al. [102], modified)

	CRISPI vs. reference: mean differences with *SD*			
	EDV [ml]	ESV [ml]	SV [ml]	EF [%]
Breath hold	-9.71 ± 9.03	-1.94 ± 6.21	-7.61 ± 8.68	-1.81 ± 3.02
Free breathing	-8.29 ± 9.51	0.43 ± 4.13	-9.29 ± 11.38	-2.05 ± 2.58

Table 4.1: Mean differences with standard deviation (SD) after subtracting EDV, ESV, SV and EF of the gated reference from those of the CRISPI technique, for both breath hold (first row) and free breathing (second row).

Only in the case of P2 the values for the SV differ between the gated reference and the two CRISPI acquisitions. This could be related to the large left ventricle as already observed in Figure 4.9 (B), which furthermore causes the comparatively high values of EDV and ESV. The determined absolute values of EDV, ESV, SV and EF of the healthy participants match those of typical left-ventricular parameters presented in the literature [103]. Furthermore, the values of EF of the healthy volunteers represent normal cardiac pump function, while those of the patients represent moderately up to

severely abnormal cardiac pump function [77]. Lastly, a Wilcoxon signed-rank test was performed to test for statistical differences at the 5 % significance level between the reference and the CRISPI method. For this, the arrhythmic patient was excluded. The test failed at rejecting the null hypothesis for ESV and EF, however, the null hypothesis was rejected for EDV and SV. The statistical test did not yield any significant differences for the separate CRISPI acquisitions in breath hold and free breathing.

4.2 Phantom and in vivo results at 7 T

4.2.1 The GSTF

The results gathered from the measurements at the 7 T Terra system are presented in the following, beginning with the Gradient System Transfer Function (GSTF). The determined GSTF at 7 T is shown in Figure 4.11 and follows the presentation format of Figure 4.1 (GSTF at 3 T). The magnitude and phase of the GSTF self-terms can be seen in Figure 4.11 (A) and (B), respectively. One of the applied spiral readout gradients in frequency domain is displayed in Figure 4.11 (C) (see Figure 3.2 (B2) for temporal domain) and the inverted GSTF magnitude as used for the pre-emphasis in Figure 4.11 (D). The contributions of the x-, y- and z-axis are shown in colors of red, blue and green, respectively. Similar to the GSTF magnitude at 3 T, the 7 T scanner exhibits low-pass behavior as the transmission decreases with increasing frequency. Also, the magnitude of the z-axis exceeds that of the x- and y- axis for all frequencies. However, the detailed shape is scanner-specific as can be seen e.g. at the resonances that are highlighted as an inlay in Figure 4.11 (A). Comparatively large fluctuations were observed between $1 - 2$ kHz. The GSTF phase demonstrated approximately a linear shape in all spatial dimensions (note the undulating phase of the z-axis at 3 T). The dominant contributions of the spiral readout gradient presented in Figure 4.11 (C) again lie in the low-frequency spectrum, which was covered by the frequency range of the inverted GSTF magnitude determined by the cutoff frequency of 12.2 kHz (Figure 4.11 D).

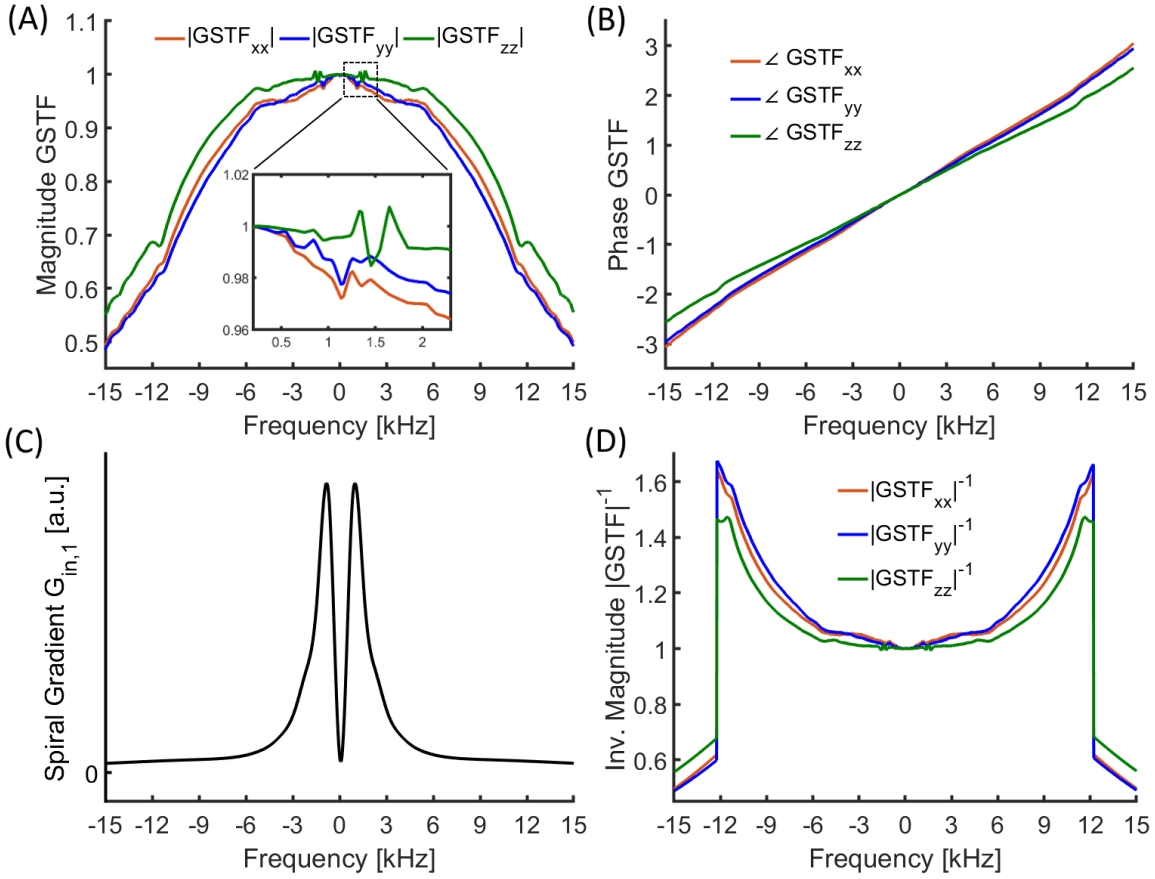

Figure 4.11: Magnitude (A) and phase (B) of the measured Gradient System Transfer Function (GSTF) at 7 T. The self-terms of the three physical dimensions x, y and z are depicted in red, blue and green, respectively, together with scanner-specific resonances (inlay of A). (C) and (D) show the magnitude of one of the spiral readout gradients in the frequency domain and the inverted GSTF magnitude applied to the automatic pre-emphasis, respectively.

4.2.2 Phantom results

In this subsection, the results of the phantom measurements performed at 7 T are summarized. To validate the applied pre-emphasis, the gradient output was measured and compared with the input. This is shown in Figure 4.12 (A1) and (B1) for both readout gradients that were used for the spiral 7 T acquisitions. Additionally, a detailed view of a local minimum is included for both gradients (Figure 4.12 A2 and B2). The pre-emphasized, nominal and measured waveforms (with and without pre-emphasis) are drawn in blue, black, green and orange, respectively. By playing out the pre-emphasized waveforms (blue curves), the scanner transmitted the originally

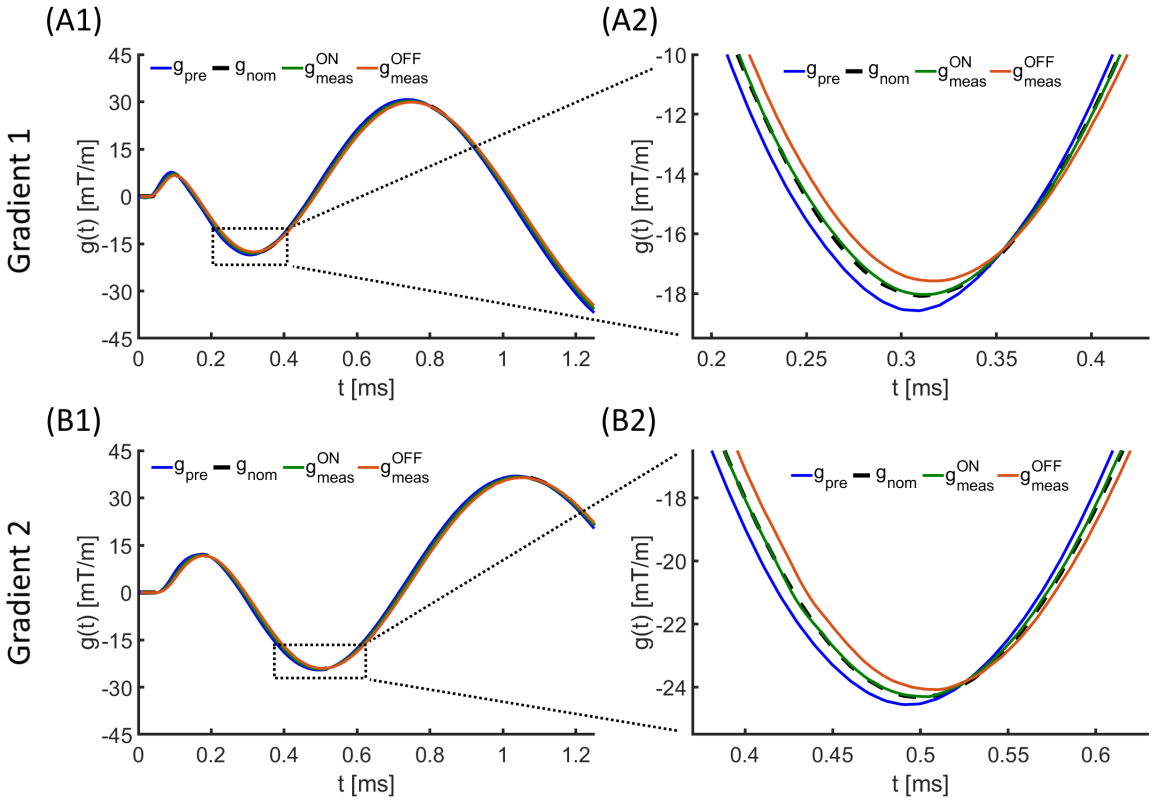

Figure 4.12: (A1) and (B1) compare the pre-emphasized, nominal and measured gradient waveforms (with and without pre-emphasis) for both spiral readout gradients in blue, black, green and orange, respectively. (A2) and (B2) show zoomed-in views of a local minimum.

intended waveforms (green curves match dashed black curves). However, a falsified output was transmitted (orange curves) in the case of playing out the gradients without GSTF pre-emphasis (dashed black curves).

Secondly, the GSTF pre-emphasis was applied to static measurements of a homogeneous, spherical phantom. For this, spiral imaging was performed with the pre-emphasized and nominal gradient waveforms as shown in Figure 4.12. The nominal k-space trajectory was used for image reconstruction. The resulting fully sampled images in transversal and coronal slice orientation are shown in Figure 4.13 (A) and (B), respectively. Figure 4.13 (A1, B1) correspond to the acquisitions without pre-emphasis and Figure 4.13 (A2, B2) to those with applied pre-emphasis. Line profiles shown in the second row of Figure 4.13 refer to the orange line drawn into the phantom images. When no trajectory correction is used, ghosting artifacts and signal pile-ups and voids are visible especially at the phantom border. However, when playing out the pre-emphasized gradient waveforms, the image quality increases as k-space sampling

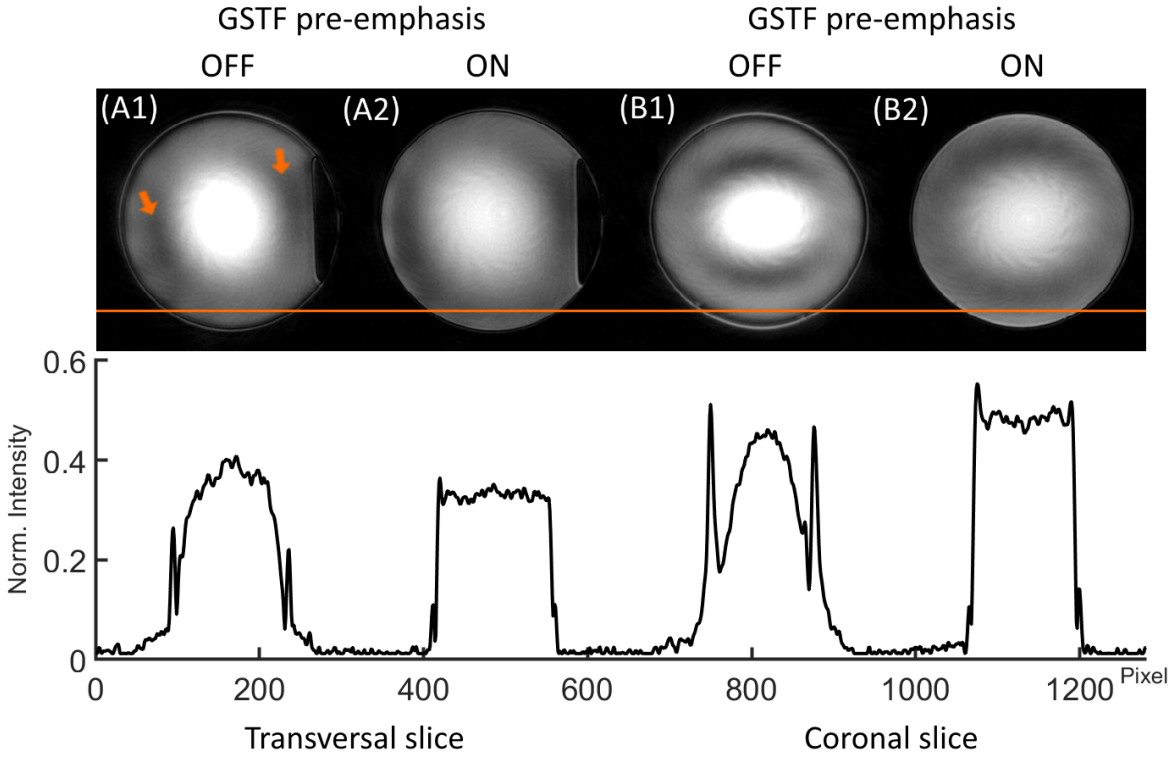

Figure 4.13: Transversal (A) and coronal (B) slice orientation of a spherical phantom, measured without (A1, B1) and with (A2, B2) GSTF pre-emphasis, respectively. The line profiles correspond to the orange line in the phantom images. B_1-inhomogeneity artifacts are exemplarily highlighted by orange arrows.

errors are mitigated. The line profiles support this observation. Without pre-emphasis, the pile-ups and voids present themselves as signal peaks at the phantom borders, and signal intensities appear to be impaired within the phantom. Both could be improved when applying the GSTF pre-emphasis. Lastly, image artifacts corresponding to B_1-inhomogeneities are exemplarily emphasized in Figure 4.13 (A1) by orange arrows. In these regions, destructive interference led to impaired signal intensity, which appears as darker areas in the images.

4.2.3 Gated CMR in human using a TWIRL k-space trajectory

In this subsection, the results of gated CMR are presented, which were acquired in a healthy participant with the golden angle $\text{TWIRL}_{\text{dip}}$ trajectory presented in Figure 3.3 (C). Sorting of data into the different cardiac segments was conducted using self-gating

by means of the k-space center signal of one coil element located close to the heart. The signal intensity over time is plotted in Figure 4.14 (A) and resulted from singular value decomposition with subsequent Savitzky-Golay filtering of the raw data. The duration

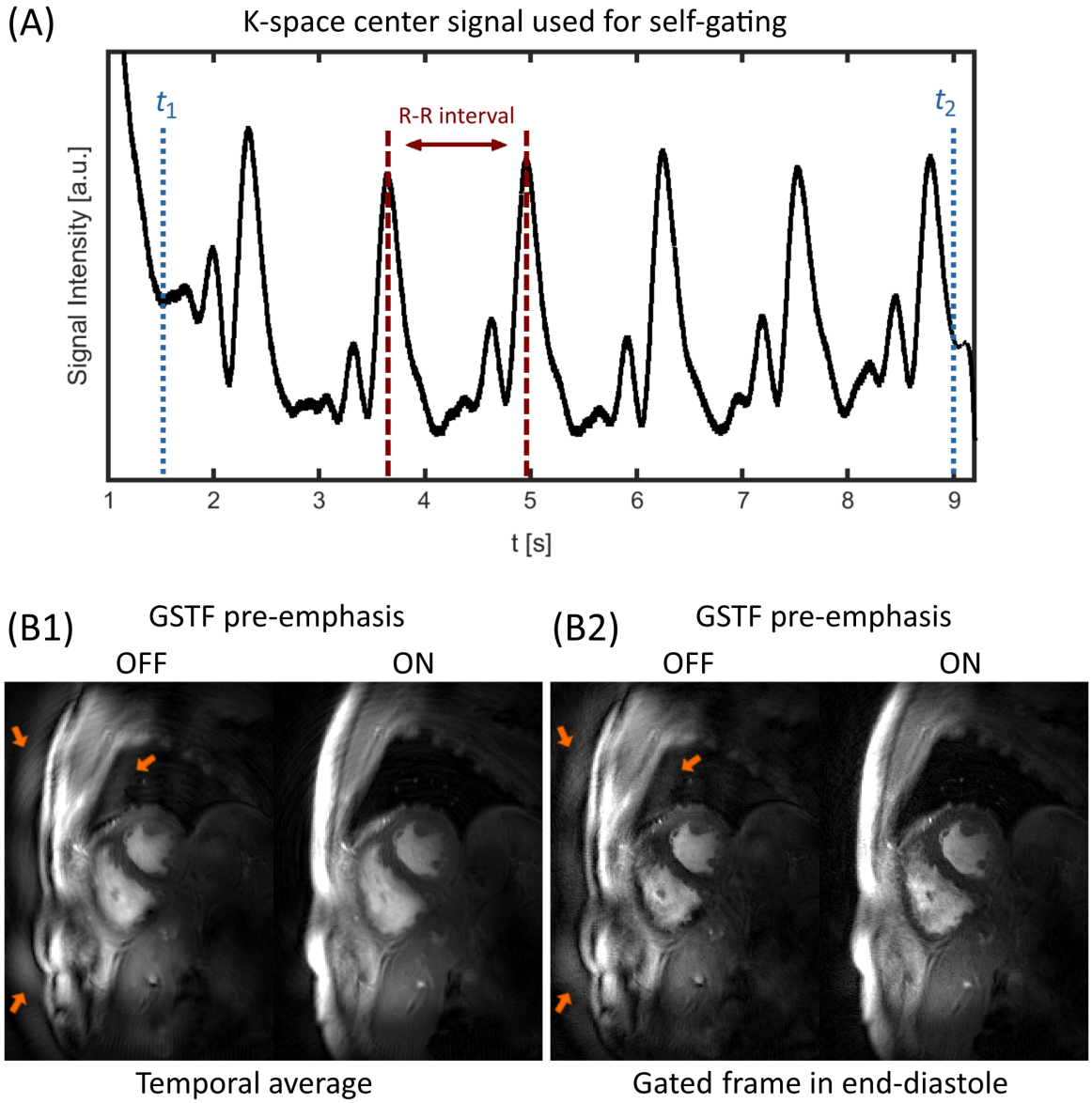

Figure 4.14: (A): K-space center signal of a coil adjacent to the heart that was used for self-gating. The duration of one R-R interval is emphasized by dashed red lines. The two dotted blue lines (t_1 and t_2) mark the start and end point of the data included into the segmentation process. (B): Performance of the applied GSTF pre-emphasis for a temporally averaged dataset (B1) and the gated frame in end-diastole reconstructed with compressed sensing (B2). Artifacts that are present when using no pre-emphasis are highlighted by orange arrows.

of one exemplary R-R interval is marked by two dashed lines in red, which corresponds to a heart rate of 46 min^{-1}. Additionally, the number of TWIRL interleaves used for segmentation ($N = 2501$) are enclosed by the two dotted lines in blue (marked by time point of start t_1 and end t_2). Figure 4.14 (B) demonstrates the in vivo performance of the applied GSTF pre-emphasis at 7 T. Images of the measurements without and with pre-emphasis of a fully sampled, temporally averaged dataset are depicted in Figure 4.14 (B1). To additionally analyze the interplay of trajectory artifacts and the compressend sensing (CS) algorithm, a gated frame reconstructed using CS is included in Figure 4.14 (B2). These images refer to the end-diastolic cardiac segment, one of in total 20 cardiac segments defined in the self-gating reconstruction step. In both cases (Figure 4.14 B1 and B2), artifacts due to k-space misregistrations are present in the images with GSTF pre-emphasis switched off (highlighted by orange arrows). However, they could be reduced by applying the pre-emphasized gradient waveforms instead of the nominal gradient waveforms (GSTF pre-emphasis switched on), which improved the overall image quality. Furthermore, the end-diastolic gated frame reveals a better contrast between myocardium and blood pool compared to the temporally averaged image.

Secondly, the performance of the CS reconstruction pipeline was tested by increasing the number of cardiac segments (#Seg.) in the self-gating procedure. This experiment is outlined in Figure 4.15 for the cases of the end-systolic gated frame with #Seg. $= 20 - 80$, which consequently affected the temporal resolution ($\Delta t = 65 - 16$ ms). The corresponding images using zero filling only and the CS reconstruction are presented in Figure 4.15 (A) and (B), respectively. To outline cardiac dynamics, twice the R-R interval is included in (B) in terms of x-t diagrams refering to the position of the orange dotted line. Changing #Seg. means that less TWIRL interleaves of the total number of $N = 2501$ are available for each cardiac segment. To demonstrate the degree of undersampling, the k-space trajectory that belongs to the respective end-systolic frame is depicted in Figure 4.15 (C).
These images show that the degree of undersampling increases for higher values of #Seg. Secondly, the golden angle sampling pattern successfully results in reasonably uniform 2D k-space coverage. However, in all cases comparatively large k-space voids remain and their sizes also increase for higher values of #Seg. A higher degree of undersampling consequently results in more pronounced image artifacts due to aliasing, as can be traced by the image series of Figure 4.15 (A). On the other hand, the CS framework managed to yield similar image quality in all four cases of #Seg. (see the

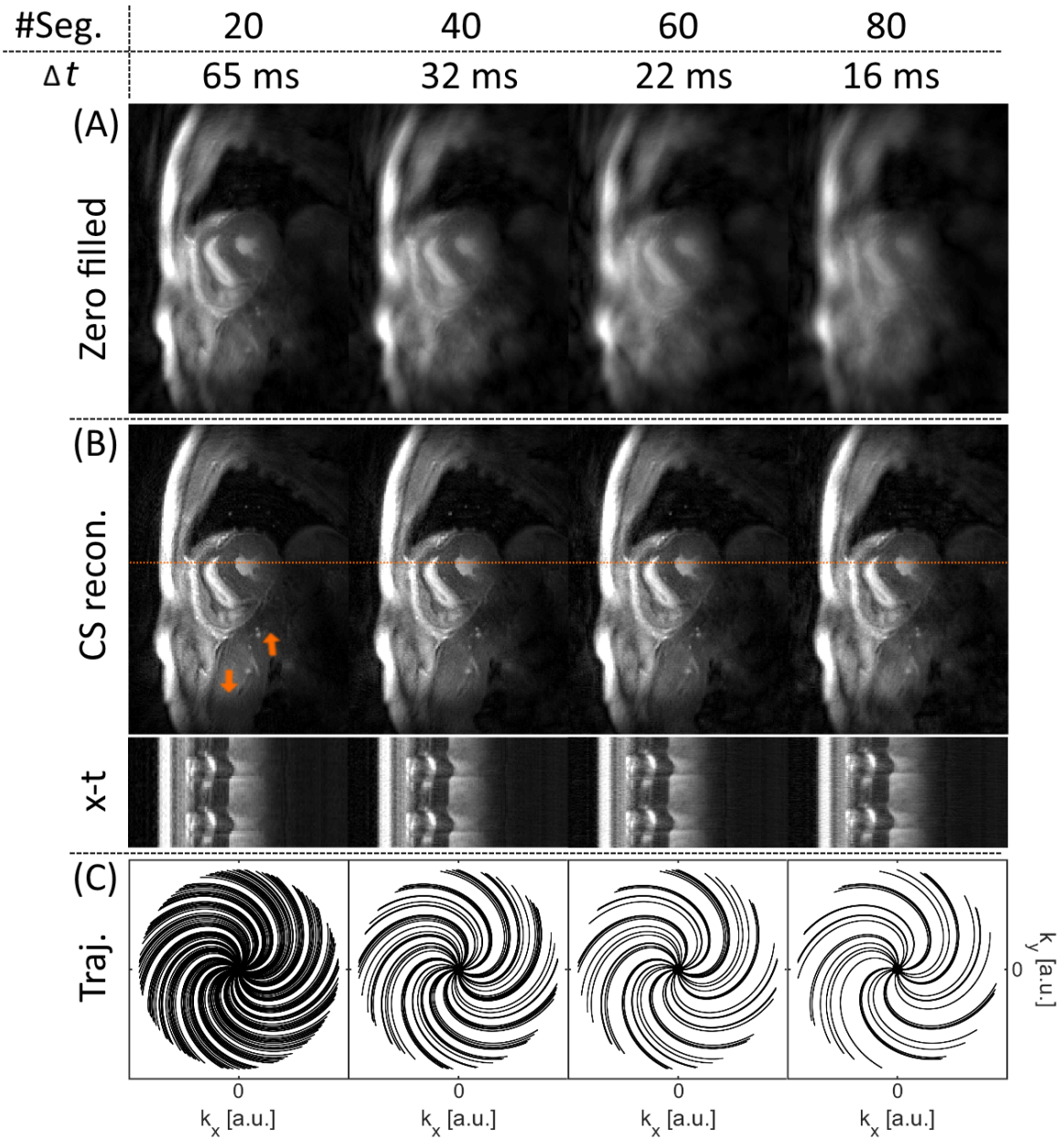

Figure 4.15: Performance of the compressend sensing (CS) reconstruction of a mid-ventricular SAX slice for a different number of cardiac segments applied during self-gating (#Seg. in a range of $20 - 80$). They correspond to a temporal resolution of $\Delta t = 65 - 16$ ms. The end-systolic gated segment of the zero filled and the CS reconstructions are shown in (A) and (B), respectively, and refer to the undersampled k-space trajectories given in (C). B_1-inhomogeneity artifacts are exemplarily highlighted by orange arrows. X-t diagrams of twice the R-R interval correspond to the position of the dotted orange line.

image series of Figure 4.15 B). However, the overall artifact power seems to gradually increase to a low extent from #Seg. = 20 to #Seg. = 80. The x-t diagrams demonstrate comparable quality in resolving cardiac dynamics. The temporal resolution of $\Delta t = 32\,\text{ms}$ already seems to be sufficient to precisely resolve the R-R interval. Moreover, image artifacts corresponding to B_1-inhomogeneities are exemplarily marked in Figure 4.15 (B) by orange arrows. Lastly, note that only the signal of the coil elements located above the participant were used for image reconstruction. The second coil element located underneath the participant led to strong amplifications of signal intensity in fat and therefore was excluded. This additionally degraded signal intensity especially in the posterior region of the participant, which e.g. caused poor visibility of the posterior wall of the myocardium (see x-t diagrams of Figure 4.15 B).

4.2.4 Real-time CMR in pig using spiral k-space trajectories

The results chapter is completed by this subsection, in which the spiral real-time CMR images of the pig measurements in free breathing at 7 T will be presented. The in vivo performance of the trajectory correction using the GSTF pre-emphasis is demonstrated in Figure 4.16. To separate image artifacts due to trajectory misregistrations from potential residual aliasing, a midventricular slice in SAX orientation is shown both as a fully sampled temporal average (Figure 4.16 A) and in the form of end-diastolic real-time frames using the compressed sensing (CS) reconstruction (Figure 4.16 B). All images were reconstructed with the nominal k-space trajectory. Here, the undersampled k-spaces of each real-time frame were covered with $N_{\text{RT}} = 20$ equidistantly distributed spiral interleaves, which resulted in a temporal resolution of $\Delta t = 64\,\text{ms}$. Images that refer to measurements without and with pre-emphasis are presented in both cases (first and second column of Figure 4.16). To investigate the impact of off-resonance related artifacts, the rawdata of the measurement with applied pre-emphasis was additionally reconstructed using a frequency offset of 615 Hz (third column of Figure 4.16). K-space trajectory artifacts using no pre-emphasis correction are marked by orange arrows, which could be mitigated by switching on the GSTF pre-emphasis. However, the reconstructed images exhibited blurring, which is not only present in the temporally averaged images but also in the end-diastolic real-time frames (emphasized by blue arrows). This could be improved by applying the empirically determined frequency offset and resulted in high resolution SAX images. Note the high contrast between myocardium and blood pool in the CS images compared to the temporally

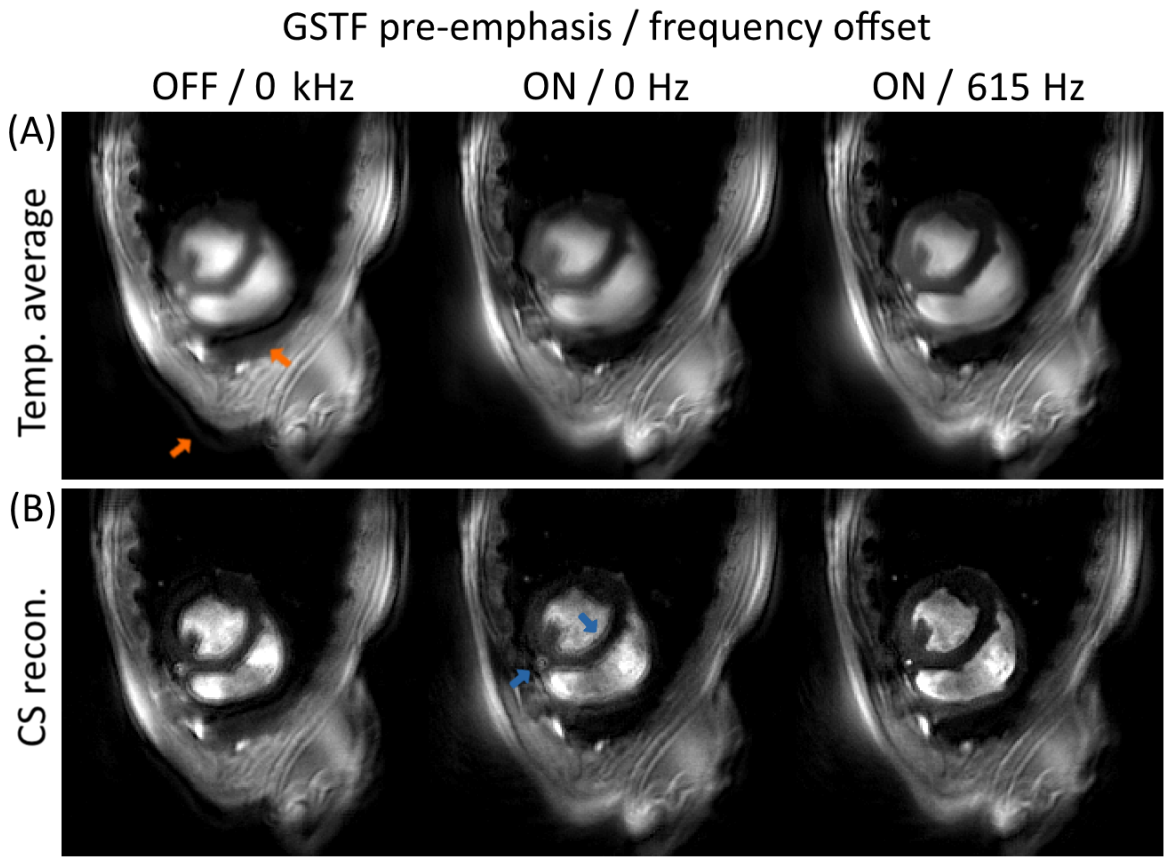

Figure 4.16: Midventricular SAX slice of a pig acquired in free breathing and reconstructed as a fully sampled temporal average (A) and with the compressed sensing (CS) algorithm for the case of an end-diastolic real-time frame (B). Images of measurements without as well as with GSTF pre-emphasis are shown. In the last column, an additional frequency offset of 615 Hz was used in image reconstruction. Image artifacts due to trajectory errors and off-resonance are highlighted by orange and blue errors, respectively.

averaged images. Solely regions with fat tissue exhibited some residual blurring or locally bright signal intensity. In general, the images of Figure 4.16 reveal a uniform distribution of signal intensity of the examined tissue, which can be associated with the in-house built coil array that was optimized to the size of the animal [99–101].
Secondly, the degree of aliasing was investigated by repeating the measurement with the spiral sampling pattern of $N_{\mathrm{RT}} = 10$ ($\Delta t = 32\,\mathrm{ms}$). This comparison is demonstrated in Figure 4.17 by showing end-systolic real-time frames of a midventricular slice in SAX orientation. Both acquisitions were performed with applied GSTF pre-emphasis in free breathing, and the rawdata was reconstructed using the nominal k-space trajectories and the same off-resonance frequency offset of 615 Hz. The reconstructed images using zero filling and the CS algorithm are presented in Figure 4.17

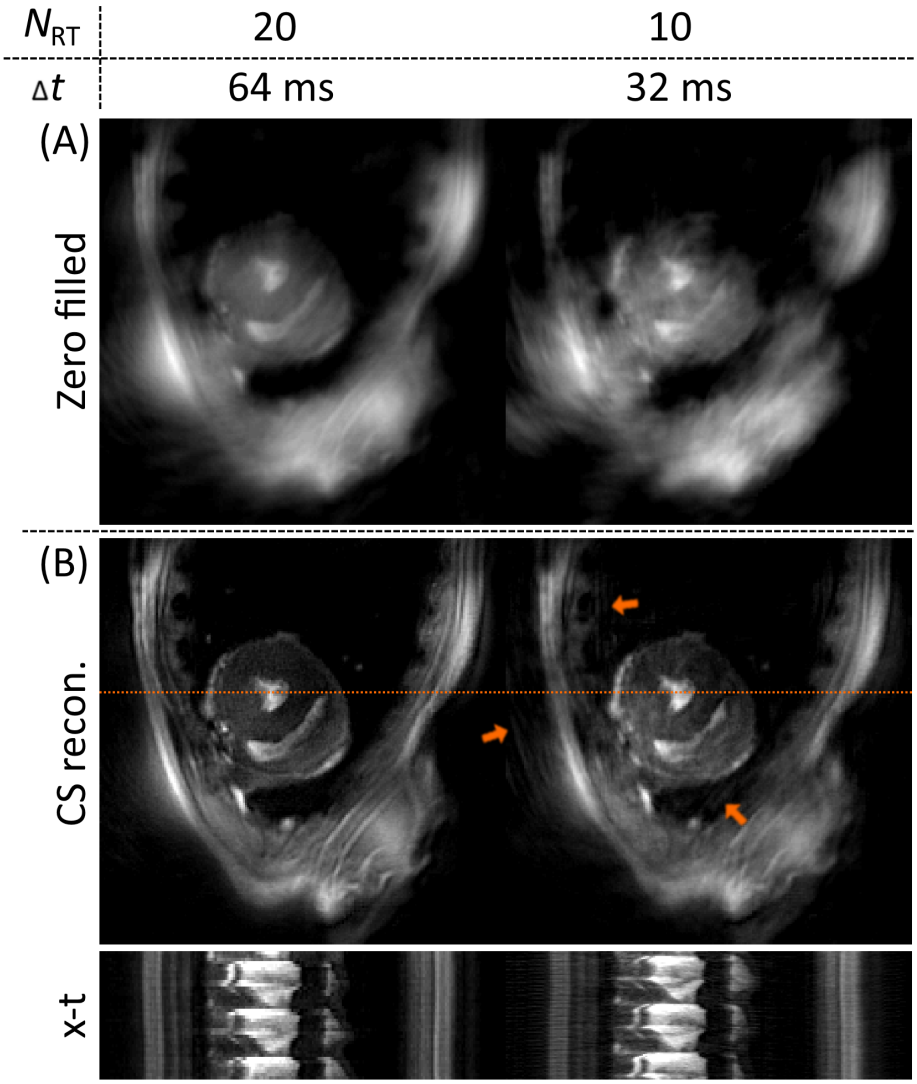

Figure 4.17: End-systolic real-time frames in midventricular SAX orientation of a pig acquired in free breathing. Images using zero filling and the CS reconstruction are depicted in (A) and (B), respectively, for two different temporal resolutions of $\Delta t = 64\,\text{ms}$ and $\Delta t = 32\,\text{ms}$. They correspond to $N_{RT} = 20$ and $N_{RT} = 10$ equidistantly distributed spiral interleaves in each real-time frame. The frequency offset of 615 Hz was also applied in these images. The x-t diagrams refer to the dotted orange line and show 40 and 80 consecutive real-time frames, respectively. Residual aliasing is emphasized by orange arrows.

(A) and (B), respectively. The two columns refer to the two different spiral k-space trajectories using $N_{RT} = 20$ and $N_{RT} = 10$. The x-t diagrams shown in Figure 4.17 (B) correspond to the orange dotted line drawn into the CS images and show 40 and 80 consecutive real-time frames, respectively. Figure 4.17 (A) presents the impairment of image quality due to k-space undersampling, which is considerably increased in the

case of $N_{\mathrm{RT}} = 10$. No image artifacts due to aliasing were observed using the CS framework for $N_{\mathrm{RT}} = 20$. Aliasing could be also reduced in the CS image of $N_{\mathrm{RT}} = 10$. However, residual artifacts are traceable, which are highlighted by orange arrows. The x-t diagrams reveal similar quality. Nevertheless, the temporal resolution of $\Delta t = 32\,\mathrm{ms}$ is visually superior to $\Delta t = 64\,\mathrm{ms}$, as the latter seems to be at the limit to resolve the details of cardiac dynamics.

5 Discussion

The aim of this work was the development of accelerated MRI strategies with the application to imaging and analyzing cardiovascular tissue with high spatiotemporal resolution. To achieve this, two key components were combined. Firstly, efficient and accurate non-Cartesian k-space sampling and secondly, image reconstruction of undersampled k-space data using compressed sensing (CS). Different k-space trajectories were created to enable rapid data acquisition of the beating heart in free breathing, optimized to the respective MR scanner at 3 T and 7 T.

A main limitation of non-Cartesian acquisitions were image artifacts due to k-space misregistrations, which impaired the image quality. Here, Gradient System Transfer Functions (GSTFs) were determined by measuring the impulse response of a MR scanner's gradient system, which served as a robust setup to correct trajectory errors. One advantage of this method is that the scanner-specific GSTF can be calculated from a unique acquisition, as its shape exhibits only little change over time [62, 70]. Furthermore, the phantom-based approach that was applied in this work does not depend on additional expensive hardware, which enables a rapid and straightforward implementation on any MR scanner [62, 70, 72–75, 102]. Here, this framework was established on two different MR scanner models, a 3 T Prisma and a 7 T Terra system. The multiplication with the GSTF in the frequency domain can be performed with any readout gradient, which means that the correction step is independent of the k-space trajectory. In this work, this was exemplarily demonstrated by applying spiral as well as TWIRL k-space trajectories at the 7 T Terra system. The cutoff frequency for the inverted GSTF magnitude may need to be increased for the pre-emphasis of readout gradients with considerably higher frequency contributions, as e.g. could be the case in echo-planar diffusion imaging [104]. The chosen cutoff frequency of 12.2 kHz provided sufficient frequency coverage of the different applied non-Cartesian gradient waveforms. A possible improvement of the inversion of the GSTF magnitude could be

achieved by implementing a decaying function such as a Fermi-Dirac function rather than a cutoff. Additionally, the performance of the pre-emphasis could be increased by including the GSTF cross-terms.

One of the novelties of this work was the implementation of the GSTF pre-emphasis as a fully automatic procedure, enabling not only the correction of arbitrary k-space trajectories but also randomly orientated, double-oblique slice positions. This is of special interest in cardiovascular applications (CMR) as the different views rely on double-oblique slice orientations, which need to be manually adjusted by the user and are different for each patient or participant. When using the pre-emphasis, images can be reconstructed using the nominal k-space trajectory in all cases. This simplifies the entire imaging process as solely the gradient waveforms of interest must be embedded in the sequence code. No further efforts in terms of gradient preparation in advance or trajectory correction in post-processing are necessary. In literature, many studies that conducted spiral CMR did not include a correction of k-space misregistrations [88, 89, 95, 105]. Some studies exploited the GSTF to determine true k-space trajectories, which they subsequently employed in image reconstruction [62, 70–72]. Tan and Meyer proposed an estimation model for gradient delays with additional eddy current compensation for brain imaging [64], which was applied by Feng et al. [92] to spiral real-time CMR.
In this thesis, besides the GSTF pre-emphasis, k-space trajectory errors at 3 T were additionally compensated using optimized global delays only. The comparison revealed that image artifacts could already be reduced by applying global time delays. However, the comprehensive GSTF correction that uses the axis- and frequency-specific impulse response of the gradient system further enhanced the final image quality.

A key aspect of the present work was the design of optimized k-space trajectories with the focus on spiral sampling patterns. The MATLAB toolbox of *Brian Hargreaves* [98] served as simple and effective instrument to flexibly create spiral gradient waveforms. At 3 T, a specific spiral sampling pattern was established to enable high resolution real-time CMR (CRISPI technique [102]). The spatial resolution was set to $(1.34 \times 1.34)\,\mathrm{mm}^2$ and the temporal resolution to 49.6 ms. Spiral real-time images at 7 T were gathered with resolutions of $(1.14 \times 1.14)\,\mathrm{mm}^2$ and $32 - 64$ ms, respectively. The spatial resolution can be easily adjusted by changing the amplitude of the readout gradients, constrained by hardware limitations of maximum slew-rate and amplitude, or by physiological limitations due to nerve stimulation. The temporal resolution can

be set by tuning the number of spiral interleaves that cover the undersampled k-space of each real-time frame, which was tested for values of $N_{\mathrm{RT}} = 10 - 20$ at 7 T. Note that a temporal resolution of < 50 ms (> 20 frames per second) is recommended to evaluate cardiac function [82, 83]. In general, there exists a trade-off between image quality and spatiotemporal resolution. If the applied CS model is overfitted, temporal blurring can impair the diagnostic evaluation of the cardiac dynamics. This is why the focus always lied on preserving cardiac dynamics, which on the downside resulted in residual aliasing for small values of N_{RT}.

In addition to spiral k-space sampling, a hybrid TWIRL trajectory was tested and applied to gated CMR at 7 T. The main purpose was to test further improvements of spiral sampling patterns as it would be reasonable to move as fast as possible out of the anyway oversampled k-space center. At the same time, sampling efficieny was intended to be maximized by exploiting the powerful gradient system to its maximum extent. In the case of moving linearly through k-space with maximum slew-rate and amplitude, the sampled k_{max} would be too high, even for short readout durations. In order to keep the slew-rate high, curved lines need to be embedded in the k-space trajectory. As a result, the radial beginning of the applied $\mathrm{TWIRL}_{\mathrm{dip}}$ trajectory was kept short compared to the subsequent curved part of the trajectory. Secondly, some time can be saved by additionally using the time of the slice selection rephaser to move through k-space. The chosen trajectory resulted in a spatial resolution of $(1.39 \times 1.39)\,\mathrm{mm}^2$ and the temporal resolution yielded values between $16 - 65$ ms, depending on the number of cardiac segments in which the data was sorted. The x-t diagrams revealed that cardiac dynamics could be sufficiently resolved by a temporal resolution of 32 ms and that no visible improvement could be linked to higher temporal resolutions. Naturally, this also depends on the heart rate of the participant or patient. In accordance with the real-time results, aliasing impaired the image quality for high numbers of cardiac segments. Again, spatial resolution could be further improved by increasing the amplitude of the readout gradients.
In all cases, the applied low rank plus sparse CS model [60] mitigated image artifacts due to incoherent aliasing. The results endorse the concept of CS as an important and powerful tool for accelerated data acquisitions, which is crucial for high resolution CMR applications [95, 105–107]. Moreover, the growing field of machine learning provides a novel and promising basis to further improve the reconstruction performance of undersampled k-spaces, not only in terms of image quality but also reconstruction speed [108].

In comparison with other cardiac real-time publications that utilized spiral data acquisition at 1.5 T or 3 T [88, 89, 92, 105], the spatial resolution of the CRISPI sequence applied in the present work is higher [102]. Also, complete images required measurement times of > 100 ms [92] and a temporal resolution of > 50 ms was realized by sliding window reconstructions [88, 89]. Steeden et al. [105] realized a spatial resolution of 1.7 mm and a temporal resolution of 30 ms by performing 8-fold accelerated spiral imaging with a tiny golden angle increment and CS-based reconstruction at 1.5 T. Another important aspect is that many CMR studies [89, 92, 105] apply balanced steady state free precession (bSSFP) instead of gradient echo (GRE) pulse sequences, because bSSFP sequences generally exhibit a higher contrast between myocardium and blood pool. In bSSFP imaging, however, all gradient moments must be balanced, which either lengthens the TR or shortens the time available for data acquisition, both to the disadvantage of real-time imaging. An improvement of spatiotemporal resolution so far could only be achieved by Zhou et al. [32] by performing gated imaging at 3 T with a GRE sequence that applied undersampled spiral k-space sampling. Here, this was also demonstrated in the study of gated CMR at 7 T with the TWIRL k-space trajectory (Section 4.2.3), which resulted in temporal resolutions of up to 16 ms.
In general, real-time studies often provide image reconstruction directly online at the MR scanner, e.g. by incorporating no or only little k-space undersampling. All acquired spiral data presented in this thesis were reconstructed offline, such that the images were not immediately available after scanning but only after reconstruction in MATLAB. In order to enable rapid evaluation of cardiac function as part of an examination in clinical routine, image reconstruction needs to be translated to the software environment at the scanner.

A part of this work compared the developed spiral real-time CRISPI sequence with ECG-gated Cartesian GRE imaging at 3 T, as it represents a reference technique for a standard clinical MR examination to evaluate cardiac function. As a result, both methods yielded similar image quality. However, the CRISPI framework entails several advantages. Firstly, the measurement can be performed in free breathing. In combination with the rapid and efficient spiral sampling pattern, whole heart coverage in SAX orientation could be achieved in less than 50 seconds. The Cartesian reference needs to be performed in several breath holds, which usually takes between 5-10 minutes as the duration of pauses for breathing depend on the health of the patient or participant. Consequently, the CRISPI sequence enables increased patient comfort and significantly simplifies CMR examinations. In severe cases, patients are not capable to hold the breath for several seconds. This could lead to the necessity to repeat the

measurement or even excludes the patient from the MR examination. From an economical point of view, shortened imaging times involve a cost reduction, which could have an impact on the general accessibility of CMR examinations [102].
To be a robust alternative to the Cartesian reference, the results of the CRISPI framework must also coincide quantitatively. Therefore, cardiovascular volumetric and functional parameters were determined. They showed good agreement for all three applied methods, Cartesian reference and CRISPI in both breath hold and free breathing. The high value of the SV in patient 2 in the case of the reference could be linked to the large size of the left ventricle (EDV $> 400\,\mathrm{ml}$). As a consequence, fluctuations in the determination of the EDV could affect the SV to this extent.
The Wilcoxon signed-rank test yielded systematic deviations in the cases of EDV and SV, which means that the CRISPI method led to a small but significant underestimation of the two parameters. However, the small sample size ($N = 8$) reduces the power of the statistical test. Exemplarily, a second test was performed, in which patient 2 was excluded (additionally to patient 1 due to the arrhythmia) and no systematic deviation was present for the EDV determined by the CRISPI method in free breathing. To increase the reliability of the test, a larger clinical study should be conducted.
If CMR measurements are performed in free breathing, through-plane motion could have an impact on the investigation of quantitative cardiovascular parameters. However, the differences of the CRISPI technique in free breathing compared to the two breath-held acquisitions are small, which underlines both the technical as well as the clinical robustness of the established CRISPI method.

So far, spiral imaging in humans at 7 T is a highly novel field of research as comparatively few publications can be found in literature [36, 109–112]. In recent years, the first ultra-high-field (UHF) MR scanners received a license for clinical use [7, 113]. Moreover, their accessibility and benefits are hampered not only by high acquisition costs but also by hardware limitations, such as magnetic field inhomogeneities or SAR restrictions due to an increased energy deposition. In addition, RF coil design is more complex, which is why the number of available coil arrays is still low [113]. As the wavelength of the transmitted RF pulse is shorter, destructive interference can lead to signal dropouts. This was observed in the results of the homogeneous phantom as well as in the results of the gated CMR study using the TWIRL k-space trajectory, and presented itself as dark regions, respectively (see Figure 4.13 and Figure 4.15).
Many spiral 7 T studies were conducted in the field of brain imaging [36, 109–112], which has the advantage that there is no moving tissue. In terms of artifact compensation, most studies focused on the reduction of blurring due to off-resonance rather

than trajectory correction due to gradient imperfections. As B_0-inhomogeneity at 7 T increases, so does the spatially varying mismatch between the frequency of the applied RF pulse and that of the spins' *Larmor* precession. This phase accumulation broadens the point spread function, which results in blurring in the case of spiral imaging [114]. Also, this effect scales with the readout duration, which is why the non-Cartesian imaging protocols in this work were implemented with comparatively short readout durations of approximately 1.3 ms. In the human in vivo images of self-gated CMR using the TWIRL k-space trajectory in breath hold, high quality results could be achieved without implementing an off-resonance correction method. However, the results gathered from the spiral real-time acquisitions in the pig in free breathing demonstrated that an off-resonance correction could significantly reduce the present blurring. A reason for this could be differences in the applied shim, e.g. vendor-provided field map estimations could suffer a frequency offset in some cases [115]. Anatomical differences between humans and pigs could also influence the B_0-homogeneity of the shimmed cardiac volume. However, as the readout durations of the TWIRL and the spiral measurements were similar, a mismatch of the resonance frequency in the pig study seems to be more likely.

Here, a spatially invariant frequency offset was applied in image reconstruction as one of the easiest approaches to compensate for off-resonance artifacts. The degree of blurring in combination with the applied readout duration and frequency offset visually coincides with the results presented in the study of Lim et al. [116]. However, the shimmed volume of the human heart at 7 T usually exhibits a non-isotropic B_0-inhomogeneity distribution [115]. More sophisticated approaches are often based on retrieving the spatially varying off-resonance information from field maps, which are either separately acquired or inherently available from the data [117–122]. The study of Engel et al. [36] demonstrated the extreme scenario of a single-shot acquisition with readout durations up to 53 ms. In these cases, an off-resonance correction method is inevitable.

The presented results at 3 T revealed that high resolution images are feasible without implementing an off-resonance correction. At most, slight blurring was observed in regions with fat tissue, which did not affect diagnostic capabilities of the heart. This is supported by the study of Zhou et al. [32], which determined that no off-resonance correction is requisite to achieve acceptable results in CMR imaging at 3 T in the case of readout durations shorter than 5 ms. In the work of Nayak et al. [88], spiral real-time imaging at 3 T was performed using readout durations longer than 8 ms, and a field map-based off-resonance correction technique was applied.

Independent of the field strength, CMR studies are more complex than e.g. static brain imaging, as there is moving tissue. But especially at 7 T, even the gold standard of ECG-gated Cartesian GRE imaging becomes challenging, not only because of B_0- or B_1-inhomogeneities but also because of a possibly corrupted ECG-signal due to the magnetohydrodynamic effect [123, 124]. This underlines the additional impact real-time imaging can have for UHF CMR, besides the problem of long imaging times in gated CMR. Furthermore, bSSFP sequences are particularly challenging at UHF due to SAR limitations and enhanced banding artifacts [113, 123]. The application of spoiled GRE sequences in combination with low flip angles prevented SAR problems in the present studies at both 3 T and 7 T. In general, recent human CMR studies at 7 T are mostly based on standard Cartesian sampling patterns [124–128]. However, spiral CMR applications at 7 T were already performed in animals, as e.g. in the study of Castets et al. [129], in which a stack-of-spiral sequence was applied to 3D T_1 mapping of the heart in mice.

Lastly, it should be mentioned that there is an ongoing discussion related to the usage of the phrase "real-time MRI" [130–132]. Dietz et al. [130] explained that "real-time MRI" does not only refer to an image series, in which each frame corresponds to a unique time-point of a dynamic process. It would also suggest that the reconstructed images should be accessible immediately after data acquisition with low latency. Nayak [132] disagreed because of the significant benefit that is offered even without low-latency reconstruction, e.g. that major efforts in engineering are required to omit gating in CMR.
The author of this dissertation agrees with Nayak, which is why the phrase "real-time MRI" was used throughout this work. Here, the focus lied on accelerating the data acquisition process together with the optimization of offline reconstruction techniques in terms of high-quality real-time CMR. This means that no special effort was made to minimize reconstruction time. Several hours were needed to reconstruct all slices of a dataset that included whole heart coverage in SAX orientation. An efficient implementation on a graphics processing unit (GPU) or machine learning techniques such as the variational network approach presented by Hammernik et al. [108] could substantially accelerate the reconstruction process. This potentially represents the missing step in embedding the CRISPI framework into clinical routine.

6 Conclusion

In conclusion, this work presented various measures to promote the field of rapid MRI. In particular, the combination of accelerated data acquisition and enhanced spatiotemporal resolution requires substantial efforts in different areas of MRI research. Firstly, todays powerful gradient systems facilitate highly efficient non-Cartesian k-space trajectories. This means that a significantly larger k-space path can be covered in each readout by e.g. spiral sampling compared to conventional Cartesian sampling. In addition to that, a high sampling precision can be achieved by including the simple and robust approach of determining the MR scanner's Gradient System Transfer Function (GSTF). Importantly, a trajectory correction was introduced by implementing a fully automatic GSTF pre-emphasis into the pulse sequence code, which resulted in higher image quality compared to a global delay compensation.

Furthermore, model-based reconstruction methods such as CS allow for high undersampling of k-space, because missing k-space positions can be reproduced during image reconstruction to suppress incoherent aliasing. Especially dynamic processes benefit from this setup, which was demonstrated by resolving the beating heart in real time with high spatiotemporal resolution. An entire CMR measurement could be realized in less than 1 minute in free breathing. The increase in both time efficiency and patient comfort can improve accessibility and acceptance of MRI as a major imaging modality to examine cardiovascular diseases.

One of the most important measures of image quality in MRI or other imaging modalities is the SNR. First and foremost, UHF strengths offer an increased SNR, which facilitates to reduce the voxel size or the acquisition time, both of substantial importance in MRI. On the opposite side, UHF imaging struggles with limitations such as magnetic field inhomogeneities or SAR issues due to RF pulses of higher energy. Images of high quality were produced at both field strengths, 3 T and 7 T. However, there is still work ahead in MRI research and engineering to overcome the present difficulties of UHF imaging in order to use 7 T scanners in todays clinical routine more often.

7 Outlook

To improve the developed setup of rapid non-Cartesian CMR, the following steps could be performed in future works. Firstly, the GSTF correction could be optimized by implementing a decaying function instead of the current pseudo-cutoff in the inversion of the GSTF magnitude. Also, an increased frequency resolution in the GSTF measurement and an incorporation of the GSTF cross-terms could improve the performance. In addition to that, the GSTF pre-emphasis could be transferred to other gradients applied in a pulse sequence, apart from the non-Cartesian readout gradients. Furthermore, a more comprehensive off-resonance correction could be implemented for cases of increased readout durations, especially at 7 T. Moreover, long reconstruction times are an obstacle for an application of the current framework in clinical routine. The upcoming field of machine learning, e.g. convolutional neural networks, forms a promising basis to accelerate image reconstruction of undersampled k-space data. And lastly, the GSTF correction could be implemented into bSSFP sequences, which potentially improves the quality of CMR, e.g. in terms of image contrast.

Apart from this, the real-time imaging pipeline could also be transferred to other dynamic in vivo applications, e.g. the process of human swallowing or speaking. This was tested within a proof of concept study at 3 T by applying the CRISPI framework to a healthy volunteer that was asked to swallow a small amount of water on command. A selection of the reconstructed image series is presented in Figure 7.1 (A-H). In the bottom right part of each real-time frame the corresponding time point is given. They enclose a time duration of 1.84 seconds. Additionally, the position of the water is highlighted by an orange arrow in each frame, respectively. The high temporal resolution ($\Delta t = 49.6\,\mathrm{ms}$) allows the detailed visualization of the water entering the oral cavity, passing the pharynx and ending into the esophagus. To give a further example of the high spatiotemporal resolution, Figure 7.1 (I) was included, in which a detailed view of the palatine uvula is shown (dotted orange box).

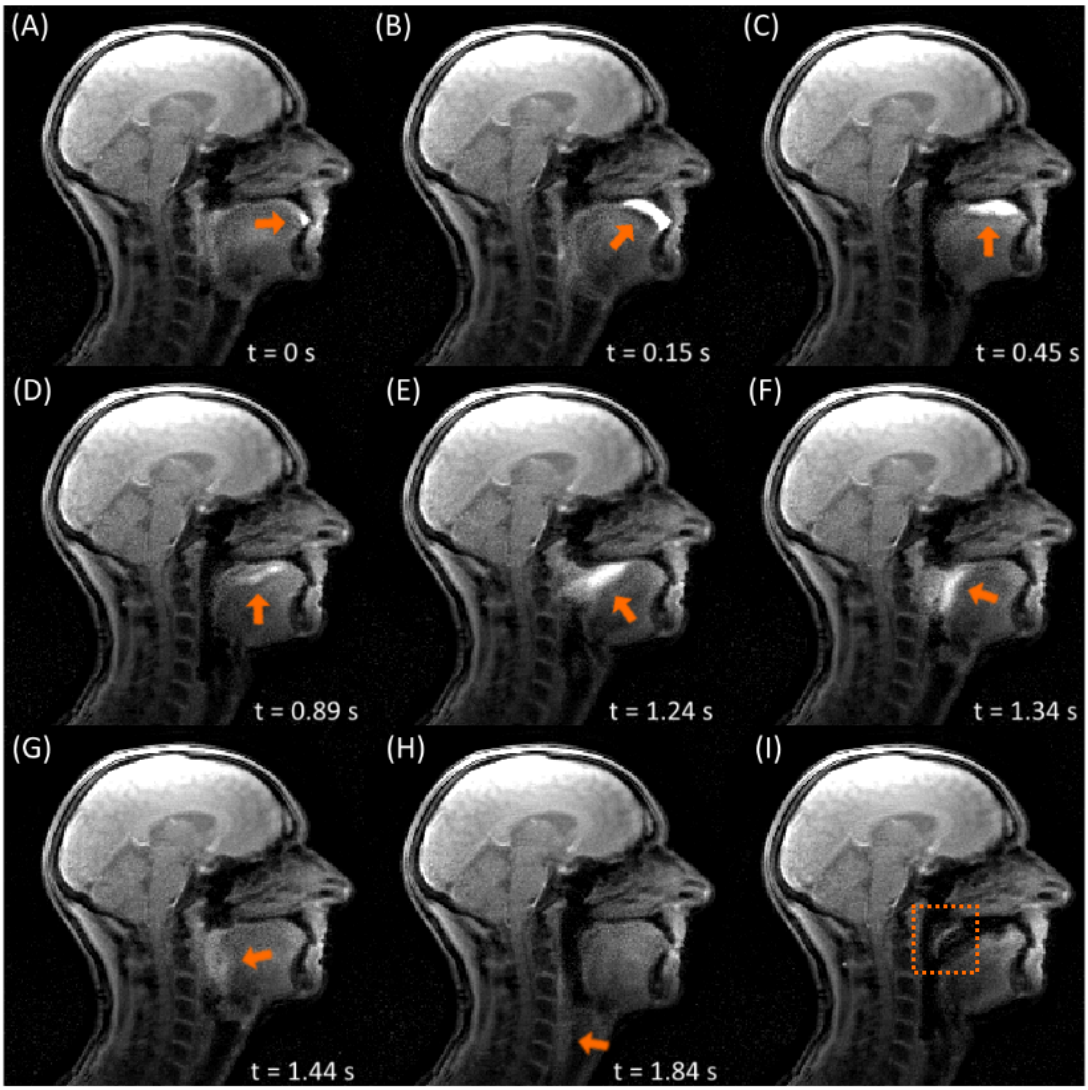

Figure 7.1: Spiral real-time imaging of a swallowing process in a healthy participant of 1.84 seconds duration using water (A - H), highlighted by orange arrows. The marked area in (I) shows a detailed view of the palatine uvula.

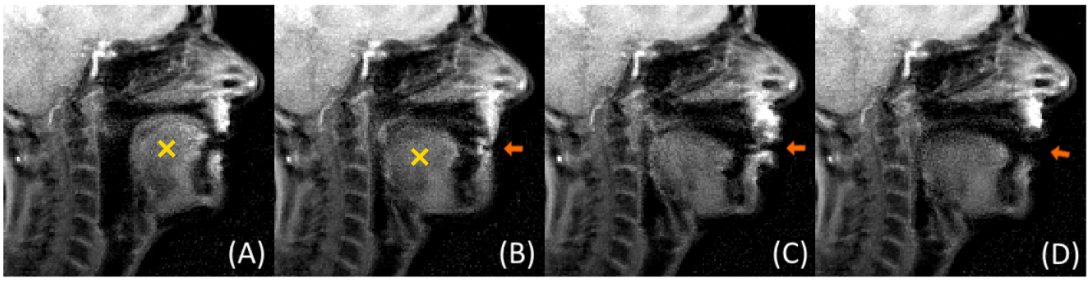

Figure 7.2: Spiral real-time imaging of a speaking healthy participant. Four time frames are shown in (A - D) and differences in the position of tongue and mouth are emphasized in yellow and orange, respectively.

In a second measurement, the volunteer was asked to speak during an acquisition of five adjacent slices. Four real-time frames of one exemplary slice are depicted in Figure 7.2 (A - D). To emphasize different positions of the tongue, the corresponding area is marked in yellow in Figure 7.2 (A) and (B), respectively. Furthermore, apparent differences in the shape of mouth and lips are highlighted in orange in Figure 7.2 (B - D). They could refer to letters such as 'm', 'o' and 'a', respectively.

The results show high-quality images of the upper respiratory tract with the ability to resolve the path of a swallowed fluid as well as the various positions of tongue, mouth and lips during speech. In accordance with the cardiac real-time results at 3 T, no artifacts due to off-resonance or k-space trajectory errors are visible. As the vocal tract involves many air-tissue boundaries, blurring due to off-resonance is generally of particular concern in spiral real-time MRI of swallowing or speech [82, 116, 133]. Here, the short readout duration of 3.1 ms and sufficient B_0-homogeneity were the key factors that prevented off-resonance related blurring at 3 T.

The importance of spiral sampling patterns in real-time MRI of speech was e.g. demonstrated in the study of Freitas et al. [134], which found that spiral GRE imaging is superior to Cartesian bSSFP imaging in terms of contrast-to-noise ratio and image quality for the example of velopharyngeal insufficiency. Similarly, Sutton et al. [133] investigated articulators in the oral cavity by applying a spiral GRE sequence at 3 T with similar temporal but inferior spatial resolution compared to the CRISPI acquisition. However, they included a field map-based correction of magnetic field inhomogeneities. Lingala et al. [135] avoided off-resonance artifacts by applying a short spiral readout of 2.5 ms to spiral GRAPPA speech imaging at 1.5 T. They achieved a high temporal resolution of 18 ms but a comparatively low spatial resolution of $(2.4 \times 2.4)\,\mathrm{mm}^2$. Recently, Lim et al. [116] applied a convolutional neural network to compensate for off-resonance artifacts in spiral real-time MRI of speech without a separate field map acquisition. They conducted a comprehensive study at 1.5 T to investigate not only the influence of the readout duration but also that of spatially varying and spatially uniform blur.

Altogether, this proof of concept study demonstrated that the developed spiral real-time framework could additionally be employed in other fields of dynamic MRI, which further strengthens the benefit of rapid non-Cartesian sampling patterns.

8 Summary

In this work, accelerated non-Cartesian Magnetic Resonance Imaging (MRI) methods were established and applied to cardiovascular imaging (CMR) at different magnetic field strengths (3 T and 7 T). To enable rapid data acquisition, highly efficient spiral k-space trajectories were created. In addition, hybrid sampling patterns such as the twisting radial lines (TWIRL) k-space trajectory were studied. Imperfections of the dynamic gradient system of a MR scanner result in k-space sampling errors. Ultimately, these errors can lead to image artifacts in non-Cartesian acquisitions. Among other reasons such as an increased reconstruction complexity, they cause the lack of spiral sequences in clinical routine compared to standard Cartesian imaging.
Therefore, the Gradient System Transfer Functions (GSTFs) of both scanners were determined and used for k-space trajectory correction in post-correction as well as in terms of a pre-emphasis. The GSTF pre-emphasis was implemented as a fully automatic procedure, which enabled a precise correction of arbitrary gradient waveforms for double-oblique slice orientations. Consequently, artifacts due to trajectory errors could be mitigated, which resulted in high image quality in non-Cartesian MRI. Additionally, the GSTF correction was validated by measuring pre-emphasized spiral gradient outputs, which showed high agreement with the theoretical gradient waveforms. Furthermore, it could be demonstrated that the performance of the GSTF correction is superior to a simple delay compensation approach.

The developed pulse sequences were applied to gated as well as real-time CMR. Special focus lied on the implementation of a spiral imaging protocol to resolve the beating heart of animals and humans in real time and free breathing. In order to achieve real-time CMR with high spatiotemporal resolution, k-space undersampling was performed. For this reason, efficient sampling strategies were developed with the aim to facilitate compressed sensing (CS) during image reconstruction. The applied CS approach successfully removed aliasing artifacts and yielded high-resolution cardiac image series.

Image reconstruction was performed offline in all cases such that the images were not available immediately after acquisition at the scanner. Spiral real-time CMR could be performed in free breathing, which led to an acquisition time of less than 1 minute for a whole short-axis stack. At 3 T, the results were compared to the gold standard of electrocardiogram-gated Cartesian CMR in breath hold, which revealed similar values for important cardiovascular functional and volumetric parameters. This paves the way to an application of the developed framework in clinical routine of CMR. In addition, the spiral real-time protocol was transferred to swallowing and speech imaging at 3 T, and first images were presented. The results were of high quality and confirm the straightforward utilization of the spiral sequence in other fields of MRI. In general, the GSTF correction yielded high-quality images at both field strengths, 3 T and 7 T. Off-resonance related blurring was mitigated by applying non-Cartesian readout gradients of short duration. At 7 T, however, B_1-inhomogeneity led to image artifacts in some cases.

All in all, this work demonstrated great advances in accelerating the MRI process by combining efficient, undersampled non-Cartesian k-space coverage with CS reconstruction. Trajectory correction using the GSTF can be implemented at any scanner model and enables non-Cartesian imaging with high image quality. Especially MRI of dynamic processes greatly benefits from the presented rapid imaging approaches.

9 Zusammenfassung

In der vorliegenden Arbeit wurden Methoden der beschleunigten Magnetresonanztomographie (MRT) etabliert, welche auf nicht-kartesischer Datenaufnahme beruhen. Diese wurden insbesondere in der Herzbildgebung bei verschiedenen Magnetfeldstärken (3 T und 7 T) angewendet. Der Fokus lag auf der Entwicklung von hocheffizienten spiralförmigen k-Raum Trajektorien, mit dem Zweck sehr kurze Aufnahmezeiten zu ermöglichen. Zusätzlich wurde eine hybride k-Raum Trajektorie untersucht, die sogenannte "twisting radial lines (TWIRL)" k-Raum Trajektorie. Ungenauigkeiten des dynamischen Gradientensystems eines MRT Scanners resultieren in fehlerbehafteter k-Raum Abtastung während der Datenaufnahme. In der nicht-kartesischen Bildgebung kann dies letztendlich zu Artefakten im rekonstruierten Bild führen. Zusammen mit anderen Hemmnissen, wie beispielsweise einer komplexeren Bildrekonstruktion, sind sie verantwortlich dafür, dass noch immer mehrheitlich kartesische Bildgebungssequenzen in der klinischen Routine durchgeführt werden.
Aus diesem Grund wurden die Übertragungsfunktionen der Gradientensysteme der verwendeten MRT Scanner (eng. "Gradient System Transfer Function (GSTF)") bestimmt und für k-Raum Trajektorienkorrekturen verwendet. Diese Korrektur wurde sowohl in der Bildrekonstruktion nach bereits erfolgter Datenaufnahme angewendet als auch im Rahmen einer Vorverstärkung bevor die Gradienten ausgespielt werden. Diese Vorverstärkung wurde als vollständig automatisierter Prozess implementiert und ermöglichte eine präzise Korrektur beliebig gewählter Gradientenfunktionen aller Schichtorientierungen. Auf diesem Wege konnten die durch Trajektorienfehler verursachten Bildartefakte kompensiert werden, was zu hoher Bildqualität in der nicht-kartesischen MRT Bildgebung führte. Des Weiteren wurde die Gradientenkorrektur durch Messungen der tatsächlich ausgespielten Gradientenformen validiert. Diese wiesen eine hohe Übereinstimmung mit den theoretisch zu erwarteten Gradientenformen auf. Darüber hinaus wurde gezeigt, dass die auf der Impulsantwort basierende, umfassende Gradientenkorrektur eine höhere Bildqualität ermöglicht als eine einfache Korrektur mittels globaler Zeitverschiebungen.

Die entwickelten MRT Sequenzen wurden sowohl in der segmentierten als auch in der Echtzeit-Herzbildgebung angewendet. Im Speziellen lag der Fokus auf der Implementierung eines Protokolls für die spirale MRT Bildgebung, welche das schlagende Herz von Tieren und Menschen in Echtzeit und freier Atmung auflösen kann. Um Echtzeit-Herzbildgebung mit hoher räumlicher und zeitlicher Auflösung zu vereinen, wurde der k-Raum unterabgetastet. In diesem Zusammenhang wurden Strategien zur effizienten und komprimierten Datenaufnahme entwickelt, unter Anwendung der Modell-basierten "Compressed Sensing" (CS)-Technik. Diese Methode reduziert Aliasing-Artefakte in der Bildrekonstruktion von unterabgetasteten Daten und ermöglicht deshalb hochaufgelöste, dynamische Echtzeit-Bilderserien des schlagenden Herzens. Allerdings wurden die gemessenen Daten stets extern rekonstruiert, sodass die Bilder nicht unmittelbar nach der Aufnahme am MRT Scanner verfügbar waren. Die spirale Echtzeit-Herzbildgebung konnte in freier Atmung durchgeführt werden, was eine Messzeit aller Schichten in der kurzen Herzachse in unter 1 Minute ermöglichte. Bei 3 T wurden die Ergebnisse mit dem Goldstandard der mittels eines Elektrokardiogramms segmentierten kartesischen Herzbildgebung im Atemstopp verglichen und es konnte gezeigt werden, dass wichtige funktionelle und volumetrische Herzparameter übereinstimmen. Dies ebnet den Weg zur Anwendung des entwickelten Protokolls in der klinischen Routine der Herzbildgebung am MRT. Darüber hinaus wurde das Protokoll in der Echtzeit-Bildgebung von Schlucken und Sprechen bei 3 T getestet. Die Ergebnisse waren ebenfalls von hoher Qualität und bestätigen den unkomplizierten Transfer der spiralen Sequenz in andere Bereiche der MRT Bildgebung. Insgesamt lieferte die GSTF-Korrektur Bilder von hoher Qualität bei beiden Feldstärken, 3 T und 7 T. Eine durch off-Resonanz verursachte Bildunschärfe wurde durch kurze Auslesezeiten der nicht-kartesischen Gradienten abgeschwächt. Allerdings führte B_1-Inhomogenität in manchen Fällen zu Bildartefakten bei 7 T.

Die vorliegende Arbeit stellt einen wesentlichen Beitrag zur Beschleunigung des MRT Bildgebungsprozesses dar, indem effiziente, unterabgetastete nicht-kartesische k-Raum Trajektorien mit der CS-Rekonstruktionstechnik kombiniert wurden. Trajektorien-Korrektur basierend auf der GSTF kann prinzipiell an jedem MRT Scanner implementiert werden und legt den Grundstein für nicht-kartesische Bildgebung mit hoher Bildqualität. Insbesondere die Bildgebung von dynamischen Prozessen profitiert von den hier vorgestellten beschleunigten Methoden zur Datenaufnahme.

Bibliography

[1] G. Barisano, F. Sepehrband, S. Ma, K. Jann, R. Cabeen, D. J. Wang, A. W. Toga, and M. Law. "Clinical 7 T MRI: Are we there yet? A review about magnetic resonance imaging at ultra-high field". In: *The British Journal of Radiology* 92.1094 (2019), p. 20180492. DOI: 10.1259/bjr.20180492.

[2] D. W. McRobbie, E. A. Moore, M. J. Graves, and M. R. Prince. *MRI from Picture to Proton*. Second Edition. Cambridge University Press, 2006.

[3] N. Müller. *Die olympische Devise "citius, altius, fortius" und ihr Urheber Henri Didon*. Accessed on May 06, 2021. URL: https://mueller.sport.uni-mainz.de/files/2018/08/DIDON.pdf.

[4] A. D. Faigenbaum, R. S. Lloyd, J. MacDonald, and G. D. Myer. "Citius, Altius, Fortius: beneficial effects of resistance training for young athletes: narrative review". In: *British Journal of Sports Medicine* 50.1 (2016), pp. 3–7. DOI: 10.1136/bjsports-2015-094621.

[5] J. M. Theysohn, S. Maderwald, O. Kraff, C. Moenninghoff, M. E. Ladd, and S. C. Ladd. "Subjective acceptance of 7 Tesla MRI for human imaging". In: *Magnetic Resonance Materials in Physics, Biology and Medicine* 21.1-2 (2007), pp. 63–72. DOI: 10.1007/s10334-007-0095-x.

[6] T. Niendorf, D. K. Sodickson, G. A. Krombach, and J. Schulz-Menger. "Toward cardiovascular MRI at 7 T: clinical needs, technical solutions and research promises". In: *European Radiology* 20.12 (2010), pp. 2806–2816. DOI: 10.1007/s00330-010-1902-8.

[7] W. T. Clarke, O. Mougin, I. D. Driver, C. Rua, A. T. Morgan, M. Asghar, S. Clare, S. Francis, R. G. Wise, C. T. Rodgers, A. Carpenter, K. Muir, and R. Bowtell. "Multi-site harmonization of 7 tesla MRI neuroimaging protocols". In: *NeuroImage* 206 (2020), p. 116335. DOI: 10.1016/j.neuroimage.2019.116335.

[8] X. He, M. A. Ertürk, A. Grant, X. Wu, R. L. Lagore, L. DelaBarre, Y. Eryaman, G. Adriany, E. J. Auerbach, P.-F. Moortele, K. Uğurbil, and G. J. Metzger. "First in-vivo human imaging at 10.5T: Imaging the body at 447 MHz". In: *Magnetic Resonance in Medicine* 84.1 (2020), pp. 289–303. DOI: 10.1002/mrm.28131.

[9] A. Sadeghi-Tarakameh, L. DelaBarre, R. L. Lagore, A. Torrado-Carvajal, X. Wu, A. Grant, G. Adriany, G. J. Metzger, P.-F. V. de Moortele, K. Ugurbil, E. Atalar, and Y. Eryaman. "In vivo human head MRI at 10.5T: A radiofrequency safety study and preliminary imaging results". In: *Magnetic Resonance in Medicine* 84.1 (2020), pp. 484–496. DOI: 10.1002/mrm.28093.

[10] W. Oldendorf and W. Oldendorf. "Advantages and Disadvantages of MRI". In: *Basics of Magnetic Resonance Imaging. Topics in Neurology*. Vol. 1. Springer, Bosten, MA, 1988, pp. 125–138. DOI: 10.1007/978-1-4613-2081-4_9.

[11] A. Haase, J. Frahm, D. Matthaei, W. Hanicke, and K.-D. Merboldt. "FLASH imaging. Rapid NMR imaging using low flip-angle pulses". In: *Journal of Magnetic Resonance (1969)* 67.2 (1986), pp. 258–266. DOI: 10.1016/0022-2364(86)90433-6.

[12] P. B. Roemer, W. A. Edelstein, C. E. Hayes, S. P. Souza, and O. M. Mueller. "The NMR phased array". In: *Magnetic Resonance in Medicine* 16.2 (1990), pp. 192–225. DOI: 10.1002/mrm.1910160203.

[13] K. P. Pruessmann, M. Weiger, M. B. Scheidegger, and P. Boesiger. "SENSE: sensitivity encoding for fast MRI". In: *Magnetic Resonance in Medicine* 42.5 (1999), pp. 952–962. DOI: 10.1002/(SICI)1522-2594(199911)42%3A5<952%3A%3AAID-MRM16>3.0.CO%3B2-S.

[14] M. A. Griswold, P. M. Jakob, R. M. Heidemann, M. Nittka, V. Jellus, J. Wang, B. Kiefer, and A. Haase. "Generalized autocalibrating partially parallel acquisitions (GRAPPA)". In: *Magnetic Resonance in Medicine* 47.6 (2002), pp. 1202–1210. DOI: 10.1002/mrm.10171.

[15] M. Lustig, D. Donoho, and J. M. Pauly. "Sparse MRI: The application of compressed sensing for rapid MR imaging". In: *Magnetic Resonance in Medicine* 58.6 (2007), pp. 1182–1195. DOI: 10.1002/mrm.21391.

[16] M. B. Stokes and R. Roberts-Thomson. "The role of cardiac imaging in clinical practice". In: *Australian Prescriber* 40.4 (2017), pp. 151–155. DOI: 10.18773/austprescr.2017.045.

[17] F. Grothues, G. C. Smith, J. C. Moon, N. G. Bellenger, P. Collins, H. U. Klein, and D. J. Pennell. "Comparison of interstudy reproducibility of cardiovascular magnetic resonance with two-dimensional echocardiography in normal subjects and in patients with heart failure or left ventricular hypertrophy". In: *The American Journal of Cardiology* 90.1 (2002), pp. 29–34. DOI: 10.1016/S0002-9149(02)02381-0.

[18] S. Marchesseau, J. X. Ho, and J. J. Totman. "Influence of the short-axis cine acquisition protocol on the cardiac function evaluation: a reproducibility study". In: *European Journal of Radiology Open* 3 (2016), pp. 60–66. DOI: 10.1016/j.ejro.2016.03.003.

[19] D. G. Nishimura. *Principles of magnetic resonance imaging*. Edition 1.2. Standford University, 2016.

[20] L. Wang, N. Salibi, Y. Wu, M. E. Schweitzer, and R. R. Regatte. "Relaxation times of skeletal muscle metabolites at 7T". In: *Journal of Magnetic Resonance Imaging* 29.6 (2009), pp. 1457–1464. DOI: 10.1002/jmri.21787.

[21] M. A. Bernstein, K. F. King, and X. J. Zhou. *Handbook of MRI pulse sequences*. First Edition. Elsevier Academic Press, 2004.

[22] M. Schär, S. Kozerke, S. E. Fischer, and P. Boesiger. "Cardiac SSFP imaging at 3 Tesla". In: *Magnetic Resonance in Medicine* 51.4 (2004), pp. 799–806. DOI: 10.1002/mrm.20024.

[23] T. A. Gallagher, A. J. Nemeth, and L. Hacein-Bey. "An introduction to the Fourier transform: relationship to MRI". In: *American Journal of Roentgenology* 190.5 (2008), pp. 1396–1405. DOI: 10.2214/AJR.07.2874.

[24] J. A. Fessler and B. P. Sutton. "Nonuniform fast Fourier transforms using min-max interpolation". In: *IEEE Transactions on Signal Processing* 51.2 (2003), pp. 560–574. DOI: 10.1109/TSP.2002.807005.

[25] A. Deshmane, V. Gulani, M. A. Griswold, and N. Seiberlich. "Parallel MR imaging". In: *Journal of Magnetic Resonance Imaging* 36.1 (2012), pp. 55–72. DOI: 10.1002/jmri.23639.

[26] M. Blaimer, F. Breuer, M. Mueller, R. M. Heidemann, M. A. Griswold, and P. M. Jakob. "SMASH, SENSE, PILS, GRAPPA: how to choose the optimal method". In: *Topics in Magnetic Resonance Imaging* 15.4 (2004), pp. 223–236. DOI: 10.1097/01.rmr.0000136558.09801.dd.

[27] D. J. Larkman and R. G. Nunes. “Parallel magnetic resonance imaging”. In: *Physics in Medicine & Biology* 52.7 (2007), R15–R55. DOI: 10.1088/0031-9155/52/7/R01.

[28] J. I. Jackson, D. G. Nishimura, and A. Macovski. “Twisting radial lines with application to robust magnetic resonance imaging of irregular flow”. In: *Magnetic Resonance in Medicine* 25.1 (1992), pp. 128–139. DOI: 10.1002/mrm.1910250113.

[29] B. M. Delattre, R. M. Heidemann, L. A. Crowe, J.-P. Vallée, and J.-N. Hyacinthe. “Spiral demystified”. In: *Magnetic Resonance Imaging* 28.6 (2010), pp. 862–881. DOI: 10.1016/j.mri.2010.03.036.

[30] Y. Qian and F. E. Boada. “Acquisition-weighted stack of spirals for fast high-resolution three-dimensional ultra-short echo time MR imaging”. In: *Magnetic Resonance in Medicine* 60.1 (2008), pp. 135–145. DOI: 10.1002/mrm.21620.

[31] C. Liu, R. Bammer, D.-h. Kim, and M. E. Moseley. “Self-navigated interleaved spiral (SNAILS): application to high-resolution diffusion tensor imaging”. In: *Magnetic Resonance in Medicine* 52.6 (2004), pp. 1388–1396. DOI: 10.1002/mrm.20288.

[32] R. Zhou, Y. Yang, R. C. Mathew, J. P. Mugler III, D. S. Weller, C. M. Kramer, A. H. Ahmed, M. Jacob, and M. Salerno. “Free-breathing cine imaging with motion-corrected reconstruction at 3T using SPiral Acquisition with Respiratory correction and Cardiac Self-gating (SPARCS)”. In: *Magnetic Resonance in Medicine* 82.2 (2019), pp. 706–720. DOI: 10.1002/mrm.27763.

[33] K. T. Block and J. Frahm. “Spiral imaging: a critical appraisal”. In: *Journal of Magnetic Resonance Imaging* 21.6 (2005), pp. 657–668. DOI: 10.1002/jmri.20320.

[34] D. G. Nishimura, P. Irarrazabal, and C. H. Meyer. “A velocity k-space analysis of flow effects in echo-planar and spiral imaging”. In: *Magnetic Resonance in Medicine* 33.4 (1995), pp. 549–556. DOI: 10.1002/mrm.1910330414.

[35] G. H. Glover and A. T. Lee. “Motion artifacts in fMRI: comparison of 2DFT with PR and spiral scan methods”. In: *Magnetic Resonance in Medicine* 33.5 (1995), pp. 624–635. DOI: 10.1002/mrm.1910330507.

[36] M. Engel, L. Kasper, C. Barmet, T. Schmid, L. Vionnet, B. Wilm, and K. P. Pruessmann. “Single-shot spiral imaging at 7 T”. In: *Magnetic Resonance in Medicine* 80.5 (2018), pp. 1836–1846. DOI: 10.1002/mrm.27176.

[37] Y. Yang, L. Zhao, X. Chen, P. W. Shaw, J. A. Gonzalez, F. H. Epstein, C. H. Meyer, C. M. Kramer, and M. Salerno. “Reduced field of view single-shot spiral perfusion imaging”. In: *Magnetic Resonance in Medicine* 79.1 (2018), pp. 208–216. DOI: 10.1002/mrm.26664.

[38] T. B. Harshbarger and D. B. Twieg. “Iterative reconstruction of single-shot spiral MRI with off resonance”. In: *IEEE Transactions on Medical Imaging* 18.3 (1999), pp. 196–205. DOI: 10.1109/42.764889.

[39] C. H. Meyer, B. S. Hu, D. G. Nishimura, and A. Macovski. “Fast spiral coronary artery imaging”. In: *Magnetic Resonance in Medicine* 28.2 (1992), pp. 202–213. DOI: 10.1002/mrm.1910280204.

[40] J. G. Pipe and N. R. Zwart. “Spiral trajectory design: a flexible numerical algorithm and base analytical equations”. In: *Magnetic Resonance in Medicine* 71.1 (2014), pp. 278–285. DOI: 10.1002/mrm.24675.

[41] J.-R. Liao, J. M. Pauly, T. J. Brosnan, and N. J. Pelc. “Reduction of motion artifacts in cine MRI using variable-density spiral trajectories”. In: *Magnetic Resonance in Medicine* 37.4 (1997), pp. 569–575. DOI: 10.1002/mrm.1910370416.

[42] J. H. Lee, B. A. Hargreaves, B. S. Hu, and D. G. Nishimura. “Fast 3D imaging using variable-density spiral trajectories with applications to limb perfusion”. In: *Magnetic Resonance in Medicine* 50.6 (2003), pp. 1276–1285. DOI: 10.1002/mrm.10644.

[43] D.-h. Kim, E. Adalsteinsson, and D. M. Spielman. “Simple analytic variable density spiral design”. In: *Magnetic Resonance in Medicine* 50.1 (2003), pp. 214–219. DOI: 10.1002/mrm.10493.

[44] J. G. Pipe. “An optimized center-out k-space trajectory for multishot MRI: comparison with spiral and projection reconstruction”. In: *Magnetic Resonance in Medicine* 42.4 (1999), pp. 714–720. DOI: 10.1002/(SICI)1522-2594(199910)42:4<714::AID-MRM13>3.0.CO;2-G.

[45] G. H. Glover. “Spiral imaging in fMRI”. In: *Neuroimage* 62.2 (2012), pp. 706–712. DOI: 10.1016/j.neuroimage.2011.10.039.

[46] B. M. Dale, J. S. Lewin, and J. L. Duerk. “Optimal design of k-space trajectories using a multi-objective genetic algorithm”. In: *Magnetic Resonance in Medicine* 52.4 (2004), pp. 831–841. DOI: 10.1002/mrm.20233.

[47] E. Yudilevich and H. Stark. “Spiral sampling in magnetic resonance imaging-the effect of inhomogeneities”. In: *IEEE Transactions on Medical Imaging* 6.4 (1987), pp. 337–345. DOI: 10.1109/TMI.1987.4307852.

[48] P. Börnert, H. Schomberg, B. Aldefeld, and J. Groen. “Improvements in spiral MR imaging”. In: *Magnetic Resonance Materials in Physics, Biology and Medicine* 9.1-2 (1999), pp. 29–41. DOI: 10.1007/BF02634590.

[49] K. P. Pruessmann, M. Weiger, P. Börnert, and P. Boesiger. “Advances in sensitivity encoding with arbitrary k-space trajectories”. In: *Magnetic Resonance in Medicine* 46.4 (2001), pp. 638–651. DOI: 10.1002/mrm.1241.

[50] N. Seiberlich, F. A. Breuer, M. Blaimer, K. Barkauskas, P. M. Jakob, and M. A. Griswold. “Non-Cartesian data reconstruction using GRAPPA operator gridding (GROG)”. In: *Magnetic Resonance in Medicine* 58.6 (2007), pp. 1257–1265. DOI: 10.1002/mrm.21435.

[51] N. Seiberlich, F. Breuer, M. Blaimer, P. Jakob, and M. Griswold. “Self-calibrating GRAPPA operator gridding for radial and spiral trajectories”. In: *Magnetic Resonance in Medicine* 59.4 (2008), pp. 930–935. DOI: 10.1002/mrm.21565.

[52] J. Pauly. *Reconstruction of Non-Cartesian Data*. Accessed on June 17, 2020. URL: https://users.fmrib.ox.ac.uk/~karla/reading_group/lecture_notes/AdvRecon_Pauly_read.pdf.

[53] J. A. Fessler. “On NUFFT-based gridding for non-Cartesian MRI”. In: *Journal of Magnetic Resonance* 188.2 (2007), pp. 191–195. DOI: 10.1016/j.jmr.2007.06.012.

[54] J. I. Jackson, C. H. Meyer, D. G. Nishimura, and A. Macovski. “Selection of a convolution function for Fourier inversion using gridding (computerised tomography application)”. In: *IEEE Transactions on Medical Imaging* 10.3 (1991), pp. 473–478. DOI: 10.1109/42.97598.

[55] V. Rasche, R. Proksa, R. Sinkus, P. Bornert, and H. Eggers. “Resampling of data between arbitrary grids using convolution interpolation”. In: *IEEE Transactions on Medical Imaging* 18.5 (1999), pp. 385–392. DOI: 10.1109/42.774166.

[56] J. G. Pipe and P. Menon. “Sampling density compensation in MRI: rationale and an iterative numerical solution”. In: *Magnetic Resonance in Medicine* 41.1 (1999), pp. 179–186. DOI: 10.1002/(SICI)1522-2594(199901)41:1<179::AID-MRM25>3.0.CO;2-V.

[57] D. L. Donoho. “For most large underdetermined systems of linear equations the minimal $\ell 1$-norm solution is also the sparsest solution”. In: *Communications on Pure and Applied Mathematics* 59.6 (2006), pp. 797–829. DOI: 10.1002/cpa.20132.

[58] D. L. Donoho. “Compressed sensing”. In: *IEEE Transactions on Information Theory* 52.4 (2006), pp. 1289–1306. DOI: 10.1109/TIT.2006.871582.

[59] S. Geethanath, R. Reddy, A. S. Konar, S. Imam, R. Sundaresan, R. B. DR, and R. Venkatesan. “Compressed sensing MRI: a review”. In: *Critical Reviews™ in Biomedical Engineering* 41.3 (2013), pp. 183–204. DOI: 10.1615/CritRevBiomedEng.2014008058.

[60] R. Otazo, E. Candes, and D. K. Sodickson. “Low-rank plus sparse matrix decomposition for accelerated dynamic MRI with separation of background and dynamic components”. In: *Magnetic Resonance in Medicine* 73.3 (2015), pp. 1125–1136. DOI: 10.1002/mrm.25240.

[61] A. S. Stern, D. L. Donoho, and J. C. Hoch. “NMR data processing using iterative thresholding and minimum l1-norm reconstruction”. In: *Journal of Magnetic Resonance* 188.2 (2007), pp. 295–300. DOI: 10.1016/j.jmr.2007.07.008.

[62] M. Stich, T. Wech, A. Slawig, R. Ringler, A. Dewdney, A. Greiser, G. Ruyters, T. A. Bley, and H. Köstler. “Gradient waveform pre-emphasis based on the gradient system transfer function”. In: *Magnetic Resonance in Medicine* 80.4 (2018), pp. 1521–1532. DOI: 10.1002/mrm.27147.

[63] J. H. Duyn, Y. Yang, J. A. Frank, and J. W. van der Veen. “Simple correction method for k-space trajectory deviations in MRI”. In: *Journal of Magnetic Resonance* 132.1 (1998), pp. 150–153. DOI: 10.1006/jmre.1998.1396.

[64] H. Tan and C. H. Meyer. “Estimation of k-space trajectories in spiral MRI”. In: *Magnetic Resonance in Medicine* 61.6 (2009), pp. 1396–1404. DOI: 10.1002/mrm.21813.

[65] P. Jehenson, M. Westphal, and N. Schuff. “Analytical method for the compensation of eddy-current effects induced by pulsed magnetic field gradients in NMR systems”. In: *Journal of Magnetic Resonance (1969)* 90.2 (1990), pp. 264–278. DOI: 10.1016/0022-2364(90)90133-T.

[66] O. Bieri, M. Markl, and K. Scheffler. “Analysis and compensation of eddy currents in balanced SSFP”. In: *Magnetic Resonance in Medicine* 54.1 (2005), pp. 129–137. DOI: 10.1002/mrm.20527.

[67] R. K. Robison, Z. Li, D. Wang, M. B. Ooi, and J. G. Pipe. “Correction of B0 eddy current effects in spiral MRI”. In: *Magnetic Resonance in Medicine* 81.4 (2019), pp. 2501–2513. DOI: 10.1002/mrm.27583.

[68] Y. Wu, B. A. Chronik, C. Bowen, C. K. Mechefske, and B. K. Rutt. "Gradient-induced acoustic and magnetic field fluctuations in a 4T whole-body MR imager". In: *Magnetic Resonance in Medicine* 44.4 (2000), pp. 532–536. DOI: 10.1002/1522-2594(200010)44:4<532::AID-MRM6>3.0.CO;2-Q.

[69] S. J. Vannesjo, M. Haeberlin, L. Kasper, M. Pavan, B. J. Wilm, C. Barmet, and K. P. Pruessmann. "Gradient system characterization by impulse response measurements with a dynamic field camera". In: *Magnetic Resonance in Medicine* 69.2 (2013), pp. 583–593. DOI: 10.1002/mrm.24263.

[70] A. E. Campbell-Washburn, H. Xue, R. J. Lederman, A. Z. Faranesh, and M. S. Hansen. "Real-time distortion correction of spiral and echo planar images using the gradient system impulse response function". In: *Magnetic Resonance in Medicine* 75.6 (2015), pp. 2278–2285. DOI: 10.1002/mrm.25788.

[71] S. J. Vannesjo, N. N. Graedel, L. Kasper, S. Gross, J. Busch, M. Haeberlin, C. Barmet, and K. P. Pruessmann. "Image reconstruction using a gradient impulse response model for trajectory prediction". In: *Magnetic Resonance in Medicine* 76.1 (2016), pp. 45–58. DOI: 10.1002/mrm.25841.

[72] N. O. Addy, H. H. Wu, and D. G. Nishimura. "Simple method for MR gradient system characterization and k-space trajectory estimation". In: *Magnetic Resonance in Medicine* 68.1 (2012), pp. 120–129. DOI: 10.1002/mrm.23217.

[73] H. Liu and G. B. Matson. "Accurate measurement of magnetic resonance imaging gradient characteristics". In: *Materials* 7.1 (2014), pp. 1–15. DOI: 10.3390/ma7010001.

[74] J. Rahmer, P. Mazurkewitz, P. Börnert, and T. Nielsen. "Rapid acquisition of the 3D MRI gradient impulse response function using a simple phantom measurement". In: *Magnetic Resonance in Medicine* 82.6 (2019), pp. 2146–2159. DOI: 10.1002/mrm.27902.

[75] M. Stich, C. Pfaff, T. Wech, A. Slawig, G. Ruyters, A. Dewdney, R. Ringler, and H. Köstler. "The temperature dependence of gradient system response characteristics". In: *Magnetic Resonance in Medicine* 83.4 (2020), pp. 1519–1527. DOI: 10.1002/mrm.28013.

[76] S. Mendis, P. Puska, and B. Norrving. *Global atlas on cardiovascular disease prevention and control*. World Health Organization, 2011. URL: https://apps.who.int/iris/handle/10665/44701.

[77] R. M. Lang, L. P. Badano, V. Mor-Avi, J. Afilalo, A. Armstrong, L. Ernande, F. A. Flachskampf, E. Foster, S. A. Goldstein, T. Kuznetsova, P. Lancellotti, D. Muraru, M. H. Picard, E. R. Rietzschel, L. Rudski, K. T. Spencer, W. Tsang, and J.-U. Voigt. "Recommendations for cardiac chamber quantification by echocardiography in adults: an update from the American Society of Echocardiography and the European Association of Cardiovascular Imaging". In: *European Heart Journal-Cardiovascular Imaging* 16.3 (2015), pp. 233–271. DOI: 10.1093/ehjci/jev014.

[78] K. Alfakih, S. Reid, T. Jones, and M. Sivananthan. "Assessment of ventricular function and mass by cardiac magnetic resonance imaging". In: *European Radiology* 14.10 (2004), pp. 1813–1822. DOI: 10.1007/s00330-004-2387-0.

[79] A. K. Attili, A. Schuster, E. Nagel, J. H. Reiber, and R. J. van der Geest. "Quantification in cardiac MRI: advances in image acquisition and processing". In: *The International Journal of Cardiovascular Imaging* 26.1 (2010), pp. 27–40. DOI: 10.1007/s10554-009-9571-x.

[80] K. Seetharam and S. Lerakis. "Cardiac magnetic resonance imaging: the future is bright". In: *F1000Research* 8.1636 (2019). DOI: 10.12688/f1000research.19721.1.

[81] G. Giovannetti, D. De Marchi, and A. Pingitore. "Radiofrequency coils and pulse sequences for cardiac magnetic resonance applications: New perspectives and future developments". In: *Reviews in Cardiovascular Medicine* 17.3-4 (2016), pp. 124–130. DOI: 10.3909/ricm0846.

[82] K. S. Nayak, Y. Lim, A. E. Campbell-Washburn, and J. Steeden. "Real-Time Magnetic Resonance Imaging". In: *Journal of Magnetic Resonance Imaging* (2020). DOI: 10.1002/jmri.27411.

[83] R. M. Setser, S. E. Fischer, and C. H. Lorenz. "Quantification of left ventricular function with magnetic resonance images acquired in real time". In: *Journal of Magnetic Resonance Imaging* 12.3 (2000), pp. 430–438. DOI: 10.1002/1522-2586(200009)12:3<430::AID-JMRI8>3.0.CO;2-V.

[84] A. C. Larson, R. D. White, G. Laub, E. R. McVeigh, D. Li, and O. P. Simonetti. "Self-gated cardiac cine MRI". In: *Magnetic Resonance in Medicine* 51.1 (2004), pp. 93–102. DOI: 10.1002/mrm.10664.

[85] L. Di Sopra, D. Piccini, S. Coppo, M. Stuber, and J. Yerly. “An automated approach to fully self-gated free-running cardiac and respiratory motion-resolved 5D whole-heart MRI”. In: *Magnetic Resonance in Medicine* 82.6 (2019), pp. 2118–2132. DOI: 10.1002/mrm.27898.

[86] M. Beer, H. Stamm, W. Machann, A. Weng, J. P. Goltz, F. Breunig, F. Weidemann, D. Hahn, and H. Köstler. “Free breathing cardiac real-time cine MR without ECG triggering”. In: *International Journal of Cardiology* 145.2 (2010), pp. 380–382. DOI: https://doi.org/10.1016/j.ijcard.2010.02.052.

[87] K. S. Nayak and B. S. Hu. “Triggered real-time MRI and cardiac applications”. In: *Magnetic Resonance in Medicine* 49.1 (2003), pp. 188–192. DOI: 10.1002/mrm.10341.

[88] K. S. Nayak, C. H. Cunningham, J. M. Santos, and J. M. Pauly. “Real-time cardiac MRI at 3 Tesla”. In: *Magnetic Resonance in Medicine* 51.4 (2004), pp. 655–660. DOI: 10.1002/mrm.20053.

[89] K. S. Nayak, B. A. Hargreaves, B. S. Hu, D. G. Nishimura, J. M. Pauly, and C. H. Meyer. “Spiral balanced steady-state free precession cardiac imaging”. In: *Magnetic Resonance in Medicine* 53.6 (2005), pp. 1468–1473. DOI: 10.1002/mrm.20489.

[90] O. Sayin, H. Saybasili, M. M. Zviman, M. Griswold, H. Halperin, N. Seiberlich, and D. A. Herzka. “Real-time free-breathing cardiac imaging with self-calibrated through-time radial GRAPPA”. In: *Magnetic Resonance in Medicine* 77.1 (2017), pp. 250–264. DOI: 10.1002/mrm.26112.

[91] Y. Y. Li, S. Rashid, Y. J. Cheng, W. Schapiro, K. Gliganic, A.-M. Yamashita, J. Tang, M. Grgas, M. Mendez, E. Haag, J. Pang, B. Stoeckel, C. Leidecker, and J. J. Cao. “Real-time cardiac MRI with radial acquisition and k-space variant reduced-FOV reconstruction”. In: *Magnetic Resonance Imaging* 53 (2018), pp. 98–104. DOI: 10.1016/j.mri.2018.07.008.

[92] X. Feng, M. Salerno, C. M. Kramer, and C. H. Meyer. “Non-Cartesian balanced steady-state free precession pulse sequences for real-time cardiac MRI”. In: *Magnetic Resonance in Medicine* 75.4 (2016), pp. 1546–1555. DOI: 10.1002/mrm.25738.

[93] X. Zhong, B. S. Spottiswoode, C. H. Meyer, C. M. Kramer, and F. H. Epstein. “Imaging three-dimensional myocardial mechanics using navigator-gated volumetric spiral cine DENSE MRI”. In: *Magnetic Resonance in Medicine* 64.4 (2010), pp. 1089–1097. DOI: 10.1002/mrm.22503.

[94] R. Bastkowski, K. Weiss, D. Maintz, and D. Giese. “Self-gated golden-angle spiral 4D flow MRI”. In: *Magnetic Resonance in Medicine* 80.3 (2018), pp. 904–913. DOI: 10.1002/mrm.27085.

[95] A. Tolouee, J. Alirezaie, and P. Babyn. “Compressed sensing reconstruction of cardiac cine MRI using golden angle spiral trajectories”. In: *Journal of Magnetic Resonance* 260 (2015), pp. 10–19. DOI: 10.1016/j.jmr.2015.09.003.

[96] B. Sievers, M. Addo, S. Kirchberg, A. Bakan, B. John-Puthenveettil, U. Franken, and H.-J. Trappe. “Impact of the ECG gating method on ventricular volumes and ejection fractions assessed by cardiovascular magnetic resonance imaging”. In: *Journal of Cardiovascular Magnetic Resonance* 7.2 (2005), pp. 441–446. DOI: 10.1081/JCMR-53515.

[97] F. Schmitt, D. Grosu, C. Mohr, D. Purdy, K. Salem, K. Scott, and B. Staeckel. “3 Tesla-MRT: Der Erfolg höherer Feldstärken”. In: *Radiologe* 44.1 (2004), pp. 31–48. DOI: 10.1007/s00117-003-1000-x.

[98] B. Hargreaves. *Variable-Density Spiral Design Functions*. Accessed 2018-2020. URL: https://mrsrl.stanford.edu/~brian/vdspiral/.

[99] I. A. Elabyad, M. Terekhov, D. Lohr, M. R. Stefanescu, S. Baltes, and L. M. Schreiber. “A novel mono-surface antisymmetric 8Tx/16Rx coil array for parallel transmit cardiac MRI in pigs at 7T”. In: *Scientific Reports* 10.1 (2020), pp. 1–18. DOI: 10.1038/s41598-020-59949-6.

[100] I. A. Elabyad, M. Terekhov, M. R. Stefanescu, D. Lohr, M. Fischer, and L. M. Schreiber. “Design and evaluation of a novel symmetric multichannel transmit/receive coil array for cardiac MRI in pigs at 7 T”. In: *IEEE Transactions on Microwave Theory and Techniques* 67.9 (2019), pp. 3928–3945. DOI: 10.1109/TMTT.2019.2913636.

[101] I. A. Elabyad, M. Terekhov, M. Stefanescu, D. Lohr, M. Fischer, and L. Schreiber. “Design of a novel antisymmetric coil array for parallel transmit cardiac MRI in pigs at 7 T”. In: *Journal of Magnetic Resonance* 305 (2019), pp. 195–208. DOI: 10.1016/j.jmr.2019.07.004.

[102] P. Eirich, T. Wech, J. F. Heidenreich, M. Stich, N. Petri, P. Nordbeck, T. A. Bley, and H. Köstler. “Cardiac real-time MRI using a pre-emphasized spiral acquisition based on the gradient system transfer function”. In: *Magnetic Resonance in Medicine* 85.5 (2021), pp. 2747–2760. DOI: 10.1002/mrm.28621.

[103] A. Maceira, S. Prasad, M. Khan, and D. Pennell. "Normalized left ventricular systolic and diastolic function by steady state free precession cardiovascular magnetic resonance". In: *Journal of Cardiovascular Magnetic Resonance* 8.3 (2006), pp. 417–426. DOI: 10.1080/10976640600572889.

[104] J. Hutter, A. N. Price, L. Cordero-Grande, S. Malik, G. Ferrazzi, A. Gaspar, E. J. Hughes, D. Christiaens, L. McCabe, T. Schneider, M. A. Rutherford, and J. V. Hajnal. "Quiet echo planar imaging for functional and diffusion MRI". In: *Magnetic Resonance in Medicine* 79.3 (2018), pp. 1447–1459. DOI: 10.1002/mrm.26810.

[105] J. A. Steeden, G. T. Kowalik, O. Tann, M. Hughes, K. H. Mortensen, and V. Muthurangu. "Real-time assessment of right and left ventricular volumes and function in children using high spatiotemporal resolution spiral bSSFP with compressed sensing". In: *Journal of Cardiovascular Magnetic Resonance* 20.79 (2018), pp. 1–11. DOI: 10.1186/s12968-018-0500-9.

[106] T. Wech, N. Seiberlich, A. Schindele, V. Grau, L. Diffley, M. L. Gyngell, A. Borzì, H. Köstler, and J. E. Schneider. "Development of real-time magnetic resonance imaging of mouse hearts at 9.4 Tesla—simulations and first application". In: *IEEE Transactions on Medical Imaging* 35.3 (2015), pp. 912–920. DOI: 10.1109/TMI.2015.2501832.

[107] D. Stäb, T. Wech, F. A. Breuer, A. M. Weng, C. O. Ritter, D. Hahn, and H. Köstler. "High resolution myocardial first-pass perfusion imaging with extended anatomic coverage". In: *Journal of Magnetic Resonance Imaging* 39.6 (2014), pp. 1575–1587. DOI: 10.1002/jmri.24303.

[108] K. Hammernik, T. Klatzer, E. Kobler, M. P. Recht, D. K. Sodickson, T. Pock, and F. Knoll. "Learning a variational network for reconstruction of accelerated MRI data". In: *Magnetic Resonance in Medicine* 79.6 (2018), pp. 3055–3071. DOI: 10.1002/mrm.26977.

[109] L. Kasper, M. Engel, C. Barmet, M. Haeberlin, B. J. Wilm, B. E. Dietrich, T. Schmid, S. Gross, D. O. Brunner, K. E. Stephan, and K. P. Pruessmann. "Rapid anatomical brain imaging using spiral acquisition and an expanded signal model". In: *NeuroImage* 168 (2018), pp. 88–100. DOI: 10.1016/j.neuroimage.2017.07.062.

[110] Y. Qian, T. Zhao, Y.-K. Hue, T. S. Ibrahim, and F. E. Boada. "High-resolution spiral imaging on a whole-body 7T scanner with minimized image blurring".

In: *Magnetic Resonance in Medicine* 63.3 (2010), pp. 543–552. DOI: 10.1002/mrm.22215.

[111] M. Esmaeili, B. Strasser, W. Bogner, P. Moser, Z. Wang, and O. C. Andronesi. "Whole-slab 3D MR spectroscopic imaging of the human brain with spiral-out-in sampling at 7T". In: *Journal of Magnetic Resonance Imaging* 53.4 (2020), pp. 1237–1250. DOI: 10.1002/jmri.27437.

[112] G. Buonincontri, R. F. Schulte, M. Cosottini, and M. Tosetti. "Spiral MR fingerprinting at 7T with simultaneous B1 estimation". In: *Magnetic Resonance Imaging* 41 (2017), pp. 1–6. DOI: https://doi.org/10.1016/j.mri.2017.04.003.

[113] O. Kraff, A. Fischer, A. M. Nagel, C. Mönninghoff, and M. E. Ladd. "MRI at 7 Tesla and above: demonstrated and potential capabilities". In: *Journal of Magnetic Resonance Imaging* 41.1 (2015), pp. 13–33. DOI: 10.1002/jmri.24573.

[114] E. Ahunbay and J. G. Pipe. "Rapid method for deblurring spiral MR images". In: *Magnetic Resonance in Medicine* 44.3 (2000), pp. 491–494. DOI: 10.1002/1522-2594(200009)44:3<491::AID-MRM22>3.0.CO;2-Z.

[115] M. Hock, M. Terekhov, M. R. Stefanescu, D. Lohr, S. Herz, T. Reiter, M. Ankenbrand, A. Kosmala, T. Gassenmaier, C. Juchem, and L. M. Schreiber. "B0 shimming of the human heart at 7T". In: *Magnetic Resonance in Medicine* 85.1 (2021), pp. 182–196. DOI: 10.1002/mrm.28423.

[116] Y. Lim, Y. Bliesener, S. Narayanan, and K. S. Nayak. "Deblurring for spiral real-time MRI using convolutional neural networks". In: *Magnetic Resonance in Medicine* 84.6 (2020), pp. 3438–3452. DOI: 10.1002/mrm.28393.

[117] L.-C. Man, J. M. Pauly, and A. Macovski. "Multifrequency interpolation for fast off-resonance correction". In: *Magnetic Resonance in Medicine* 37.5 (1997), pp. 785–792. DOI: 10.1002/mrm.1910370523.

[118] L.-C. Man, J. M. Pauly, and A. Macovski. "Improved automatic off-resonance correction without a field map in spiral imaging". In: *Magnetic Resonance in Medicine* 37.6 (1997), pp. 906–913. DOI: 10.1002/mrm.1910370616.

[119] K. S. Nayak, C.-M. Tsai, C. H. Meyer, and D. G. Nishimura. "Efficient off-resonance correction for spiral imaging". In: *Magnetic Resonance in Medicine* 45.3 (2001), pp. 521–524. DOI: 10.1002/1522-2594(200103)45:3<521::AID-MRM1069>3.0.CO;2-6.

[120] H. Moriguchi, B. M. Dale, J. S. Lewin, and J. L. Duerk. "Block regional off-resonance correction (BRORC): a fast and effective deblurring method for spiral imaging". In: *Magnetic Resonance in Medicine* 50.3 (2003), pp. 643–648. DOI: 10.1002/mrm.10570.

[121] W. Chen and C. H. Meyer. "Fast automatic linear off-resonance correction method for spiral imaging". In: *Magnetic Resonance in Medicine* 56.2 (2006), pp. 457–462. DOI: 10.1002/mrm.20973.

[122] W. Chen and C. H. Meyer. "Semiautomatic off-resonance correction in spiral imaging". In: *Magnetic Resonance in Medicine* 59.5 (2008), pp. 1212–1219. DOI: 10.1002/mrm.21599.

[123] D. Stäb, A. Al Najjar, K. O'Brien, W. Strugnell, J. Richer, J. Rieger, T. Niendorf, and M. Barth. "Cardiac magnetic resonance imaging at 7 Tesla". In: *JoVE (Journal of Visualized Experiments)* 143 (2019), e55853. DOI: 10.3791/55853.

[124] J. J. Suttie, L. DelaBarre, A. Pitcher, P. F. van de Moortele, S. Dass, C. J. Snyder, J. M. Francis, G. J. Metzger, P. Weale, K. Ugurbil, S. Neubauer, M. Robson, and T. Vaughan. "7 Tesla (T) human cardiovascular magnetic resonance imaging using FLASH and SSFP to assess cardiac function: validation against 1.5 T and 3 T." In: *NMR in Biomedicine* 25.1 (2012), pp. 27–34. DOI: 10.1002/nbm.1708.

[125] S. Rapacchi, T. Troalen, Z. Bentatou, M. Quemeneur, M. Guye, M. Bernard, A. Jacquier, and F. Kober. "Simultaneous multi-slice cardiac cine with Fourier-encoded self-calibration at 7 Tesla". In: *Magnetic Resonance in Medicine* 81.4 (2019), pp. 2576–2587. DOI: 10.1002/mrm.27593.

[126] F. von Knobelsdorff-Brenkenhoff, V. Tkachenko, L. Winter, J. Rieger, C. Thalhammer, F. Hezel, A. Graessl, M. A. Dieringer, T. Niendorf, and J. Schulz-Menger. "Assessment of the right ventricle with cardiovascular magnetic resonance at 7 Tesla". In: *Journal of Cardiovascular Magnetic Resonance* 15.1 (2013), pp. 1–9. DOI: 10.1186/1532-429X-15-23.

[127] C. S. Aigner, S. Dietrich, and S. Schmitter. "Three-dimensional static and dynamic parallel transmission of the human heart at 7 T". In: *NMR in Biomedicine* 34.3 (2021), e4450. DOI: 10.1002/nbm.4450.

[128] E.-S. H. Ibrahim, V. E. Arpinar, L. T. Muftuler, J. Stojanovska, A. S. Nencka, and K. M. Koch. "Cardiac functional magnetic resonance imaging at 7T: Image quality optimization and ultra-high field capabilities". In: *World Journal of Radiology* 12.10 (2020), pp. 231–246. DOI: 10.4329/wjr.v12.i10.231.

[129] C. R. Castets, E. J. Ribot, W. Lefrançois, A. J. Trotier, E. Thiaudière, J.-M. Franconi, and S. Miraux. “Fast and robust 3D T1 mapping using spiral encoding and steady RF excitation at 7 T: application to cardiac manganese enhanced MRI (MEMRI) in mice”. In: *NMR in Biomedicine* 28.7 (2015), pp. 881–889. DOI: 10.1002/nbm.3327.

[130] B. Dietz, B. G. Fallone, and K. Wachowicz. “Nomenclature for real-time magnetic resonance imaging”. In: *Magnetic Resonance in Medicine* 81.3 (2019), pp. 1483–1484. DOI: 10.1002/mrm.27487.

[131] M. Bock, L. Traser, A. Caglar Özen, M. Burdumy, B. Richter, and M. Echternach. “Reply to Letter to the Editor: “Nomenclature for real-time magnetic resonance imaging””. In: *Magnetic Resonance in Medicine* 81.3 (2019), pp. 1485–1485. DOI: 10.1002/mrm.27599.

[132] K. S. Nayak. “Response to Letter to the Editor: “Nomenclature for real-time magnetic resonance imaging””. In: *Magnetic Resonance in Medicine* 82.2 (2019), pp. 525–526. DOI: 10.1002/mrm.27770.

[133] B. P. Sutton, C. A. Conway, Y. Bae, R. Seethamraju, and D. P. Kuehn. “Faster dynamic imaging of speech with field inhomogeneity corrected spiral fast low angle shot (FLASH) at 3 T”. In: *Journal of Magnetic Resonance Imaging* 32.5 (2010), pp. 1228–1237. DOI: 10.1002/jmri.22369.

[134] A. C. Freitas, M. Wylezinska, M. J. Birch, S. E. Petersen, and M. E. Miquel. “Comparison of Cartesian and non-Cartesian real-time MRI sequences at 1.5 T to assess velar motion and velopharyngeal closure during speech”. In: *Plos One* 11.4 (2016), e0153322. DOI: 10.1371/journal.pone.0153322.

[135] S. G. Lingala, Y. Zhu, Y. Lim, A. Toutios, Y. Ji, W.-C. Lo, N. Seiberlich, S. Narayanan, and K. S. Nayak. “Feasibility of through-time spiral generalized autocalibrating partial parallel acquisition for low latency accelerated real-time MRI of speech”. In: *Magnetic Resonance in Medicine* 78.6 (2017), pp. 2275–2282. DOI: 10.1002/mrm.26611.

Publications

Journal article

Philipp Eirich, Tobias Wech, Julius F. Heidenreich, Manuel Stich, Nils Petri, Peter Nordbeck, Thorsten A. Bley, Herbert Köstler. "Cardiac real-time MRI using a pre-emphasized spiral acquisition based on the gradient system transfer function". In: *Magnetic Resonance in Medicine* 85.5 (2021), pp. 2747-2760. DOI: `https://doi.org/10.1002/mrm.28621`

Conference abstracts

Philipp Eirich, Tobias Wech, Manuel Stich, Julian A.J. Richter, Thorsten A. Bley, Herbert Köstler. "Spiral imaging using a fully automatic pre-emphasis based on the Gradient System Transfer Function (GSTF)". *ISMRM* 27^{th} *Annual Meeting & Exhibition*; Montréal, QC, Canada; 2019

Philipp Eirich, Tobias Wech, Manuel Stich, Theresa Reiter, Laura M. Schreiber, Herbert Köstler. "Pre-emphasis of Twisting Radial Lines (TWIRL) using the Gradient System Transfer Function (GSTF) at 7T". *ESMRMB* 36^{th} *Annual Scientific Meeting*; Rotterdam, Netherlands; 2019

Philipp Eirich, Tobias Wech, Julius F. Heidenreich, Manuel Stich, Nils Petri, Peter Nordbeck, Thorsten A. Bley, Herbert Köstler. "Spiral real-time cardiac MR imaging using a GSTF-based pre-emphasis". *ISMRM Virtual Conference & Exhibition*; 2020

Philipp Eirich, Tobias Wech, Julius F. Heidenreich, Manuel Stich, Nils Petri, Peter Nordbeck, Thorsten A. Bley, Herbert Köstler. "Cardiac real-time MRI at 3T with a GSTF-corrected spiral k-space trajectory". *Online EUREKA! Symposium of the Graduate School of Life Sciences*; 2020

Johannes Portmann, Tobias Wech, **Philipp Eirich**, Herbert Köstler. "MOCO-MAP using a TWIRL trajectory". *ESMRMB* 36^{th} *Annual Scientific Meeting*; Rotterdam, Netherlands; 2019

Johannes Portmann, Tobias Wech, **Philipp Eirich**, Herbert Köstler. “MOCO-MAP - fast and multiparametric cardiac MRI”. *Online EUREKA! Symposium of the Graduate School of Life Sciences*; 2020

Jonas Kleineisel, **Philipp Eirich**, Julius F. Heidenreich, Herbert Köstler, Thorsten A. Bley, Tobias Wech. “Real-time cardiac MRI using spiral read-outs and a Variational Network for data-driven reconstruction”. *ISMRM Virtual Conference & Exhibition*; 2021

Curriculum Vitae

Danksagung

An dieser Stelle bedanke ich mich bei all den Personen, die zu dem Gelingen dieser Promotionsarbeit beigetragen haben.

Zunächst gilt mein besonderer Dank Prof. Dr. Herbert Köstler, der mir diese spannende und interessante Themenstellung anbot und die Arbeit mit großem Engagement und Zeitaufwand betreute. Als Leiter der experimentellen Radiologie sind Sie hauptverantwortlich für die großartige Zusammenarbeit und Atmosphäre innerhalb unserer Arbeitsgruppe, ich habe mich dort immer bestens aufgehoben gefühlt.
Darüber hinaus gilt mein herzlicher Dank Prof. Dr. Tobias Wech, der als direkter Ansprechpartner ebenfalls meine Arbeit beaufsichtigte und betreute. Die Zusammenarbeit mit dir hat mir immer außerordentlich Spaß gemacht und auch dir war kein Anruf und keine Frage zu viel. Die Betreuungssituation insgesamt war herausragend und trug damit maßgeblich zu dem erfolgreichen Verlauf des Promotionsprojektes bei.
Ebenso gilt mein Dank Prof. Dr. Thorsten Bley, der als Leiter des Instituts für Diagnostische und Interventionelle Radiologie des Universitätsklinikums Würzburg das Promotionsprojekt ermöglichte und mir ein tolles Arbeitsumfeld bot. Im Besonderen der Austausch zwischen Naturwissenschaftlern und Ärzten hat mich persönlich immer sehr interessiert. Deshalb möchte ich mich auch bei Dr. Julius Heidenreich für die gute Zusammenarbeit und sein Forschungsinteresse bedanken.
Insgesamt möchte ich mich ausdrücklich bei allen weiteren Kolleginnen und Kollegen aus der Experimentellen Radiologie bedanken: Katharina Rath, Dr. Andreas Weng, Dr. Anne Slawig, Dr. Lenon Mendes Pereira, Dr. Manuel Stich, Dr. Julian Richter, Juliana Bibiano, Johannes Portmann, Hannah Scholten und Jonas Kleineisel. Ich hatte wirklich eine klasse Zeit und die Stimmung war immer überragend. Vor allem die gegenseitige Hilfe und Unterstützung wusste ich immer sehr zu schätzen und ist nicht selbstverständlich.

Des Weiteren gilt mein Dank Prof. Dr. Laura Schreiber und ihrer Arbeitsgruppe im Deutschen Zentrum für Herzinsuffizienz. Mir wurden nicht nur erstklassige Räumlichkeiten zur Verfügung gestellt, sondern ich wurde auch von allen Beteiligten sehr herzlich aufgenommen und in die Messroutine am 7 T Tomographen miteinbezogen.

Ein großes Dankeschön gilt ebenso der Graduate School of Life Sciences, welche ein herausragendes, strukturiertes Promotionsprogramm anbietet. Es wird dort sehr viel geleistet, um den Promotionsstudenten ein breites Spektrum an Weiterbildungsmöglichkeiten bereit zu stellen. In diesem Zusammenhang möchte ich mich gerne bei meinem gesamten Prüfungskomitee bedanken, bestehend aus Prof. Dr. Herbert Köstler, Prof. Dr. Laura Schreiber und PD Dr. Bernhard Petritsch. In regelmäßigen Treffen wurden dort meine Ergebnisse diskutiert und ich erhielt fachliche Ratschläge und Anregungen. Zuletzt gilt mein persönlicher Dank meiner Freundin Cristina Klinnert, sowie meiner Familie Antonia, Maria und Roland Eirich, die mich zu jedem Zeitpunkt innerhalb der Promotion uneingeschränkt unterstützt haben.

Affidavit

I hereby confirm that my thesis entitled "Accelerated non-Cartesian cardiovascular MR Imaging at 3 T and 7 T" is the result of my own work. I did not receive any help or support from commercial consultants. All sources and / or materials applied are listed and specified in the thesis.

Furthermore, I confirm that this thesis has not yet been submitted as part of another examination process neither in identical nor in similar form.

Würzburg; May 21, 2021

Philipp Eirich

Eidesstattliche Erklärung

Hiermit erkläre ich an Eides statt, die Dissertation "Beschleunigte nicht-kartesische MRT Herzbildgebung bei 3 T und 7 T" eigenständig, d.h. insbesondere selbständig und ohne Hilfe eines kommerziellen Promotionsberaters, angefertigt und keine anderen als die von mir angegebenen Quellen und Hilfsmittel verwendet zu haben.

Ich erkläre außerdem, dass die Dissertation weder in gleicher noch in ähnlicher Form bereits in einem anderen Prüfungsverfahren vorgelegen hat.

Würzburg; 21. Mai 2021

Philipp Eirich